Next Materials 8 (2025) 100772

Contents lists available at ScienceDirect

Next Materials

journal homepage: www.sciencedirect.com/journal/next-materials

Review article

Recent advances in electrochemical CO_2 reaction to C_{3+} products

Yiding Yang, Kaili Liu, Md Sakib Hasan Khan, Zhehao Sun, Zongyou Yin *

Research School of Chemistry, Australian National University, Canberra, ACT 2601, Australia

ARTICLE INFO

Keywords:
Electrocatalysis
CO_2 reduction reaction
Cu-based materials
Non-Cu-based materials
C_{3+} products

ABSTRACT

One effective strategy for mitigating carbon emissions is utilizing carbon dioxide as a substrate to synthesize high-value multi-carbon products through the electrochemical CO_2 reduction reaction (CO_2RR). Despite the widespread application of C_{3+} oxygenated hydrocarbons, including propanol, acetone, and butanol, in numerous industrial chemical processes, the literature provides scant reporting on their role in electrochemical CO_2 reduction reactions. In this review, the reaction mechanisms specific to predominant C_3 products are analyzed in detail. Subsequently, we outline advancements concerning three distinct variants of Cu-based catalysts, namely 1) Cu oxide-derived catalysts, 2) Cu nanoparticle catalysts, and 3) Cu single atoms and molecular Cu catalysts. Meanwhile, the feasibility of designing copper-based tandem catalytic systems to produce C_{3+} products in CO_2RR is also discussed. Additionally, the review explores the emergence of non-Cu-based catalysts, particularly nickel (Ni)- and molybdenum (Mo)-based transition-metal phosphides and chalcogenides. These systems, with the characterization of high catalytic efficiency, excellent stability and low cost, provide sustainable and economical alternatives. The integration of such catalysis offers promising solutions to overcome existing limitations, paving the way for efficient, scalable, and sustainable CO_2RR technologies. Besides artificial intelligence (AI) and machine learning (ML) combined with DFT and high-throughput (HT) experiments, as a new paradigm shift in data-driven catalyst exploration, this review addressed some promising recent work for catalysts to yield C_{3+} products from CO_2RR on that edge.

1. Introduction

Global industrialization has accelerated for over a century, accompanied by the large-scale use of fossil fuels (coal, oil, and natural gas), resulting in a significant increase in greenhouse gas emissions (such as CO_2 and NO_2) [1,2], which has had irreversible effects on global surface temperatures and precipitation. What's worse, traditional fossil fuels will continue to dominate energy consumption in the long term, and the current global CO_2 emissions remain a cause for concern [3]. As shown in (Fig. 1), global CO_2 emissions have been rising annually, reaching 36.1 billion tons in 2022. If the current emission growth rate continues, the temperature will increase by 1.5℃ within 7.1 years. [4] To mitigate the greenhouse effect, researchers have developed various technologies to capture and convert carbon dioxide into value-added chemicals [5], including electrochemical reduction [6], photocatalytic reduction [7], and biological conversion [8].

Among these methods, the CO_2RR is considered the most promising conversion pathway due to its unique advantages: (1) CO_2RR can be carried out under mild conditions; (2) the reaction phase can be finely controlled, and adjustable electrochemical parameters facilitate high conversion efficiency; (3) it can utilize various renewable energy sources such as wind and solar power as electrocatalytic drivers, storing energy in the synthesized chemicals [9].

High C═O bonding energy (750 kJ mol^{-1}) makes CO_2 very stable, resulting in a high activation energy requirement for CO_2RR [10]. To date, efforts to break through the performance boundaries to meet commercialization needs have been made by using metal catalysts, including copper (Cu), gold (Au), and silver (Ag) [11]. In recent years, significant progress has been made in the selectivity and Faradaic efficiency (FE) of C_1 and C_2 products in CO_2RR, such as carbon monoxide (CO) [12], formic acid [13,14], and ethylene [15,16].

However, although significant progress has been achieved in electrochemical CO_2RR for producing C_1 and C_2 products, the electrochemical CO_2RR still faces a lot of challenges in achieving high selectivity and productivity when generating C_3 and C_{3+} products. The main bottlenecks hindering industrial-scale production and commercialization include: Firstly, the selectivity and productivity toward C_{3+} products are generally low, currently insufficient to meet the economic

* Corresponding author.
E-mail address: zongyou.yin@anu.edu.au (Z. Yin).

https://doi.org/10.1016/j.nxmate.2025.100772
Received 19 January 2025; Received in revised form 27 March 2025; Accepted 27 May 2025
Available online 31 May 2025

viability and scalability required for industrial applications [17]. Secondly, reports and systematic investigations on C_{3+} products are considerably fewer compared to those on C_1 and C_2 products, leading to an incomplete understanding of the reaction mechanisms, critical intermediates, and product distribution rules [18]. This significantly hinders precise tuning and further optimization of reaction systems. Thirdly, the synthesis of C_{3+} products involves complex carbon-carbon coupling steps, such as C_1-C_1 and C_1-C_2 coupling, which impose stringent requirements on the surface structures and electronic properties of the catalysts [19]. Moreover, the formation pathways of C_{3+} products often compete directly with those of C_2 products (e.g., ethylene and ethanol) [20]. Additionally, undesirable side-products such as hydrogen and formic acid are commonly formed, significantly diminishing selectivity and overall efficiency towards target C_{3+} chemicals. Lastly, few studies have reported stable, long-term production of C_{3+} products under high current densities, indicating an urgent need to enhance both the overall energy efficiency and reaction stability for industrial-scale applications [21].

Despite these challenges, C_{3+} products have attracted considerable attention due to their essential roles in industry, energy, and consumer products, holding key positions in modern manufacturing and everyday life [22]. For example, propane and butane are extensively used as heating fuels in both industrial and residential applications. Ethane and propane are frequently converted via dehydrogenation into essential petrochemical platform molecules such as ethylene and propylene. Additionally, isoprene and butadiene serve as critical monomers in elastomeric materials, including synthetic rubbers widely used in tyres. Styrene is predominantly utilized in the production of polystyrene and as a comonomer in high-performance polymer materials such as acrylonitrile-butadiene-styrene (ABS), styrene-butadiene rubber, and unsaturated polyester resins [23]. Moreover, certain oxygen-containing C_{3+} compounds, including n-propanol, isopropanol, n-butanol, isobutanol, and 1,4-butanediol (1,4-BDO), are also widely applied in industrial production and daily consumer products. N-propanol and propionaldehyde are essential solvents and reaction intermediates in various chemical processes. Specifically, n-propanol has drawn significant attention as a promising fuel additive due to its superior octane rating, higher heat value, and lower emission characteristics compared to methanol and ethanol. Isopropanol, n-butanol, and isobutanol are extensively used as industrial cleaners and key solvents in household products such as inks and paints due to their high volatility, ease of removal, and amphiphilic nature (compatibility with both aqueous and organic phases) [22].

Despite the established high economic value and market demand of these C_{3+} products in the industrial and energy sectors, their global production and market scale remain significantly limited due to technical and cost barriers. For instance, the current global production of n-propanol is merely around 0.2 million tons per year—considerably lower than mature bulk chemicals like methanol (150 million tons/year), ethanol (77 million tons/year), and ethylene (140 million tons/year). This limited supply maintains a high market price, constraining broader applications and large-scale industrial development. Notably, propylene, propane, and butane possess substantial global market values of approximately 104.1 billion USD, 82.4 billion USD, and 108.4 billion USD, respectively. Other economically significant C_{3+} products include propanol (3.1 billion USD), acetone (5.7 billion USD), ethyl acetate (5.5 billion USD), butadiene (10.5 billion USD), 1,4-butanediol (6.5 billion USD), and 1-butanol (5.2 billion USD) [21,22]. These substantial market values underscore the immense economic potential and importance of sustainably synthesizing these C_{3+} products [21].

Thus, advancing high-efficiency CO_2 electrochemical conversion technologies to overcome current bottlenecks in selectivity and productivity of C_{3+} products can significantly reduce their production costs, expand market sizes, and enhance economic competitiveness. Such advancements are expected not only to unlock greater application potentials in high-value sectors, including fuels, plastics, synthetic rubbers, and polyurethanes, but also fundamentally drive the low-carbon transition and sustainable growth of the global chemical industry, resulting in considerable environmental benefits and economic returns.

Copper is widely used in CO_2RR, due to its unique empty d-orbitals, can coordinate with CO_2 and reduce the energy of the C═O bond during catalysis [24,25]. Moreover, it also has ideal binding energies with most intermediates produced in CO_2RR (e.g., *OCHO, *CO) [26], allowing these intermediates to further couple and generate multi-carbon products. This review first describes the current generation mechanisms of the most common C_3 products through electrochemical CO_2RR. Then comprehensively analyzes various copper-based catalysts, dividing the Cu catalysts based on their structural and morphological characteristics into oxide-derived Cu (OD-Cu), Cu nanoparticles (NPs), Cu single atoms (SAs), and molecular Cu catalysts. The review summarizes the research

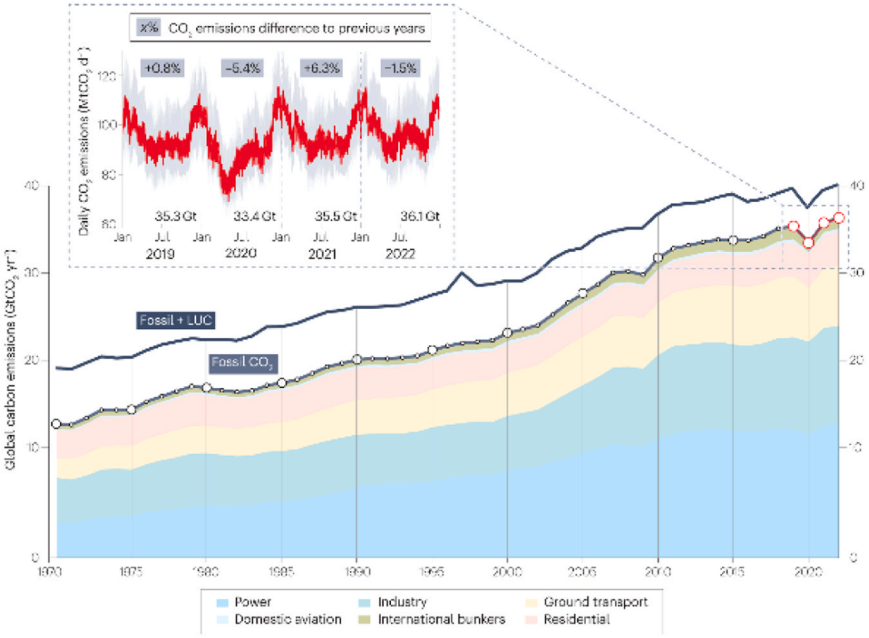

Fig. 1. Global CO_2 emissions 1970–2022 [4]. Copyright 2023, Springer Nature.

progress of existing copper-based catalysts and non-copper-based catalysts in converting CO_2 into C_{3+} products through electrochemical reduction. Additionally, it discusses some insights into the production of C_{3+} products through the design of tandem catalytic systems in CO_2RR, pointing to the future design of highly active, directionally selective, and stable catalysts and tandem catalytic systems.

While significant advancements have been made in the electrochemical CO_2RR to produce C_1 and C_2 products, the synthesis of C_{3+} products remains an intricate challenge due to the high energy barriers, complex reaction pathways, and critical need for well-optimized active sites to facilitate C-C coupling. Conventional methods, such as density functional theory (DFT) and experimental high-throughput screening, often fall short in addressing these complexities due to their computational and resource limitations. Recent breakthroughs in integrating artificial intelligence (AI), machine learning (ML), and high-throughput algorithms have introduced a transformative paradigm for catalyst discovery. These data-driven approaches accelerate the identification and optimization of electrocatalysts by combining the predictive power of ML with the fundamental insights provided by DFT, enabling the rapid screening of vast catalytic spaces and improving reaction selectivity. By leveraging these innovations, researchers have made strides in designing highly selective catalysts, particularly to produce complex hydrocarbons and oxygenates, offering a promising pathway to overcome the inherent challenges of CO_2RR. This review also analyses the promising insights from this perspective.

2. Reaction pathways and mechanism of C_3 products

The reaction mechanisms for CO_2 conversion into C_2 products (such as C_2H_4, C_2H_5OH, etc.) are highly diverse, with their primary differences arising from the various C-C coupling pathways. Influenced by catalysts and reaction environments, it is widely recognized that four main *C-C coupling mechanisms exist, including *CO-CO [27,28], *OC-CHOH [29], *OC-CHO [30], *OC-COH [31], and H_2C-CH_2 [32] (* representing adsorption sites on the catalyst surface). Current research has conducted relatively thorough investigations on these four different *C-C coupling methods and subsequent reactions. Theoretically, the generation of C_3 products from CO_2 involves 3206 intermediates and 4506 reactions [33], resulting in significant controversies over the reaction mechanisms of various C_3 products. It is generally believed that there are two main pathways for the CO_2RR to C_3 products: one is the direct trimerization of *CO (C_1-C_1-C_1) [34], and the other is the formation of *C_2 intermediates through *C-C coupling, followed by the coupling of *C_2 intermediates with *CO (*C_1-C_2) [35], ultimately forming C_3 products. According to current reports and related density functional theory (DFT) studies, the main C_3 products generated through CO_2RR are 1-propanol, 2-propanol, acetone, propylene, and propane. Therefore, we will mainly discuss the reaction mechanisms of these five products.

2.1. Mechanism of n-propanol

n-propanol is the most common C_3 product in CO_2RR using Cu-based catalysts. Although the exact reaction pathway for n-propanol remains unclear, current studies suggest that its formation occurs through the cleavage of the O-C bond at the middle carbon position of the C-C-C chain. This results in an oxygen-containing carbon at the end of the alkyl chain [36–38]. Additionally, there is evidence indicating that ample C-C coupling to form C_2 intermediates and/or ethylene [39], as well as saturated CO or *CO, can increase the selectivity for n-propanol [40–42]. According to DFT calculations, three types of *C_2 intermediates can produce n-propanol: *OCCO [41,43], *OCCOH [44,45], and *HOCCOH [46]. These intermediates are determined by the active sites provided by the catalyst during the reaction, with specific steps illustrated in Fig. 2.

The most common pathway for the formation of n-propanol is shown in the black route. It begins with the coupling of two *CO to form *OCCO. The resulting *OCCO then reacts with a third *CO to form *OCCOCO, which subsequently undergoes a proton-electron transfer process to form n-propanol. The blue route represents the *HOCCOH reaction pathway, two *HOC molecules couple to form *HOC-COH, which then undergoes *CO insertion and n-propanol forms through proton-electron transfer. The red route involves the *COCHO and *CO coupling to form *COCOCHO. However, it is important to note that the *C_2 intermediates in these three pathways are also considered key intermediates for ethylene and ethanol which means C_2 products will inevitably compete with n-propanol during CO_2RR process

2.2. Mechanism of 2-propanol reaction & acetone

Unlike the formation mechanism of n-propanol, 2-propanol primarily forms through the coupling of the *OCH_2CH_3 intermediate with *CO to form *$CHOHCHOHCH_3$, which then undergoes a proton-electron

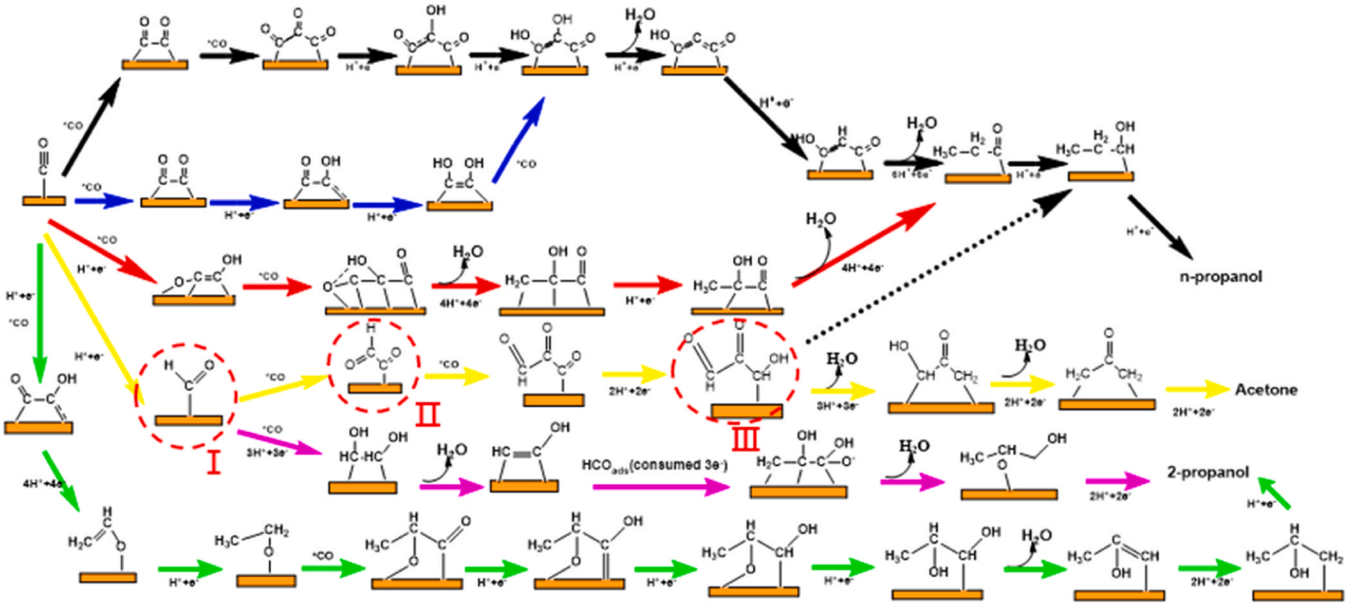

Fig. 2. Reaction pathways of n-propanol, 2-propanol, and acetone.

transfer process (green route) [47]. There are some pieces of evidence indicating that over-saturated CO_2 favors the formation of the key intermediate *OCH_2CH_3, increasing the coverage of *CO and *OCH_2CH_3, thereby selectively producing 2-propanol in CO_2RR reactions [47]. However, some studies speculate that 2-propanol forms through the coupling of *HCCOH and *HCO adsorption under alkaline conditions, as shown in the purple route [48], while this formation mechanism of 2-propanol should be verified through a combination of in-situ technical experiments and DFT calculations.

The commonly accepted mechanism for acetone formation involves the 'CO insertion process' which is shown in the yellow route [49]. Gaseous CO_2 forms a radical anion * CO_2•, producing the adsorbed intermediate *COOH. The adsorbed *COOH undergoes further reduction to form the intermediate * CO, leading to the formation of * CHO (I). The desorbed CO can diffuse and spill over to the catalyst sites to undergo the "CO insertion process," forming *COCHO (II). (II) then couples with *CO to form the *CHOHCOCHO (III) intermediate, which eventually undergoes a series of proton-coupled electron transfer processes to form acetone. It is noteworthy that acetone production via this pathway is always accompanied by methanol and 1-propanol formation. After (I), the reduction and rearrangement of the catalyst to *OCH_3 results in the formation of CH_3OH. After (II), it accompanies the formation of ethylene and ethanol, and after (III), it can randomly lead to n-propanol pathways [50].

Chen et al [51]. discovered a new pathway for acetone formation through studies on copper single atoms (Fig. 3**a**). Unlike the previous pathway, in this mechanism, *COCOH transforms into *COC species by breaking the C-O(H) bond. The formed *COC is further reduced to the *$COCH_3$ intermediate through sequential hydrogenation steps. The *$COCH_3$ intermediate then couples with another adsorbed *CO to form *$COCOCH_3$, and finally, through a proton-electron transfer process, acetone is formed.

2.3. Mechanism of propylene and propane

Due to the almost non-existent occurrence of propylene in Cu-based CO_2RR, there is limited research on the mechanism of propylene formation. One possible reason is that the formation of propylene requires 18 electrons, involving complex intermediates and facing kinetic limitations. Additionally, the formation of propylene can be traced back to the allyl alkoxy (*CH_2=$CHCH_2O$) intermediate, which easily desorbs in an alkaline microenvironment, making propylene formation unfavorable [37]. Gao et al [39]. proposed that the key to propylene formation involves the coupling between adsorbed/molecular CO_2 or *COOH intermediates and highly protonated adsorbed *C_2 intermediates with carbon double bonds, such as *OCH=CH_2 from the ethylene pathway. This is followed by multiple proton-electron transfer processes to form propylene (Fig. 3**b**). Yeo et al [52]. proposed a CH/CH_2 insertion mechanism on a polarized Ni surface, starting with the coupling of *CH/CH_2 + *COOH and then followed by the insertion of CH and/or CH_2, forming longer-chain C_{3+} hydrocarbon (Fig. 3**c, d**).

Asadi et al [53]. developed an ImF-Mo_3P catalyst that reduces CO_2 to propane through the trimerization of *CO (Fig. 3**e**). In the most thermodynamically favorable mechanism, the initial steps (prior to RC7) involve three consecutive CO_2 adsorptions and related proton-coupled electron transfer (PCET) reactions (CO_2 → COOH → CO), forming *CO + *CO + *CO adsorbates on three neighboring Mo sites of ImF-Mo_3P (RC7). Through energetic adjustments of the *CO trimers, *CO-CH-CO (RC11), the most promising precursor to proceed into the trimerization step, is finally obtained. After generating the crucial C-C-C trimerization on the surface of catalysts, the final step involves protonating all O/OH groups in the adsorbates (starting from RC11), forming H_2O, and saturating the C atoms with hydrogen to form RC15, yielding the C_3H_8 product.

Huang et al [54]. systematically used machine learning ML to predict the C-C-C coupling process in CO_2RR and the C_3 reaction pathways. They found that the direct coupling of *C_1 intermediates is energetically more favorable than C-C coupling between *C_1 and *C_2 intermediates. The highly hydrogenated synthesis mechanisms of propylene and propane might be more suitable for developing non-Cu-based materials for *C_1-*C_1-*C_1 trimerization. Combining ML with various metal catalysts may thermodynamically discover more favorable pathways for producing propylene and propane.

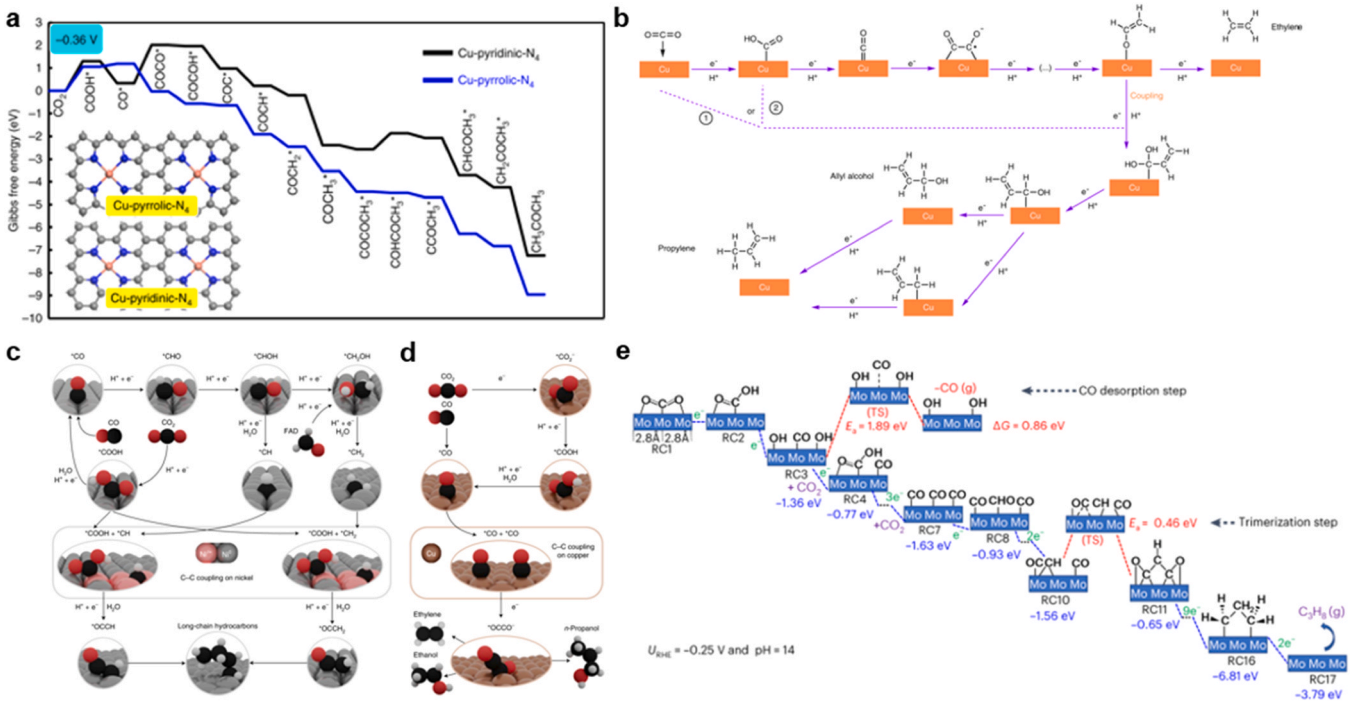

Fig. 3. Reaction pathway for **a** acetone [51], Copyright 2020, Springer Nature. **b** propylene[39] Copyright 2023, Springer Nature **c, d** propylene [52], Copyright 2022, Springer Nature. and **e** propane[53] Copyright 2023, Springer Nature.

3. Cu-based materials for CO_2RR to C_3 products

3.1. Cu oxide-derived Cu catalysts

The heterointerface effect can regulate the reconstruction behavior of catalysts during the electrochemical CO_2RR, which could optimize their activity and stability [55]. Among these strategies, pre-oxidation serves as an effective approach by customizing the surface/interface [56] and modulating the structure and properties [57], thereby regulating the electrified interface through the adjustment of uncoordinated atoms to enhance catalyst selectivity [58].

Oxide-derived copper (Cu-OD) films exhibit unique selectivity towards C_3 products, a property stemming from their potential to generate numerous grain boundaries[46] during consecutive oxidation and redeposition processes. Studies have shown that partially or completely pre-oxidizing Cu catalysts before CO_2 electrolysis can generate catalyst precursors, which subsequently undergo pre-reduction reactions to form Cu-OD materials. This effectively alters the surface morphology, roughness, and size of the catalyst, thereby changing its crystalline orientation which facilitates the formation of active sites on the catalyst surface and low-coordination environments, further promoting the C-C coupling process and enhancing the selectivity and FE towards C_{3+} products. Currently, Cu-OD techniques primarily include chemical oxidation [46,59,60], thermal annealing [61,62], oxygen plasma exposure [63], and halide anion treatment [64–66]. The construction of Cu-OD catalysts typically begins with synthesizing precursor materials where copper exists in an oxidation state of + 1 or + 2. The final activation of these copper oxide-based precursor materials usually occurs before or during the CO_2RR, applying cyclic voltammetry (CV) or linear sweep voltammetry (LSV) tests, within an electrochemical environment.

3.1.1. Chemical oxidation

Cu_xO made from chemically oxidized Cu material has attracted widespread attention due to its simple preparation and other

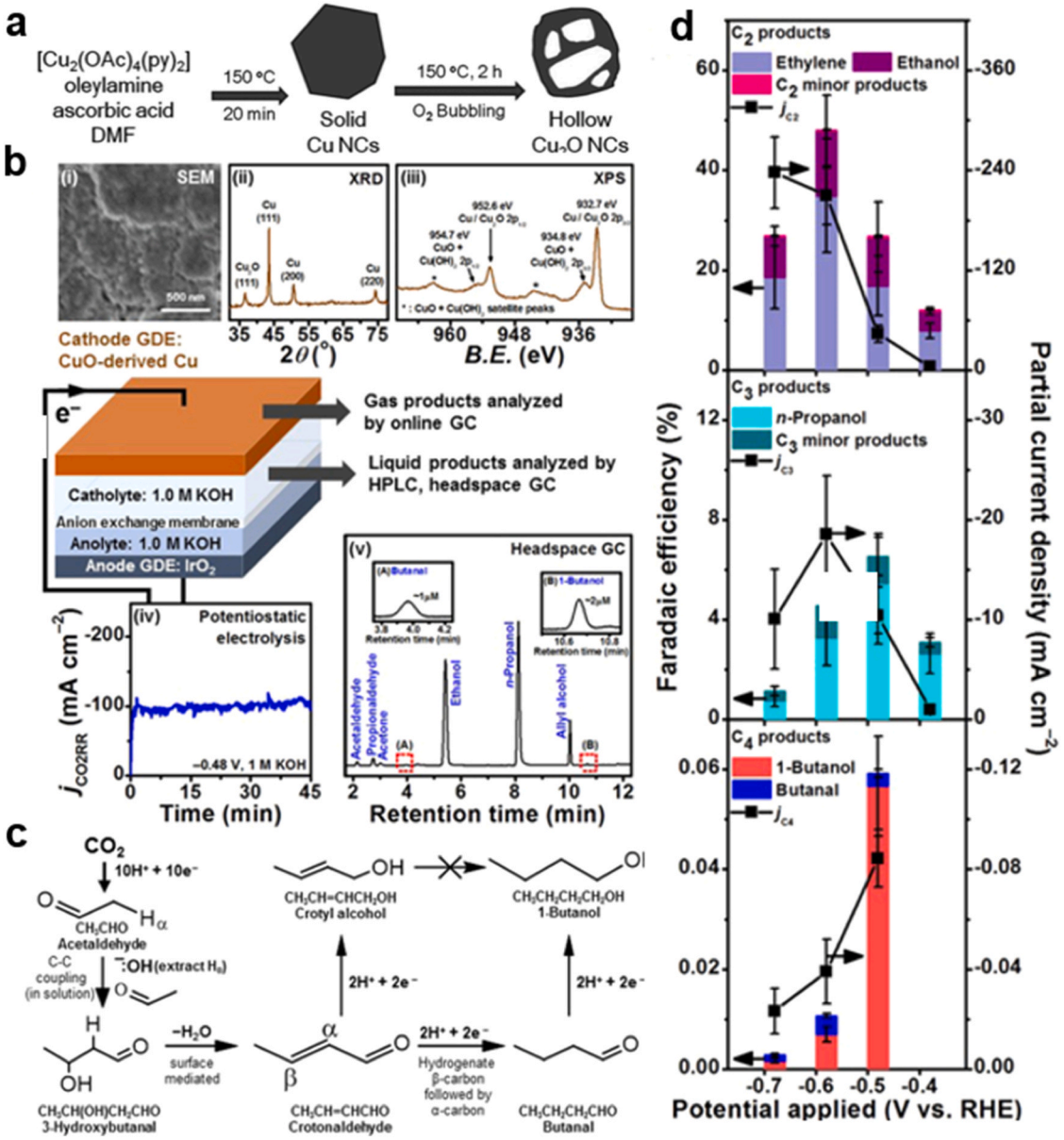

Fig. 4. **a** Schematic illustration showing morphology variation of Cu HNCs as the reaction proceeds for different periods [59]. Copyright 2022, Royal Society of Chemistry. **b** Diagram of CO_2 flow cell electrolysis setup: characterization of CuO-derived Cu cathodes by (i) SEM, (ii) XRD, and (iii) XPS (iv) large CO_2 reduction current densities (v) sensitive headspace GC can quantify minor products down to the μm-scale. **c** Reaction scheme for CO_2 reduction to 1-butanol. **d**FE and partial current densities of C_2, C_3 and C_4 products. Reproduce with permission [67] Copyright 2020, Welly.

advantages. Different types of Cu oxides can be obtained through simple alkaline treatments or hydrothermal methods. These differences may lead to variations in the surface roughness of copper and the under-coordinated Cu sites after electroreduction, leading to the selectivity of Cu catalysts' final products (C_2 or C_{3+} products) being different.

Zhang et al [59]. crafted Cu_2O hollow nanocages (HNCs) through an in situ oxidative etching methodology, whereby Cu precursors underwent a high-temperature reduction to generate polyhedral Cu nanocrystals, followed by in situ oxidative etching into hollow interiors via oxygen gas bubbling (Fig. 4**a**). This reduction process for Cu_2O HNCs augmented the number of defect sites and stepped facets in the material, FE of n-propanol reached 8.21 % under −1.1 V vs. RHE. In a parallel study, Yeo et al [60]. fabricated Cu_2O catalyst films with various thicknesses and morphologies via a hydrothermal approach. These oxide films were pre-reduced to Cu(0) catalysts, which were then employed for CO_2RR. They discovered that following pre-reduction, micro-sized Cu_2O particles converted into Cu_2O-derived Cu nanoparticles, with the crystallite size of the particles decreasing from 41 nm to 18 nm. The small Cu nanoparticles led to an increase in the specific surface area, the creation of numerous grain boundaries, activation of sites, and ultimately stronger adsorption of CO on the Cu active sites. The resultant FE was 5.4 % for n-propanol at −1.7 mA cm^{-2}. Not only does the size of the catalyst Cu-OD copper nanoparticles affect the selectivity of the C_{3+} product, Yeo's team [67] further demonstrated that the local microenvironment under electrolysis also affects the production of the C_{3+} product. They reported the generation of C_4 oxygenates by alkaline electrolysis of CO_2 in a flow cell using a CuO-derived Cu gas diffusion electrode (GDE) (Fig. 4**b**). As obtained by combining reaction product analysis of possible intermediates of electrolysis with DFT studies, the formation of the key C_4 intermediate crotonaldehyde ($CH_3CH{=}CHCHO$) can be traced back to the aldol condensation of two acetaldehyde (CH_3CHO) molecules produced by carbon dioxide electroreduction (C-C bond formation) (Fig. 4**c**). At the same time, OH^- ions in the electrolyte, localized alkaline pH facilitate the initial C-C coupling step between the two acetaldehyde molecules and promote the generation of C_4 long chains, with the Cu surface contributing to the subsequent dehydration step of crotonaldehyde, and consequently to the generation of 1-butanol on copper, an FE = 0.056 %, $j_{1\text{-butanol}}$ = -0.080 mA cm^{-2} achieved at −0.48 vs RHE (Fig. 4**d**). However, although the authors demonstrated for the first time the generation of C_4 long chains by the Cu-OD method, due to factors such as the low activity of acetaldehyde reduction to 1-butanol on copper material, while the promotion of C-C coupling and dehydration steps must be copper-based catalysis, resulting in selectivity of 1-butanol is low which constrained by the limitations of traditional one-pot methods. Therefore, to develop multi-carbon products effectively, employing efficient tandem catalysts [68,69], or tandem cells [70,71] might be a preferable option.

Meanwhile, Tang et al [46]. employed Cu_2O and CuO with diverse valence states by oxidizing Cu foils in different concentrations of NaOH, finding that CuOD-Cu possessed a significant n-propanol catalytic efficiency of up to 17.9 % FE, whereas the main product on Cu_2OD-Cu electrode was formate. (Fig. 5**a**) Moreover, the CuOD-Cu shows a top performance with high FE and low overpotential compared to other CO_2RR reports (Fig. 5**b**), with the FE of n-propanol maintained at 15 %

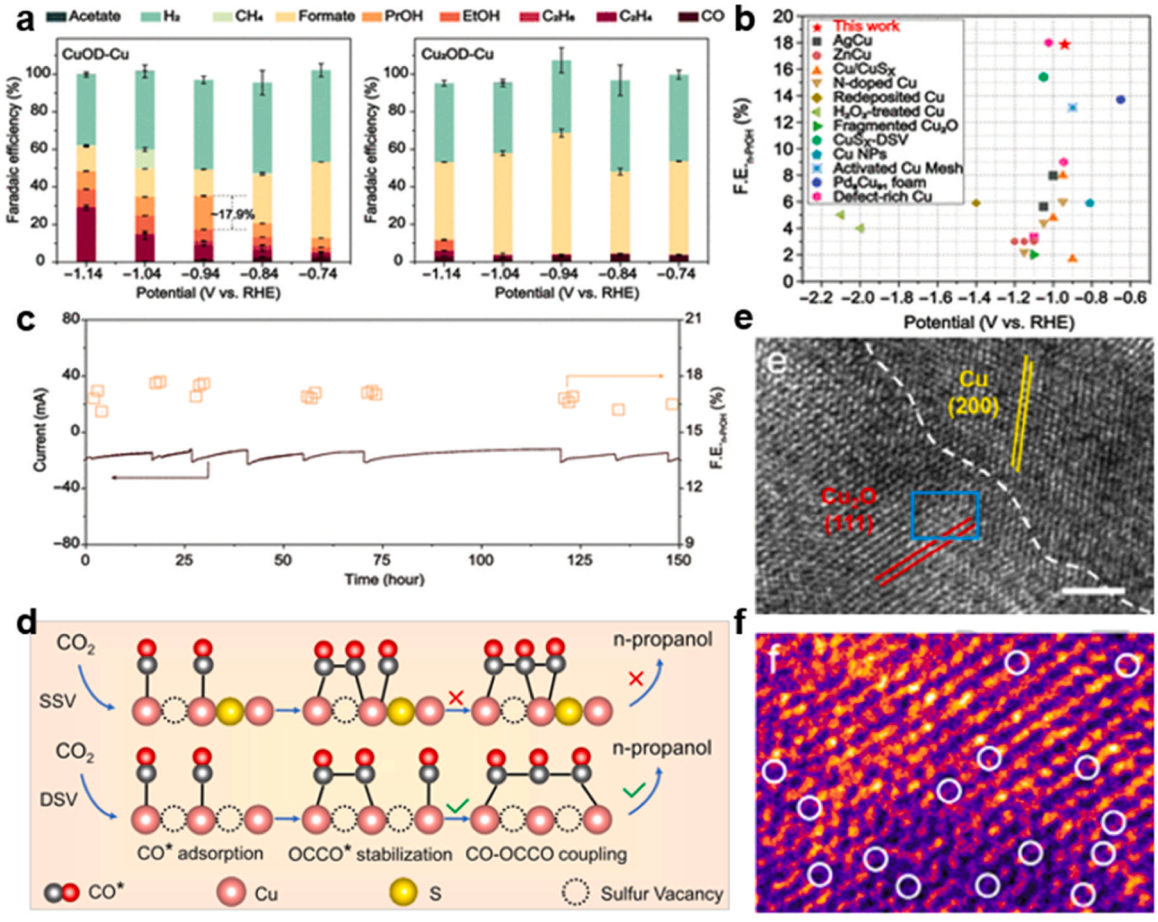

Fig. 5. **a** F.E. of products on CuOD-Cu (left) and Cu_2OD-Cu (right) during CO_2RR in H cell. **b** Performance comparison of the work with the state-of-the-art results. **c** Long-term stability measurement of CuOD-Cu [46]. Copyright 2023, Science (AAAS). **d** Mechanism of n-propanol formation on adjacent CuSx-DSV, showing the dimerization of CO-CO followed by CO-OCCO coupling [80]. Copyright 2021, Springer Nature. **e** HRTEM image, **f** enlarged color view of the blue rectangle in **e** Reproduce with permission[79] Copyright 2024, Welly.

after 150-hour continuous CO_2RR at −0.94 V vs. RHE (Fig. 5**c**). Although the authors noted that the CuOD-Cu catalysts preferred n-propanol in terms of selectivity, they also derived through molecular dynamics simulations that the reason for the generation of n-propanol was because CuOD-Cu possessed a rougher surface, (i.e., a higher density of surface Cu atoms) as compared to Cu_2OD-Cu, which is agreeable to the view of YeO et al [60]. Moreover, the SiO_2-mediated $Cu^+/Cu(0)$–NH_2 composite interface further enhanced the CO_2 reduction performance. Wang et al [72]. coated a porous SiO_2 layer on Cu_2O nanoparticles and subsequently modified the SiO_2 surface with an -NH_2 functionalized silane coupling agent. The strong interfacial interaction between SiO_2 and Cu_2O induced the oxidation of low valence Cu, allowing part of Cu^+ to remain in its oxidized state even during CO_2RR, ultimately forming a $Cu^+/Cu(0)$ interface. Additionally, SiO_2 acted as a bridge connecting Cu species with -NH_2 functional groups, constructing a Cu-NH_2 composite catalytic interface. This synergistic interaction enhanced CO_2 adsorption and activation, facilitated CO intermediate formation, and accelerated C-C coupling at the $Cu^+/Cu(0)$ interface. Actually, it is worth noting that the more abundant undercoordinated Cu sites are also crucial for the generation of n-proponal. DFT results revealed that the most favorably converted $*C_2$ intermediate on the surface of the CuOD-Cu catalyst is *HOCCOH. *HOCCOH is thermodynamically more preferred to be coupled to *CO, which favors the formation of $*C_1$ and $*C_2$ intermediates, allowing for C-C coupling not only between *CO and *CO but also between *CO and $*C_2$ [38,73]. In addition to the regulation of Cu oxides, researchers have found that the asymmetric sites formed by Cu^+ and Cu(0) play a critical role in stabilizing *CO and *OCCO intermediates and promoting *OC-COCO coupling to produce n-propanol [74–77]. As a result, studies focusing on controlling the oxidation states of copper ($Cu^+/Cu(0)$) to enhance C_{3+} yield are increasingly gaining attention. However, in the electrochemical CO_2RR, Cu^+ is inevitably reduced to Cu(0), which leads to a decrease in the content of Cu^+, thereby affecting the catalytic performance and electrochemical stability. Scientists have tried various methods to maintain the relative stability of Cu_2O during the CO_2RR process [74,78–80]. Zheng et al [80]. created double sulfur vacancies on the hexagonal CuS (100) planes by lithium electrochemical tuning method (Fig. 5**d**). This high density of dual sulfur vacancies not only effectively adjusted the ratio of Cu^+/Cu in the catalyst but also reduced the Cu-Cu distance. As a result, the FE for n-propanol production in H-cells increased to 15.4 %, and the partial current density for n-propanol production in flow cells further increased to 9.9 mA/cm^2. Duan et al [79]. successfully synthesized a catalyst with a bicontinuous structure, b-Cu_2O/Cu, by electrochemically reducing $Cu(OH)_2/CuO$. This structure consists of ultra-small nano-domains smaller than 10 nm (Fig. 5**e, f**). Analyses using X-ray diffraction (XRD), X-ray absorption spectroscopy (XAS), and X-ray near edge structure (XANES) show that the Cu valence state in b-Cu_2O/Cu remains stable during electrolysis, with a dynamic transition occurring between Cu^+ and Cu(0). Furthermore, X-ray photoelectron spectroscopy (XPS), Cu LMM, and electron paramagnetic resonance (EPR) results indicate that there are abundant oxygen vacancies in the b-Cu_2O/Cu catalyst. These oxygen vacancies likely originate from the bicontinuous structure composed of Cu_2O nanodomains, metallic Cu nano-domains, and numerous Cu_2O-Cu interfaces. This dynamic transition of Cu valence states allows b-Cu_2O/Cu to demonstrate a significantly high FE for n-propanol ($FE_{n\text{-propanol}}$=16.2 %) and good electrochemical stability, maintaining performance for 10 hours at −1.4 V vs. RHE. Atomically dispersed Cu_xO can simultaneously induce the formation of a large number of oxygen vacancies with strong Lewis acid activity, with the assistance of the porous tubular electrode, directional gas transport is realized, constructing a rich gas-liquid-solid three-phase reaction interface, which could enhance the activity and selectivity of the catalysts [81]. In contrast, n-Cu_2O/Cu nanoparticles[79] with an average size of 54.4 ± 4.2 nm, fabricated via $NaBH_4$ reducing, only achieved an FE of 4.2 % at the same voltage and showed a poor stability. Although methods such as increasing oxygen vacancies have been used to improve electrochemical stability, further enhancing stability by integrating changes in the microenvironment during the electrochemical process remains a challenge that requires additional research [82,83].

In addition to maintaining the $Cu^+/Cu(0)$ state through oxygen vacancies, doping copper catalysts with secondary metals or heteroatoms such as sulfur, boron, and halides can also effectively delay the depletion of Cu^+ and promote C-C coupling reactions [44,77,84–86]. Wang et al [85]. designed a Cu-CuI composite catalyst with a rich $Cu^+/Cu(0)$ interface by physically mixing Cu nanoparticles and CuI powder. Under the potential of −1.00 V vs. RHE, this catalyst demonstrated good electrochemical performance in producing n-propanol, with an FE of 6.9 %. Structural characterizations before and after the reaction indicated that the Cu-CuI composite catalyst underwent significant reconstruction under CO_2RR conditions, with residual Cu^+ and adsorbed iodine on the catalyst surface likely facilitating the rapid generation of C_{2+} products. Wang et al [44]. prepared copper catalysts modified with different halogen elements (F-Cu, Cl-Cu, Br-Cu, I-Cu) via hydrothermal methods and found that the production rate and FE of C_{2+} products significantly increased as the halogen electronegativity increased (Fig. 6**a, b**). Cu LMM Auger spectra and X-ray absorption near edge structure measurements displayed the co-existence of the Cu (0) and Cu^+ on X-Cu catalysts, and with the increase in halogen electronegativity, the proportion of Cu^+ sites increased, and the adsorption capacity of CO enhanced (Fig. 6**c, d**), ultimately achieving an n-propanol FE of up to 6.4 %. Additionally, Zheng et al [86]. co-modified the Cu surface in situ with halide anions and alkali metal cations, choosing $KCuF_3$ perovskite as the precursor and reconstructing it into surface F-bonded, single K-doped Cu(111) nanocrystals to create the K-F-Cu-CO_2 catalyst, which can suppress the formation of H_2 and CH_4, enhancing the FE of n-propanol to 4.7 % (Fig. 6**e**).

Apart from halide ions, boron-doped copper (Cu-B) catalysts exhibit strong binding capabilities with CO due to the introduction of boron, which alters the electronic state densities of Cu3d and C2p on the copper surface, resulting in a stronger CO binding energy. This alteration in electronic structure results in the copper atoms in the boron-doped regions having a higher positive charge, thereby effectively promoting C-C coupling and CO dimerization reactions [77]. Einaga et al [87]. observed that under ambient temperature and pressure conditions, boron-doped diamond (Cu-BDD) electrodes can effectively reduce CO_2 to acetone at −1.0 V vs. Ag/AgCl, demonstrating an FE of 7 %. Simultaneously, Cai et al [88]. reported that through online gas chromatography (GC) analysis, chemically plated Cu-B suppresses the direct release of CO and the formation of CH_4 via the CHO pathway on the copper surface, thereby promoting CO C-C coupling to form more multi-carbon products, allowing the Cu-B catalysts to directly produce n-propanol with an FE of 7.1 % at −1.15 V vs. RHE. Additionally, phosphorus-doped Cu (Cu-P) also demonstrated the production of n-propanol under the same conditions with an FE of 5.1 %, attributed to phosphorus's low electronegativity (P: 2.19) and strong electron-withdrawing capability, which helps stabilize the $Cu^+/Cu(0)$ surface state. Thus, by adjusting the doping ratio of boron and phosphorus in Cu catalysts, enhancing catalyst performance and selectivity, further optimization of the generation of C_{3+} products during CO_2RR can be achieved [89].

3.1.2. *Thermal annealing*

Thermal annealing of copper-based catalysts leads to significant changes in their structure and chemical states, primarily manifesting as secondary mesopores within the pore sidewalls of the copper catalysts. Following redox reactions, the internal restructuring of the copper catalyst introduces additional lattice distortions and defects, creating interfaces enriched with high surface energy favorable to produce C_3 products during CO_2RR. The formation of Cu^{2+}, Cu^+, and $Cu^{\delta+}$ can be controlled by varying the annealing temperature and time and some researchers believe that $Cu^{\delta+}$ is a dynamic valence state caused by CuO/

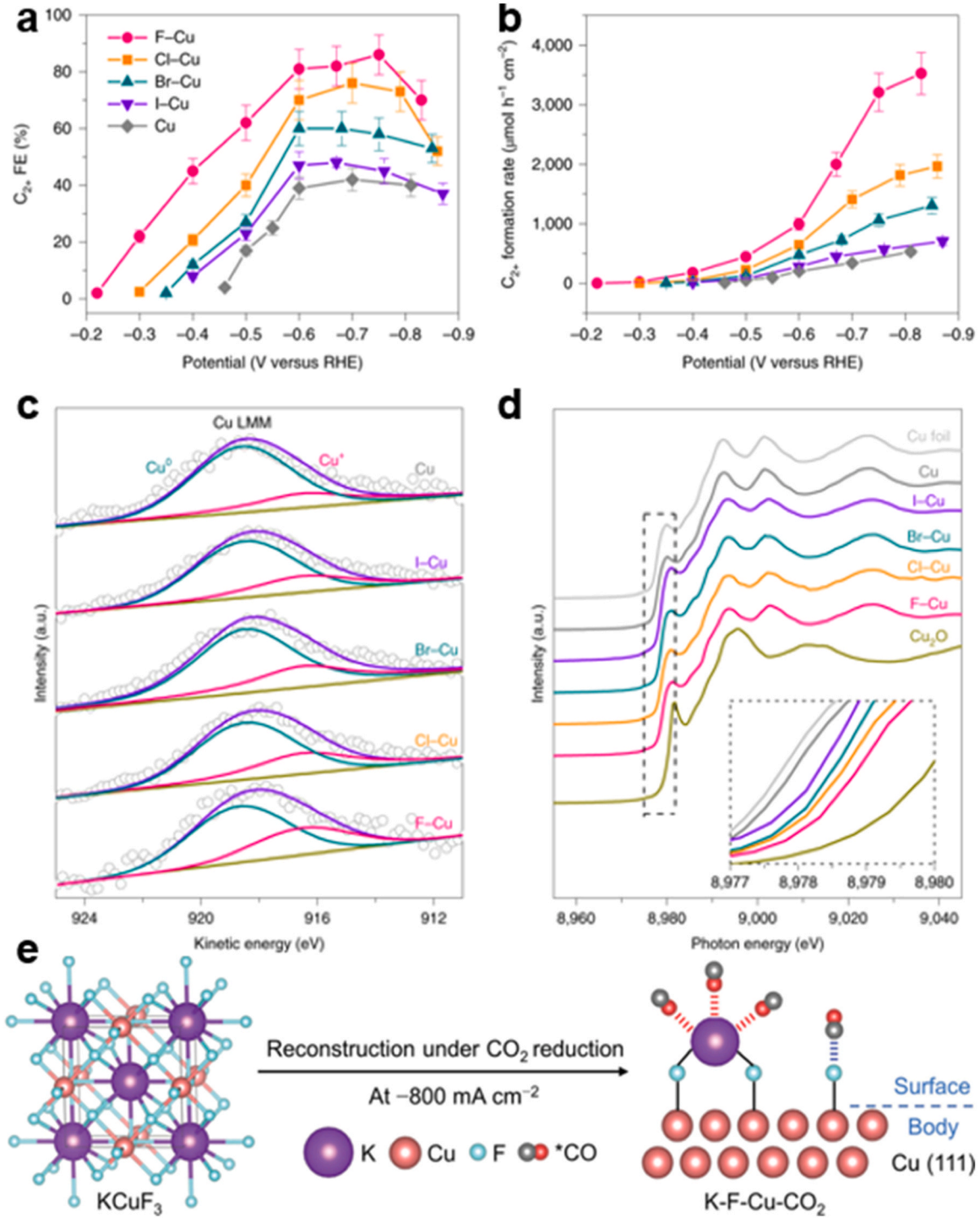

Fig. 6. **a** The FEs of C_{2+} products under different applied potentials over X-Cu catalysts in 1 M KOH. **b** The formation rates of C_{2+} products under different applied potentials over X − Cu catalysts in 1 M KOH. **c** Copper LMM Auger spectra of the X − Cu catalysts. **d** In-situ copper K-edge X-ray absorption near edge structure spectra of X-Cu catalysts at −0.6 V vs. RHE in 1 M KOH [44]. Copyright 2020, Springer Nature **e** Scheme of surface F and K co-modified Cu(111) with adsorbed *CO intermediates for K-F-Cu-CO_2. Reproduce with permission[86] Copyright 2024, Welly.

Cu_2O on the surface and determined by different contents [90]. After annealing, the $Cu_\delta O$ nanoparticles dynamically restructure during electrochemical reduction [91], evolving into smaller Cu nanoparticles with rich grain boundaries, which promotes the interconnection of surface grain boundaries and active crystal planes, affecting CO adsorption and C-C coupling steps [92]. Some researchers also proposed that annealed copper catalysts can better avoid the accumulation of poisoning carbon species on the surface compared to electroplated catalysts [93], thus enhancing the production of C_{3+} products. Broekmann et al [61]. modified copper mesh through electrodeposition and thermal annealing, achieving an FE of 13.1 % for n-propanol production and forming propylene during CO_2RR at −0.9 V vs. RHE with a current density of -1.33 mA cm^{-2}. Notably, although only a small amount of propylene is produced (FE_{C3H6} <2 %), this also proves the possibility of electroreduction of Cu-OD copper catalyst to propylene. The increase in FE_{C3H6} may be related to the catalyst's crystal face and surface active

sites [39].

Dutta et al [94]. electrodeposited copper foam on an activated carbon foil substrate, followed by annealing in air for 12 h at 300 °C to form a CuO/Cu_2O stage catalyst. Ultimately, the reductive degradation of the formed Cu-oxide precursor triggers morphological changes at the nanoscale, including the appearance of smaller nanoparticles and nanocavities on the dendritic foam structure. Identical location (IL) scanning electron microscopy (SEM) analysis demonstrated an increase in the electrochemical active surface area (ECSA), with newly formed Cu nanoparticles and nanocavities affecting the ECSA by altering the density of low-coordinated surface sites and grain boundaries (Fig. 7**a-f**). This promoted C-C coupling reactions, thereby enhancing the formation of C_{3+} products, resulting in an FE of 8.21 % at −1.72 mA cm^{-2} under the potential of −0.87 V vs. RHE. Kang et al [95]. utilized the highly reactive N radicals of the N_2 plasma to produce interstitial nitrogen atoms in the CuO crystals, which effectively regulates the binding energy between Cu and *CO intermediates. However, some researchers proposed that the presence of Cu_2O nanoparticles indeed enhances the selective C-C coupling in the carbon dioxide reduction reaction [96]. Furthermore, by adjusting the ratio of Cu^+/Cu (0) on the Cu surface, the forming of Cu^+/Cu (0) interface lowered the energy barrier of the original Cu(111) surface [97]. Therefore, annealing leads to the reconstruction of multiple grain boundaries for the same metal or different metal phases [98]. Based on this, Broekmann's group[62] took advantage of the characteristics of Pd, which are conducive to the formation of *CO, and synthesized an alloy with a total composition of 9 % Pd and 91 % Cu through electrodeposition. Subsequently, the prepared metal alloy foam was converted to an oxidized state through thermal annealing, resulting in oxidized catalyst precursor being reduced pre-electrochemically to return to the metal state, achieving an FE of 13.7 % for n-propanol at −0.65 V vs. RHE with a current density of −1.15 mA cm^{-2}. Ex situ XRD and IL SEM revealed that this continuous process from metal to oxide and then subsequent reduction to metal indeed involved phase restructuring, with the surface nano-separating into Pd-rich and Cu-rich domains, where Pd-rich domains facilitated *CO formation and *H production, while Cu-rich domains were optimal for C-C coupling. (Fig. 7**g-t**) The reduced metal state of Pd_9Cu_{91} was also proven to have an increased ECSA and surface roughness of Cu nanoparticles compared to the precursor, indicating that the Cu-OD process improved the catalyst's geometric surface area through nanostructural modification, inducing high local current densities. Furthermore, the catalytic activity of high-temperature annealed OD-Cu stems from specific Cu sites. The magnetization of Cu ultimately achieved the antiparallel spin arrangement of electrons, promoting C-C coupling at Cu-Cu sites, thus producing C_{2+} [99]. High FE for n-propanol primarily because the Cu-Cu sites completely suppressed the formation of methane and other C_1 hydrocarbon pathways, promoting the formation of stable C_2 intermediates that combine with CO [100].

3.1.3. *Oxygen plasma exposure & halogen anion treatment*

Oxygen plasma treatment is a simple and scalable technique that can grow predictable oxide structures under very mild conditions [101]. It is also an effective method for activating catalysts, creating defects, or embedding atoms, thereby enhancing reaction activity [102]. Owing to its ability to quickly change the surface oxidation state at room temperature, producing nanostructured oxide layers with adjustable morphologies, many researchers applied this technique for reducing CO_2 to C_{3+} products. Cuenya et al [63]. utilized oxygen plasma treatment to

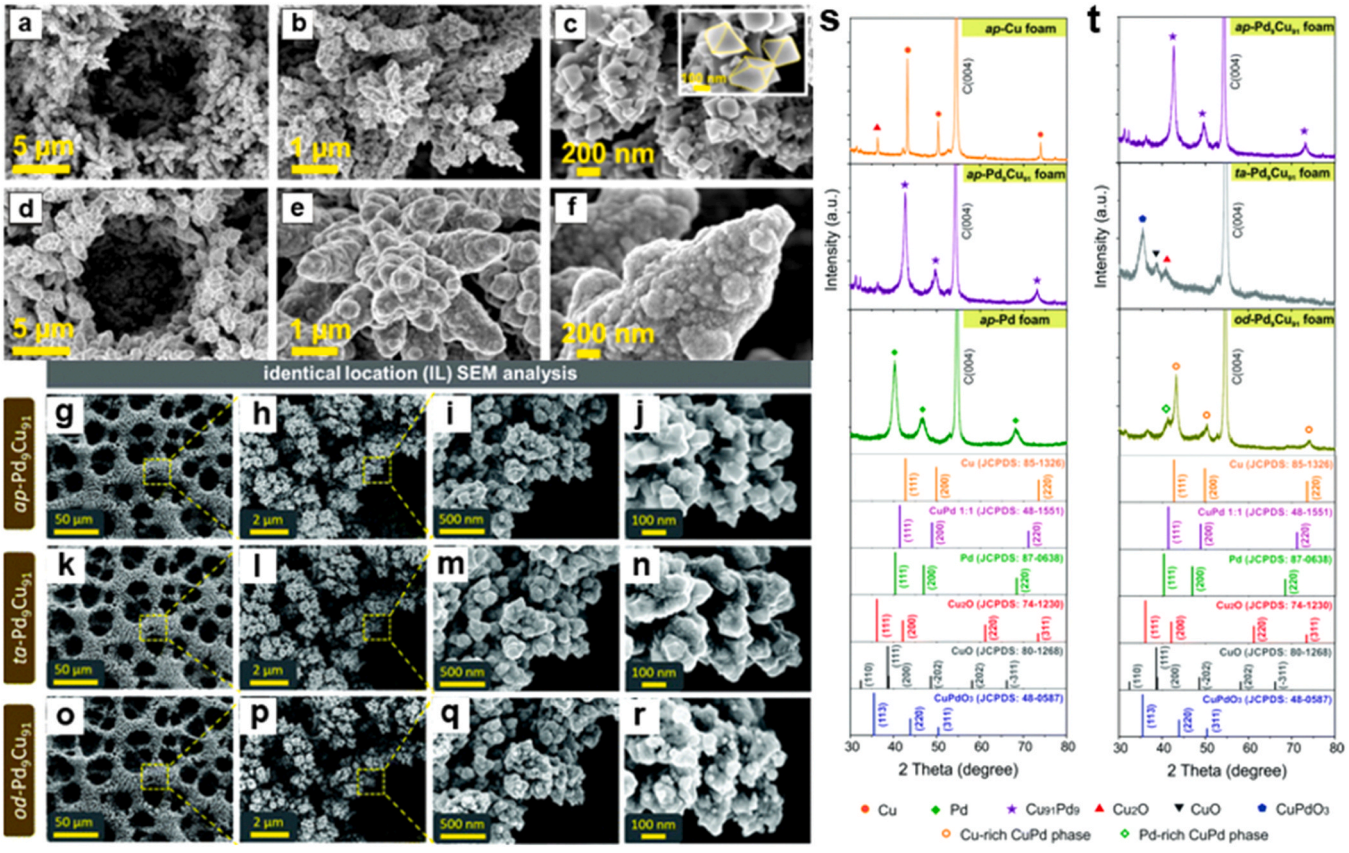

Fig. 7. **a-c** SEM micrographs of the as-deposited Cu foam; **d-f** SEM micrographs of the thermally annealed Cu foam (300 °C, 12 h, in air) denoted as Cu_xO foam.9 [4] Copyright 2020, Elsevier. IL SEM analysis of the co-alloyed foam catalyst depending on the processing stage; **g-j** as-prepared (*ap*) alloy foam; **k-n** thermally annealed (*ta*) alloy foam. **o-r** oxide-derived (*od*) alloy foam; **s** XRD of the *ap* pure Cu, pure Pd, and the Pd_9Cu_{91} foam samples; **t** XRD of the Pd_9Cu_{91} sample depends on the processing stage *ap*, *ta*, and *od*.6 [2] Copyright 2020, Royal Society of Chemistry.

develop a Cu nanocube catalyst with adjustable Cu(100) facet structures and ionic (O^{2-} and Cl^-) levels. By controlling the compositions of oxygen plasma, they discovered a strong correlation between the oxygen content within the copper nanocubes and their corresponding catalytic performance and selectivity for n-propanol. The results indicated that after O_2 plasma treatment, the catalysts gained a higher subsurface oxygen content during the oxidation phase, which stabilized the underground strata of Cu nanocubes, leading to the formation of Cu_xO or subsurface oxides. This resulted in lattice strain within the relatively oxygen-deficient surface layers of the copper nanocubes [103]. Moreover, unique defect sites created during the O_2 plasma oxidation phase of the Cu-based catalyst were considered key factors for achieving exceptional activity and selectivity for n-propanol. The plasma treatment caused chemical and physical changes to the Cu surface, altering the surface morphology, and achieving controllable surface roughening [104]. Bell et al [105]. compared Cu surfaces roughened by plasma pretreatment with Ar, O_2, and nitrogen N_2 to electrochemically polished Cu samples in terms of activity and product selectivity. They found a higher proportion of low-coordination Cu sites on the roughened surfaces, which favored the adsorption of *OC-COH and promoted C-C coupling. Compared to electrochemically polished Cu, Cu pretreated with Ar or O_2 plasma showed more than an order of magnitude decrease in CO production rate, while C_3 products, (acryl alcohol and n-propanol), were increased by a factor of 3–5, with $FE_{C3products}$ approaching 10 %. The adjustment of surface roughness increased the ECSA and regulated the surface orientation, such as Cu(100), creating surface defect sites to provide low-coordination Cu sites, making them kinetically favorable [106]. Based on the potential of the unique square configuration of Cu(100) in promoting C-C coupling, especially in the formation of n-propanol, Cuenya team [107] has focused on this surface orientation and its interaction with surface defect sites and the Cu^+/Cu (0) ratio. Through a meticulously designed pulsed electrolysis method, they not only adjusted the morphology and oxidation state of the copper catalyst but also enhanced the activity of the Cu(100) surface through roughening treatment, while precisely controlling the Cu^+/Cu(0) ratio. Furthermore, by carefully selecting the anodic potential, they achieved continuous in situ regeneration of Cu^+, optimizing the dynamic balance of the catalytic process. These innovatively designed experimental parameters allowed the faradaic efficiency of n-propanol to reach 5.5 % under the conditions of −1.0 V vs. RHE, demonstrating significant potential in improving yield and selectivity. However, when designing catalysts roughening, the impact of the microenvironment must also be considered. Research by Raciti et al [108]. indicated that high current densities observed on highly roughened electrocatalysts can rapidly increase pH. Higher pH values reduce proton concentration and suppress the formation of C_1 products, favoring *CO-CO coupling and thus promoting the formation of C_{2+} products [109,110]. However, high pH can also reduce the local CO_2 concentration, and the limited amount of CO_2 dissolved on rough electrode surfaces may decrease the efficiency of electrochemical CO_2RR [111]. Therefore, optimizing the kinetics of CO_2RR by adjusting factors such as surface roughness and local pH to overcome kinetic barriers is crucial for the formation of C_{3+} products.

The introduction of halide ions promotes the formation of copper-halide compounds under oxidizing conditions, which subsequently convert to CuxO and are further reduced to Cu nanoparticles under reducing conditions. Kwon et al [66]. electrolytically polished polycrystalline copper, subjecting it to anodic corrosion in KCl solution and generating a layer of Cu_2O on the surface. It is followed by a pre-reduction process, forming irregular copper nanoparticles with an approximate diameter of 20 nm. After treating these catalysts with CO_2RR at low overpotentials, a total of nine C_2 and C_{3+} products were produced. Lee et al [65]. utilized the chemical affinity between chloride ions (Cl^-) and Cu to in situ generate a Cl-induced biphasic Cu_2O-Cu (Cu_2OCl) catalyst. They realized this by applying cathodic potential for a CO_2 electrolysis system to form various phase structures. Within the CO_2RR range of −0.6 to −1.8 V vs. RHE, C_{3+} products were obtained, with an FE of 8.7 % for n-propanol. The XPS and XANES spectrums, confirmed that Cl^- acts as a retardant in the reduction of Cu_2O to metallic copper, and a relatively high ratio of Cu oxidation states (Cu^+ and Cu) favors the adsorption of *CO, resulting in a more stable coverage of various intermediates on the catalyst surface, preserve the reaction intermediates for a longer time on the surface, which facilitate the formation of C_{3+} products (Fig. 8**m**). Moreover, the anodic halogenation of electropolished copper, followed by alkali-induced oxide formation, is conducive to stabilizing the Cu_2O on the surface and subsurface oxygen species. Based on this, Palmore et al [112]. observed that copper underwent morphology modification during anodic halogenation and subsequent oxide formation and reduction processes, resulting in a catalyst with a high density of defect sites. SEM and EDS analyses of the morphological and chemical changes clarified that the high-density defect sites on the surface were from surface reconstruction caused by the oxide formation and electro-reduction processes (Fig. 8**a-l**). EDS also provided evidence that subsurface oxygen at Cu_KCl, Cu_KBr, and Cu_KI defect sites was produced by the localized high pH values of the electrolyte oxidizing the copper (Fig. 8**n-u**). These factors promoted the formation of C_3 products, including n-propanol, propionaldehyde, and allyl alcohol. Moreover, the doping of elements with strong electronegativity facilitates electron transfer from Cu to the dopant atoms, causing changes in the chemical states and electronic structures of the catalyst [58,113]. Zhang et al [114]. synthesized a copper-based metal-organic complex using $CuCl_2$ as the metal precursor and triethylamine (TEA) as the organic ligand, preparing a chlorine-doped catalyst (R-Cu-C) with orchid leaf-shaped nanoplates through surface reconstruction under in situ electrochemical conditions, achieving an FE of 17.3 % for n-propanol at −1.05 V vs. RHE. The study shows that Cl ions not only stabilize the oxidation states of adjacent Cu sites, promoting the formation of the Cu^+/Cu(0) interface structure and maintaining the stability of the interface during the electrocatalytic process [115,116]. More importantly, these halide ions enhance the adsorption of intermediates, effectively reducing the overpotential of the electrochemical reduction reaction [117].

3.2. Cu NPs

Due to the high surface area and newly exposed activate sites, nanoparticles (NPs) catalysts typically exhibit higher activity compared to bulk surfaces. Furthermore, nanoparticles with good shape and size control can help understand catalytic activity trends and design efficient catalysts. Researchers use Cu NPs as a model to improve catalyst activity in various ways, such as changing the particle size of Cu NP [118,119], modulating the exposed surface via tuning the morphologies of Cu NPs [120], reducing Cu_xO NP to generate Cu NP in situ before catalysis [45], and increasing the loading amount of Cu NP per unit area [121]. These enhancements deepen the refinement of Cu NP catalysts, enabling them to exhibit varying selectivity in the CO_2RR.

Yang et al [121]. observed unique structural transformations in Cu NPs systems during electroreduction, using densely packed Cu NPs to selectively convert CO_2 into multicarbon products. They synthesized Cu NPs with an average size of 6.7 nm by reducing copper(I) acetate (CuAc) precursors at high temperatures using tetradecylphosphonic acid as a surface ligand. The resulting Cu NPs were deposited onto carbon paper substrates (1^{geo}_{cm2}), and as the loading increased to about 45 μg, most of the carbon paper's surface was covered with densely packed Cu NP. After electrolysis of this nanoparticle system, the copper nanoparticles aggregated within the carbon substrate, forming larger cubic particles mixed with smaller nanoparticles (10–40 nm) (Fig. 9**a**). This high-density, tightly packed arrangement of Cu NPs, coupled with a sufficiently supportive substrate, enabled an FE for n-propanol of 5.9 % at −0.81 V vs. RHE (Fig. 9**b-d**). Due to the enriched disorder within the Cu NPs, the Cu NPs system showed higher selectivity for C_{3+} products compared with crystalline copper [115]. To further understand the evolution mechanism of Cu NPs during CO_2RR, Yang et al [118]. utilized

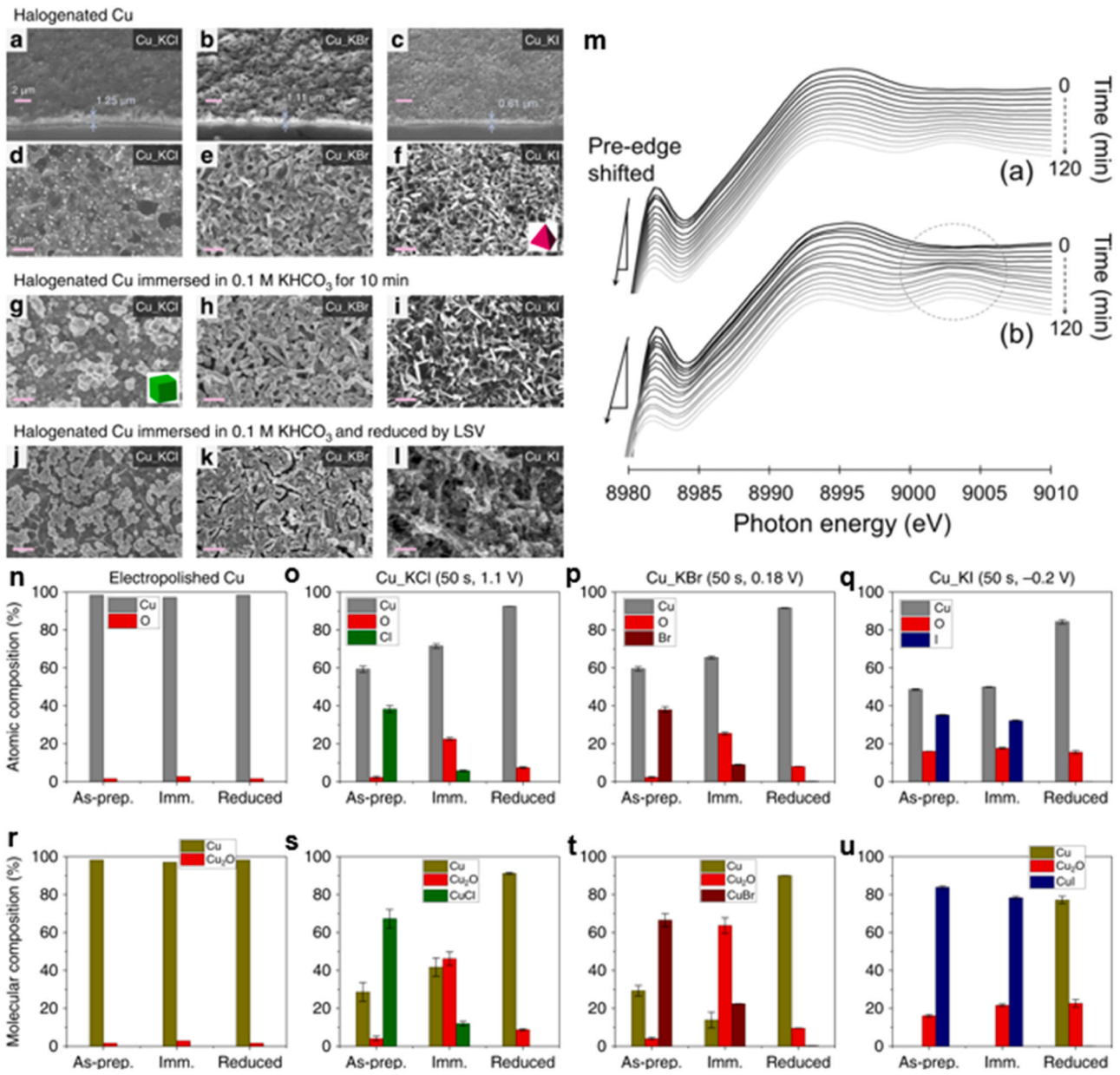

Fig. 8. SEM images of halogenated Cu foils: **a-f** as-prepared; **g-i** after immersion in 0.1 M $KHCO_3$ for 10 min; **j-l** after reduction by LSV. Scale bars: 2 μm. **n-q** EDS of raw data of atomic composition of electropolished Cu foil and halogenated Cu foils. **r-u** Compositions of molecular species from converted EDS data. 'As-prep.' indicates the as-prepared catalyst by electropolishing or anodic halogenation. 'Imm.' indicates the catalyst underwent oxide formation by immersion in air-saturated 0.1 M $KHCO_3$ electrolyte for 10 min. 'Reduced' indicates the catalyst was reduced in CO_2-saturated 0.1 M $KHCO_3$ electrolyte by LSV from its corresponding OCP to −1.8 V vs Ag/AgCl at a scan rate of 5 mV/s [112]. Copyright 2020, Springer Nature. **m** Comparison of in situ measured Cu K-edge XANES results for Cu_2O_{Cl} and Cu_2O_{OE} as a function of reaction time. Reproduce with permission[65] Copyright 2015, Welly.

various in situ testing methods to study the structural behavior, dynamic potential, and nanograin boundary limits during the CO_2RR process. They employed monodisperse Cu NPs of different diameters (7, 10, and 18 nm) as model catalysts, displaying a comprehensive structural diagram of the life cycle of high-performance copper NPs electrocatalysts (Fig. 9**e**), revealing the process of initial aggregation, transformation into Cu nanocrystals, and final formation of highly polycrystalline metallic Cu nanocrystals rich in nanoparticle boundaries. This confirmed that the unique selectivity of the Cu NP system for C_{2+} products primarily stems from the abundance of grain boundaries, supporting high-density, low-coordination active sites. However, when the Cu NP system is exposed to air, the structure rich in nanograin boundaries also activates the double bonds of oxygen molecules. This allows oxygen atoms to dissociate quickly and insert into the Cu lattice, rapidly reorganizing into well-defined single-crystal Cu_2O nanocubes. The formed nanograin boundaries contain a large number of active unmatched Cu sites, enhancing the product selectivity of Cu NPs. Therefore, by reducing the size of NPs, clusters, or molecular complexes to generate dense nanoparticle grain boundaries that support low-coordination active Cu sites, the product selectivity of Cu NPs can be enhanced. Based on this view, they demonstrated that 5 nm Cu NPs (FEn-propanol = 5.68 %, at −0.8 V vs. RHE) have a higher n-propanol FE and selectivity compared to 7 nm Cu NPs ($FE_{n\text{-propanol}}$ = 5.52 %, at −0.8 V vs. RHE). However, there is still controversy over the active state of the valence or coordination environment of Cu catalysts under CO_2RR conditions [122,123]. Yang and colleagues[123] prepared Cu nanoparticles (Cu NPs) capped with polyvinylpyrrolidone (PVP). In the absence of a capping agent, the Cu NPs were infiltrated by surface

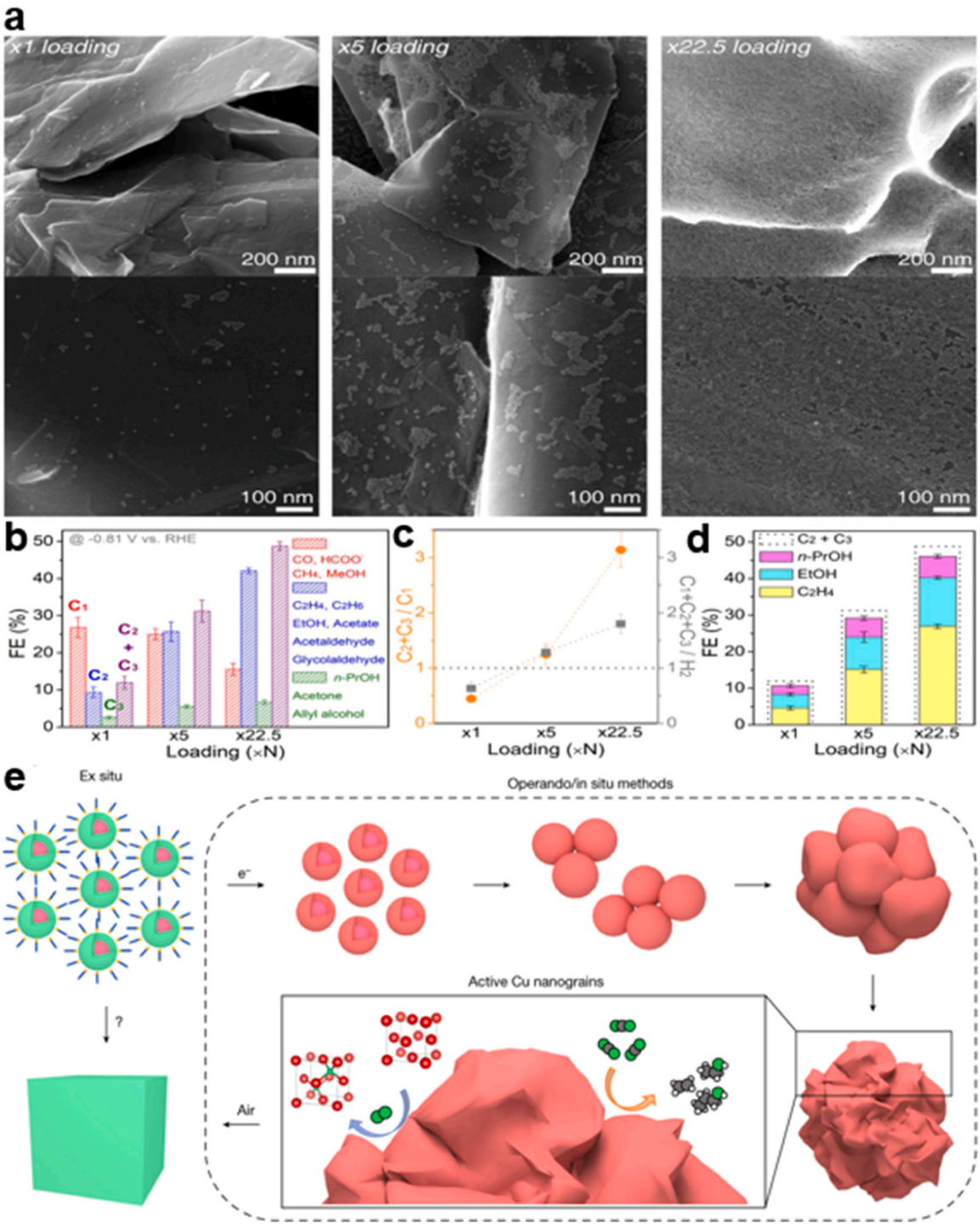

Fig. 9. **a** SEM images of Cu NPs loaded on carbon-paper support at × 1 loading, × 5 loading, and × 22.5 loading. **b** FEs (%) for C_1, C_2, and C_2 products. **c** Relative ratio of the FEs. **d** Ethylene, ethanol, and n-propanol FE with the dotted line showing the overall C_2-C_3 FE. Activity measured at −0.81 V vs. RHE, using 0.1 M $KHCO_3$ saturated under 1 atm CO_2. Error bars shown in B-D are 1 SD from three independent measurements [115]. Copyright 2020, The National Academies Press. **e** Scheme of the life cycle of Cu nanocatalysts and operando EC-STEM studies of dynamic morphological changes [118]. Copyright 2023, Springer Nature.

oxygen, forming crystalline Cu_2O/Cu NPs, which facilitated the formation of n-propanol. Conversely, fully capped Cu NPs displayed high selectivity for methane, with an FE reaching up to 70 %, and produced almost no n-propanol. However, Sargent et al [84]. employed a similar encapsulation strategy, depositing a layer of Cu nanoparticles onto a polytetrafluoroethylene (PTFE) nanofiber surface via sputter deposition, followed by a nitrogen-doped carbon (N-C) layer to fabricate N-C/Cu catalysts. Depending on the nitrogen atomic percentage in the N-C layer, catalysts with 26 %, 34 %, and 39 % N-C/Cu were synthesized. The chemical state of Cu during the CO_2RR was studied via operando X-ray absorption spectroscopy (XAS) at the Cu K-edge, revealing that Cu remained in the zero-valence state throughout the CO_2RR. This indicates that the selectivity of the N-C/Cu catalysts for n-propanol is associated with the metallic state of Cu rather than the presence of copper oxides. Additionally, increasing the nitrogen content in the N-C layer led to higher FE for n-propanol production, achieving 5.9 % for 26 % N-C/Cu,

7.7 % for 34 % N-C/Cu, and 8.6 % for 39 % N-C/Cu.

The insufficient surface coverage of *CO and the high activation barrier for C-C coupling are challenges in achieving more efficient and higher production of n-propanol from CO_2RR [121]. The instability of $*C_2$ intermediates on the original Cu surface can lead to desorption rather than further intermolecular reduction with *CO to form C_3 products [121,124]. Ren[119] et al. pointed out that n-propanol is favored only when the reactants contain both locally high concentrations of *CO and C_2H_4, coupled with a large catalytic interfacial surface area generation, whereas CO reduction will only produce EtOH [45]. Cu NPs exhibit significant selectivity and FE for C_2H_4, thus many researchers have achieved high FEs for n-propanol using Cu NPs in CO reduction. Hinrichsen et al [124]. found that using the same Cu NPs for CO reduction reaction (CORR), the FE for n-propanol was 28 %, whereas it was only 4.6 % in CO_2RR. Therefore, employing a two-step or tandem method to reduce CO_2 to CO, and then using the Cu NP system to reduce CO to n-propanol may be more effective than a direct one-step reduction [125].

In addition to the size of Cu NPs influencing the selectivity of C_3 products, the orientation of crystal facets on Cu NPs has also been confirmed to affect their selectivity for C_3 products. Wu et al [120]. synthesized five distinctly shaped Cu_2O crystal systems (Cu-OD) and constructed three interfaces: Cu (111)/Cu (111), Cu (111)/Cu (110), and Cu (110)/Cu (110) (Fig. 10 **m**). They reported that the Cu (100)/Cu (111) interface has a more favorable local electronic structure compared to the Cu (111)/Cu (111) and Cu (110)/Cu (110) interfaces, which provide more favorable conditions for the production of C_3 products. This finding is supported by the research of Ren and Gratze [39], who sputtered a CuCl precursor onto a GDL and pre-reduced the surface CuCl to Cu nanocrystals (CuNCs). Their results showed that the metallic copper nanocrystals formed from the CuCl precursor had abundant Cu (100) and Cu(111) facets, which facilitated the production of C_3 products such as propylene, n-propanol, and allyl alcohol during the CO_2RR process. The FE for propylene reached a record high of 1.42 % at a cathodic current density of 21.4 mA/cm^2 at −0.50 V, demonstrating the effectiveness of this interface. Their research also showed that after 16 hours of electrolysis, despite morphological reconstruction of the catalyst surface, the distribution of Cu(100) and Cu(111) facets remained almost unchanged (the ratio of Cu(111) to Cu(100) only decreased from 1.26 before the CO_2RR to 1.05 after CO_2RR). Therefore, how to maintain a large area distribution of Cu(100) and Cu(111) on the catalyst surface and the nearly equal distribution of these two crystal facets before and after the CO_2RR might be another important aspect to consider for producing C_{3+} products via CO_2RR.

Moreover, high-index copper surfaces or kinked surfaces (such as Cu (711)[126], Cu(751)[122]) have been found to exhibit high activity and selectivity for C-C coupling. Hahn et al [126]. discovered that the highly kinked Cu(751) surface shows remarkable selectivity and current efficiency for the synthesis of C_3 product, indicating that high Miller index kink sites on copper surfaces may possess unique properties that enhance the intrinsic activity of the catalyst. Based on this view, Liu et al. [127], with the aid of chiral molecules, generated Cu(653) chiral surfaces with chiral kink sites at the atomic level through electro-deposition of $[CuCl_4]^{2-}$ and the removal of organic components (Fig. 10 **a-k**). The study found that the chiral surfaces limit configurational changes of C_{3+} intermediates on the catalyst surface, effectively lowering the reaction barriers for the electrochemical reduction of CO_2 to synthesize C_{3+} products. Electrocatalytic CO_2 reduction studies conducted in NH_4HCO_3 aqueous solution at potentials ranging from-0.6 to −1.3 V vs. RHE for 24 hours yielded productions of serine, ethanol, and formic acid at approximately 3.8 (± 0.6) μmol, 58.6 (± 6.5) μmol, and 108.1 (± 6.5) μmol, respectively, with FE of 1.2 (± 0.2) %, 22.3 (± 2.5) %, and 6.8 (± 0.4) %. The enantiomeric excess (ee%) of serine reached 94 %, marking the first instance of direct synthesis of amino acids through electrochemical reduction of CO_2. DFT calculations were employed by researchers to analyze the pathway and mechanism of serine formation via electrocatalytic CO_2 reduction (Fig. 10 **l**). The calculations indicated that on the chiral surface Cu(653), thermodynamics favor the formation of 3-hydroxypyruvic acid intermediates and L-serine, confirming the significant role of chiral surface structures in shaping serine formation and enantioselectivity.

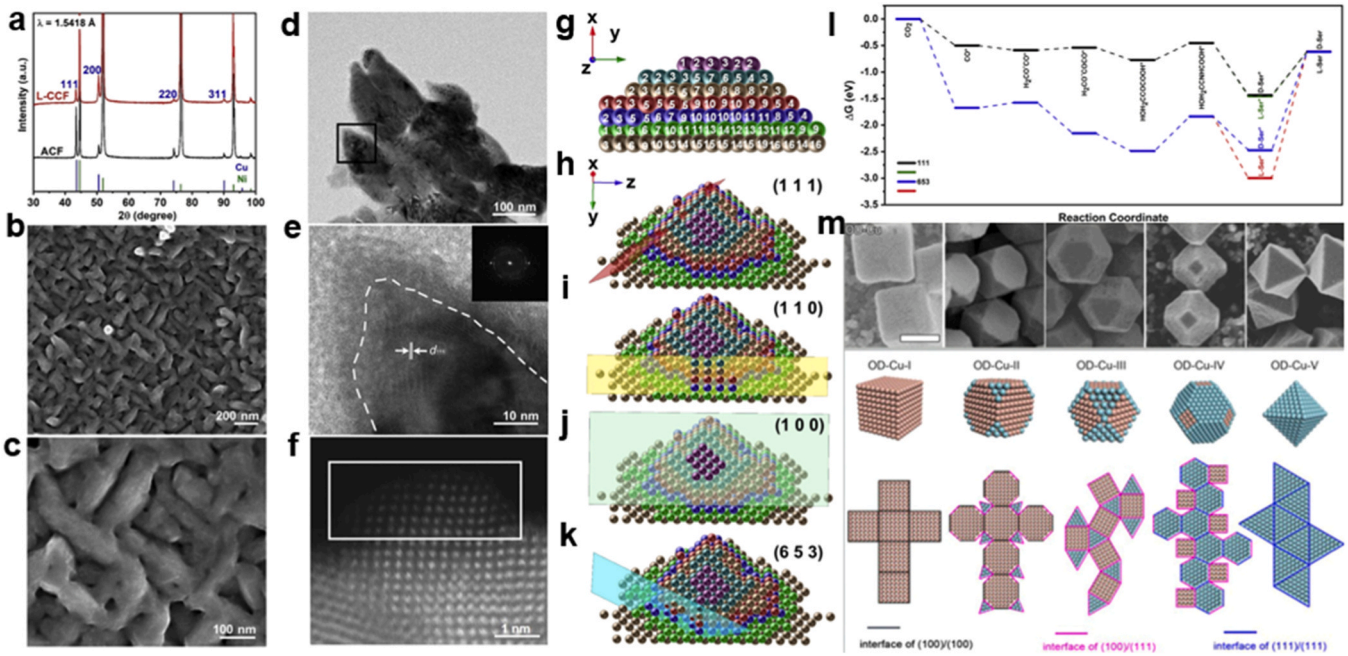

Fig. 10. a-f Morphologies and structures of L-CCFs. **a** XRD patterns of L-CCFs (red) and ACFs (black). **b** and **c** Low- and high-magnification SEM images of L-CCFs. **d** and **e** Low and high-magnification TEM images of L-CCFs. **f** HAADF-STEM image of L-CCFs. **G-k** slab surface models of (111), (110), (100), and (653) obtained from the structural model reconstructed from the STEM image of L-CCFs. **l** DFT calculations for the enantioselective formation of Ser[127] Copyright 2023, Elsevier. **m** SEM images and corresponding schematic of five Cu-OD NPs with 3 different interfaces[120] Copyright 2022, American Chemical Society.

3.3. Cu single-atom catalysts (SACs) & Cu molecular catalysts

3.3.1. Cu SACs

SACs are a special type of supported catalyst where the metal components are dispersed as single atoms without coordination between the metals. SACs can significantly optimize the electronic structure, the unsaturated coordination environment disperses the metal species into high-density active atomic centers, which have been proven to have enhanced activity and adjustable CO_2 reduction selectivity [128,129]. Metal-organic frameworks (MOFs) and covalent organic frameworks (COFs) are often used as precursors due to their abundant functional groups, stable structures, and tunable porosity, which can limit the growth of aggregates and organize metal distribution within their crystal structures [130]. Additionally, due to its excellent thermal and chemical stability, graphitized carbon nitride (g-C_3N_4) is used as a backbone for supporting metal single atoms [131]. These precursors or backbones are annealed in a nitrogen or argon flow through chemical vapor deposition (CVD) methods to remove the organic parts and serve as support frameworks that can fully anchor the metal single atoms. Since zinc has a relatively low melting point compared to other metals, zinc-containing MOFs like ZIF-8 are often used as support frameworks to synthesize copper single atoms.

Currently, researchers widely use nitrogen-doped conductive carbon with N-chelated Cu sites as the support material, which contains a mixture of coexisting pyrrolic, pyridinic, porphyrin-like, and graphitic Cu-N groups [132]. The coordination atoms significantly affect the geometric and electronic structure of Cu SACs, thereby regulating the reaction pathways and product distribution of CO_2 reduction. However,

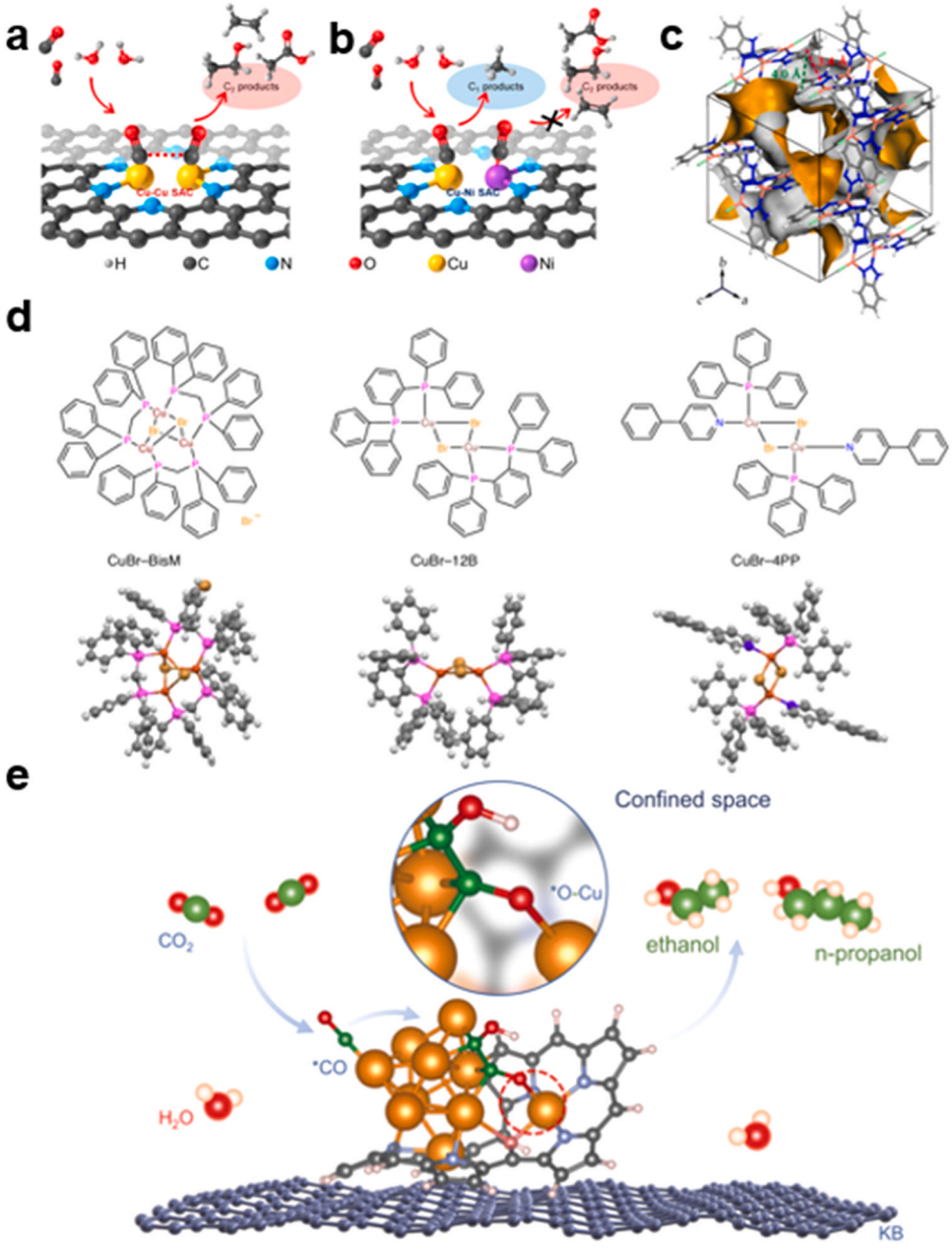

Fig. 11. Schemes of the structures and products for the eCO_2RR on **a** dual Cu-Cu and **b** Cu-Ni SACs [134]. Copyright 2021, American Chemical Society. **c** pore structure stacked by the trinuclear Cu(I) complex via π-π interactions [139]. Copyright 2022, American Chemical Society. **d** Molecular structures of CuBr-BisM, CuBr-12B and CuBr-4PP [140]. Copyright 2024, Springer Nature. **e** The proposed C-C coupling and oxygenation mechanism for producing alcohols on restructured Hex-2Cu-O. color codes: Cu, orange; C, gray (Hex-2Cu-O), navy (KB) and green (reaction intermediates); O, magenta (Hex-2Cu-O) and red (reaction intermediates); H, pink (Hex-2Cu-O) [75]. Copyright 2022, Springer Nature.

although Cu SACs are widely used to reduce CO_2 to C_1 and C_2 products, there are few reports on C_3 products. Ma et al [133]. used Ag_2S/Ag nanowires to provide initial anchoring sites for Cu single-atom catalysts (Cu/Ag_2S/Ag), then formed Cu single-atom catalysts on defective Ag surfaces through electrochemical treatment, which could produce a small amount of n-propanol at −1.0 V vs. RHE. Zheng et al. used CuBTC $(H_2O)^{134}$ as a precursor and L-glutamic acid as a nitrogen source to prepare diatomic copper catalysts, (Fig. 11**a,b**) finding that Cu-Cu favors the adsorption of neighboring CO intermediates, producing n-propanol from −1.1 V vs. RHE to −1.9 V vs. RHE. Although the current yield of C_3 product n-propanol is low in the research of Cu single-atom catalysts, these research results provide hope for future optimization of catalysts to improve C_3 product selectivity.

Chen et al [51]. synthesized Cu-doped ZIF-8 by hydrothermal method and carbonized the precursor at 1000℃ in a nitrogen atmosphere to prepare Cu-SA/NPC. They anchored atomically distributed Cu on N-doped Cu-SA/NPC and evaluated the electrochemical reduction of CO_2. Cu-SA/NPC reduced CO_2 to acetic acid, ethanol, and acetone products at low overpotential, with acetone being the main product, achieving an FE of 36.7 % and a yield of 336.1 μg/h. Interestingly, when they carbonized the synthesized precursor in an argon atmosphere to prepare Cu-SA/NPC $_{(Ar)}$ and conducted CO_2RR under the same conditions, the maximum FE of acetone dropped to less than 20 %. XPS observations revealed that although the Cu catalysts formed under the two atmospheres had similar N contents, their N species were different. The N coordinated with Cu in the nitrogen atmosphere and formed Cu-pyrrolic-N_4; in the argon atmosphere, it formed Cu-pyridinic-N_4. DFT calculations indicated that Cu coordinated with pyridinic N (Cu-pyridinic-N_4) had higher activity for acetone formation compared to Cu coordinated with pyrrolic N (Cu-pyrrolic-N_4). These findings provide new insights for designing single-atom catalysts for CO_2 reduction experiments. By adjusting different annealing atmospheres (such as NH_3), new N-Cu coordination modes can be introduced to increase the selectivity of C_3 products.

3.3.2. Cu molecular catalysts

Cu molecular catalysts consist of ligand molecules connected to Cu ions. Unlike single-metal-atom catalysts, which are typically composed of nitrogen-doped carbon and coordination polymers, molecular metal complex catalysts can freely adjust reactivity and selectivity by changing the ligand design [135]. These catalysts, with well-defined active sites and specific electronic properties, can change the electronic state of the central metal by selecting suitable organic ligands, exhibiting high activity for CO_2 reduction [136,137]. It is widely accepted that Cu-based compounds with di-Cu active sites are beneficial for C-C coupling in CO_2RR, forming C_{2+} products [138]. Chen et al [139]. constructed a trinuclear Cu(I) complex consisting of pyrazole-bridged di-Cu(I) sites and uncoordinated triazole nitrogen atoms (Fig. 11**c**), whose synergistic effect promotes C-C coupling and hydrogenation of key intermediates, resulting in the highly selective electroreduction of CO_2 to C_{2+} products, with a maximum propanol efficiency of 4 %.

Morikawa et al [140]. introduced π-conjugated substituents into the catalyst ligands to enhance the molecular catalyst's ability to adsorb and retain CO_2. They designed a series of multinuclear copper complexes, named CuBr-BisM, Cu-Br-12B, and CuBr-4PP, with a large number of π electrons and robust active sites using a bromide bridge as the ligand (Fig. 11**d**). During CO_2RR, the distance between the two bridged Cu-Cu centers of CuBr-4PP can flexibly change according to the different active sites, which facilitates attracting reducing species to one Cu side and accepting the substrate to the other Cu side, thereby promoting C-C coupling. This efficient design resulted in a propanol FE of 10 % at −2.2 V vs. Ag/AgCl, the highest efficiency among current Cu molecular catalysts. Operando X-ray absorption fine structure (XAFS) analysis confirmed that the precisely designed structure does not decompose during the CO_2 electrolysis process, and the Cu(I) oxidation state is maintained in the CuBr-4PP complex without change during CO_2RR. This stability is primarily because the accepted electrons during CO_2RR are dispersed into the phenylpyridine and CO_2-reduction intermediates, reflecting the high stability of this catalyst. This design of di-Cu molecular metal complexes, effectively accommodating microenvironmental changes during CO_2RR, while maintaining its structure and freely adjusting the electronic state of the reaction center and reaction environment, promotes C-C coupling. Combining organic copper compounds and inorganic copper ions may represent another direction for the electrocatalytic selective synthesis of C_{3+} high-value-added products. Peng et al [75]. designed the catalyst Hex-2Cu-O based on a fluorinated porphyrin structure capable of effectively binding individual intermediates to form bimetallic copper sites, which subsequently break down into copper clusters during the CO_2RR. The synergistic interaction between the under-coordinated Cu clusters and adjacent Cu centers provides a limited space with an additional O-Cu bond, facilitates C-C coupling and oxidation (Fig. 11**e**). This leads to the production of n-propanol, achieving an FE of 18.3 % at −1.2 V vs. RHE.

3.4. Cu-based tandem catalyst

Catalysts composed of metals such as Au, Ag, Pd, Bi and Zn have been proven to have the selective ability to convert CO_2 to C_1 products during the CO_2RR, while Cu-based catalysts inherently possess the unique ability for C-C coupling [141]. For heterogeneous catalysis like CO_2RR, the addition of foreign metals can modulate the atomic ensembles of adsorbate binding, induce lattice strain, and charge transfer, and alter the d-band center of the host metal, all effectively enhancing catalytic activity and selectivity [142].

Based on this principle, tandem copper catalysts are particularly suitable for generating C_3 products. These catalysts first produce *CO at non-copper metal sites such as Au, Ag, and Zn, subsequently, *CO is transferred to copper-based active sites for C-C coupling to form $*C_2$ intermediates, and finally, $*C_1$ and $*C_2$ intermediates undergo C-C coupling to produce multi-carbon products [38,143]. Therefore, using different catalysts with optimal intermediate binding energies at respective steps can significantly improve catalytic efficiency and promote an orderly reaction process. Cu-based tandem catalysts can target specific metals for reaction with a particular $*C_2$ intermediate, offering thermodynamic and kinetic advantages over traditional copper catalysts. Furthermore, through the collaborative effort of multiple sites, Cu-based tandem catalysts exhibit superior FE and current density for the reduction of CO_2 to C_{3+} products.

3.4.1. Bi- or multi-metallic and composites systems

The AgCu bimetallic catalyst demonstrates effective tandem catalysis by increasing CO coverage and shortening the diffusion path of CO to Cu through CO spillover [144]. Kim et al [145]. introduced Ag NPs into Cu_2O NPs via a galvanic replacement reaction, with an Ag content of 10 % (Fig. 12**a**). During CO_2RR, intermediates *CO generated on the Ag surface migrate to the Cu surface at the Ag-Cu interface in Ag/Cu_2O, via diffusion and/or sequential desorption-reabsorptions. This migration increases the CO coverage on the Cu surface, suppressing the HER by proton adsorption on the Cu surface and promoting C-C coupling, leading to the FE of n-propanol with 9.09 % at −0.82 V vs. RHE. Furthermore, Sohn et al [146]. introduced Sb into the AgCu bimetallic system through a galvanic replacement reaction, forming an Ag-Sb-Cu mesh electrode. This ternary system, through the synergistic action of multiple sites, increased the production of C_{3+} hydrocarbons (such as C_3H_6 and C_3H_8) during CO_2RR, with a small amount of C_4 products also being generated, indicating the unique cascade catalytic capability of multi-site catalysts.

In the reduction of CO_2 to C_3 products, the stabilization of *CO and $*C_2$ intermediates on the catalyst surface is significant for C-C coupling. It has been proved that introducing a third metal, such as Fe or Ru, can increase the retention time of *CO intermediates [147]. Sargent et al [41]. synthesized Ag-Ru-Cu catalysts by inserting Ru into AgCu

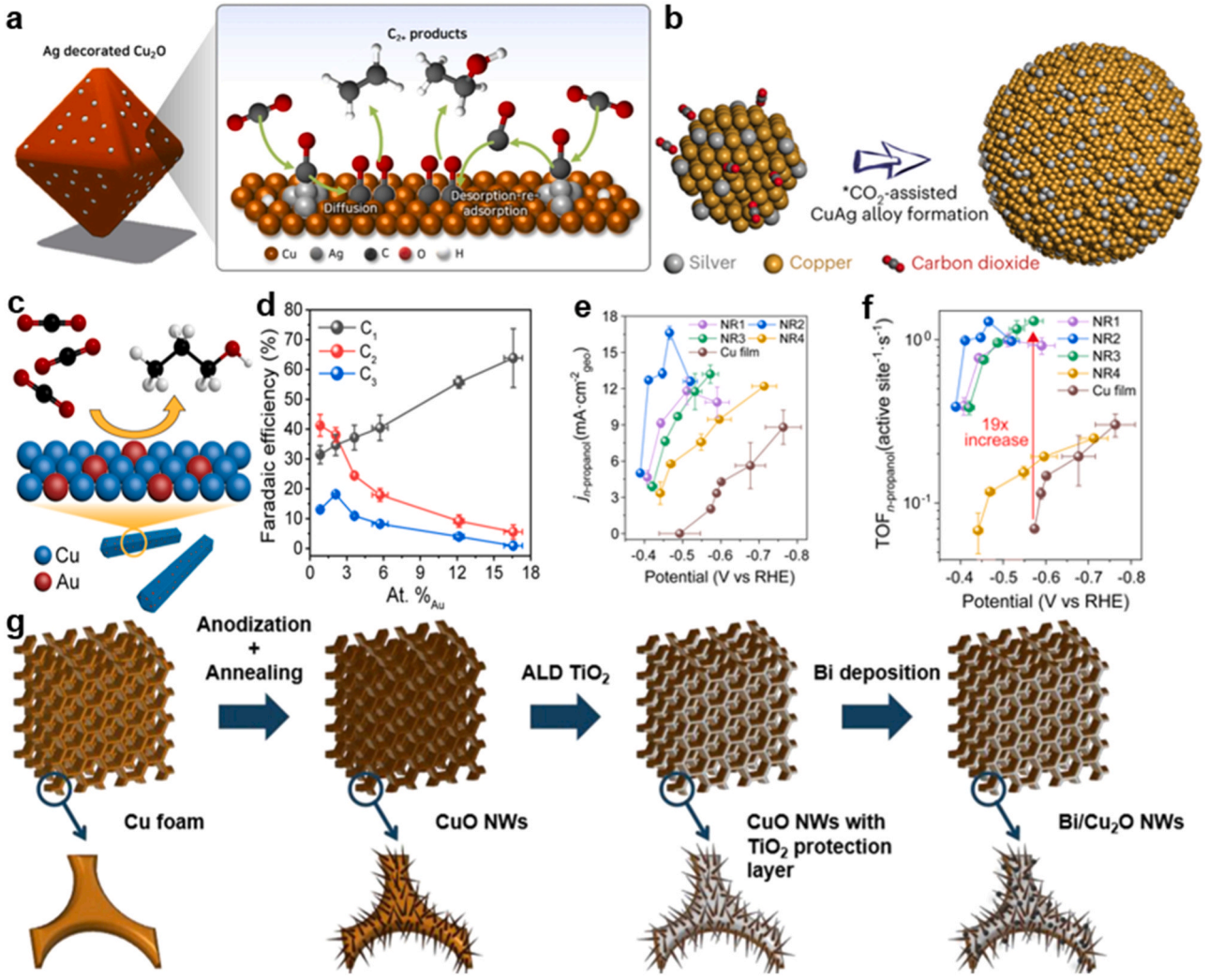

Fig. 12. **a** Schematic illustration of silver-modified Cu_2O forming tandem catalysts, which allows CO generated on the Ag surface to migrate from Ag to Cu at the Ag-Cu interface of Ag/Cu_2O by diffusion or sequential desorption-resorption, increasing the coverage of CO on the Cu surface [145]. Copyright 2023, Elsevier. **b** Schematic illustration of *CO_2 adsorption-assisted alloy formation [47]. Copyright 2023, Springer Nature. **c** Scheme of Au/Cu NR. **d-f** CO_2RR performance of Au/Cu NR catalysts. **d** FEs of C_1, C_2, and C_3 products. **e** Partial current densities of n-propanol production. **f** Potential-dependent $TOF_{n\text{-propanol}}$ values [148]. Copyright 2024, American Chemical Society. **g** Scheme of Bi/Cu_2O NWs synthesis [153]. Copyright 2022, Elsevier.

bimetallics via a galvanic-replacement approach. Co-doping of Ag and Ru in Cu induces *CO adsorption near C_1-C_1 and C_1-C_2 coupling sites, increasing CO coverage on the catalyst surface, and promoting multiple C-C couplings. Due to the high adsorption energy of the key *C_2 intermediate for C_1-C_2 coupling on Ag-Ru-Cu, the desorption of *C_2 intermediates from the Ag-Ru-Cu surface is reduced, thereby increasing the residence time of *C_2 intermediates needed for C_3 production, which dramatically improve the FE of C_{3+} products.

However, although the galvanic-replacement approach effectively introduces metals onto copper, it has limitations such as structural heterogeneity and poor crystal plane selectivity, making it challenging to achieve consistent control over the nanoparticle surface, thus affecting overall catalytic performance. Qi et al [47]. proposed a supersaturation strategy to synthesize CuAg alloy catalysts. By maintaining CO_2 concentration above the saturation limit and using a strong bicarbonate electrolyte to suppress the galvanic replacement reaction on the copper surface, they promoted the co-deposition of Ag and Cu to form a CuAg alloy (Fig. 12**b**), preferentially growing active CuAg (100) facets. This strategy promoted dendritic directional growth of the CuAg alloy, increasing the catalyst's ECSA, while dispersed Ag atoms weakened intermediate alkyl chain binding, enhanced C-O bond strength, and facilitated 2-propanol formation. The FE of 2-propanol was 56.7 % at a potential of −0.7 V vs. RHE, with a current density of 59.3 mA cm^{-2} over 200 hours. Ye et al [148]. synthesized a series of Au/Cu alloy nanorod (NR) catalysts with tunable surface compositions by adjusting the size of Au seeds (Fig. 12**c**), finding that the coverage of *C_1 and *C_2 intermediates during CO_2RR depended on the dispersion and concentration of surface Au dopants. The NR_2 ($2_{at\%}$ Au DMA) catalyst achieved a high $FE_{n\text{-propanol}}$ of 18.2 ± 0.3 % at a low overpotential of −0.41 V vs. RHE, with a partial current density for n-propanol of 16.6 mA cm^{-2}_{geo} (Fig. 12**d-f**). The high properties of these catalysis indicated that carefully controlling the concentration and distribution of minor metals is crucial for elucidating the structure-composition-property relationships and achieving excellent catalytic performance [148].

Moreover, the compressive strain induced by the lattice distortion in the alloy changes the position of the d-band center and modulates the interaction with the intermediates [149]. In CuZn alloys, the presence of Zn not only affects the electronic structure of the Cu sites but also desorbs poorly adsorbed CO on the Zn sites and increases the amount of stray CO on the Cu sites [150]. For instance, Roy et al [49]. synthesized the nano-alloy catalyst $Cu_{0.85}Zn_{0.15}$/C based on CuZn-BTC (1,3,5-benzene tricarboxylic acid) MOF. On the surface of the catalyst $Cu_{0.85}Zn_{0.15}$/C, the desorbed CO could diffuse and spill over to the Cu sites for the "CO insertion process" to form * -COCHO species, which is

favorable for acetone production, and $FE_{acetone}$ reached 38.1 % at −0.4 V vs. RHE. Kaya et al [48]. obtained a Cu-ZnO interface through a thermal oxidation method which still can produce acetone after 7 hours test. Interestingly, when applying potential at −1.7 V vs. RHE, significant formation of n-propanol and methanol was observed after one hour, with FEs of 23.36 % and 69.54 %, respectively. This might be due to the Cu_2O-ZnO (Cu^+ reduction to Cu) on the catalyst surface [151]. However, as the duration of electroreduction increased, the catalyst was reduced to Cu/ZnO, and the products gradually shifted to methanol, 2-propanol, and acetone. The FE for 2-propanol and acetone reached 33.65 % and 30.13 %, respectively. This shift may be caused by changes in the complex microenvironment during the electroreduction process, providing different C_1 and C_2 intermediates that couple at lower energy barriers, and the changes in the active sites of the metal structure during the reduction reaction. FESEM revealed that after 7 hours of CO_2RR, the Cu-ZnO interface exhibited that localized ZnO nanoflowers formed from $Zn(OH)_2$ precipitation. The formation of these nanoflowers involves electron and proton transfer, inducing a localized pH near the surface of the electrode, which facilitates the coupling of $*C_2$-$*C_1$ in favor of the formation of the C_3 product. Oxygen vacancies may be generated in the ZnO nanoflowers here, as reported by Geng et al. [152], the presence of oxygen vacancies increases the charge density of ZnO near the valence band, resulting in a highly stable adsorption configuration and stronger C═O bond activation, accelerating the CO insertion process and promoting acetone production. Azenha et al [153]. discovered that a series of Bi-loaded CuBi catalysts showed the presence of oxygen vacancies in Bi, enhancing CO_2 binding affinity and promoting propane formation (Fig. 12**g**). The FE for propane reached 85.4 % at a total current density of −45 mA/cm^2. However, the mechanism of propane formation on Cu-based materials requires further investigation.

3.4.2. *Two-step tandem catalytic system*

The direct electrochemical reduction of CO_2 to a single C_{3+} product faces challenges in selectivity and CO_2 conversion rates, particularly for large scale application, but these limitations in energy efficiency and current density can be addressed by designing multiple tandem devices to achieve the required industrial performance [70]. Romero Cuellar et al [154]. designed an integrated tandem cell system for CO_2RR, employing two-step electrolysis to produce multi-carbon products (Fig. 13**a**). Humidified CO_2 is supplied to the first electrochemical cell,

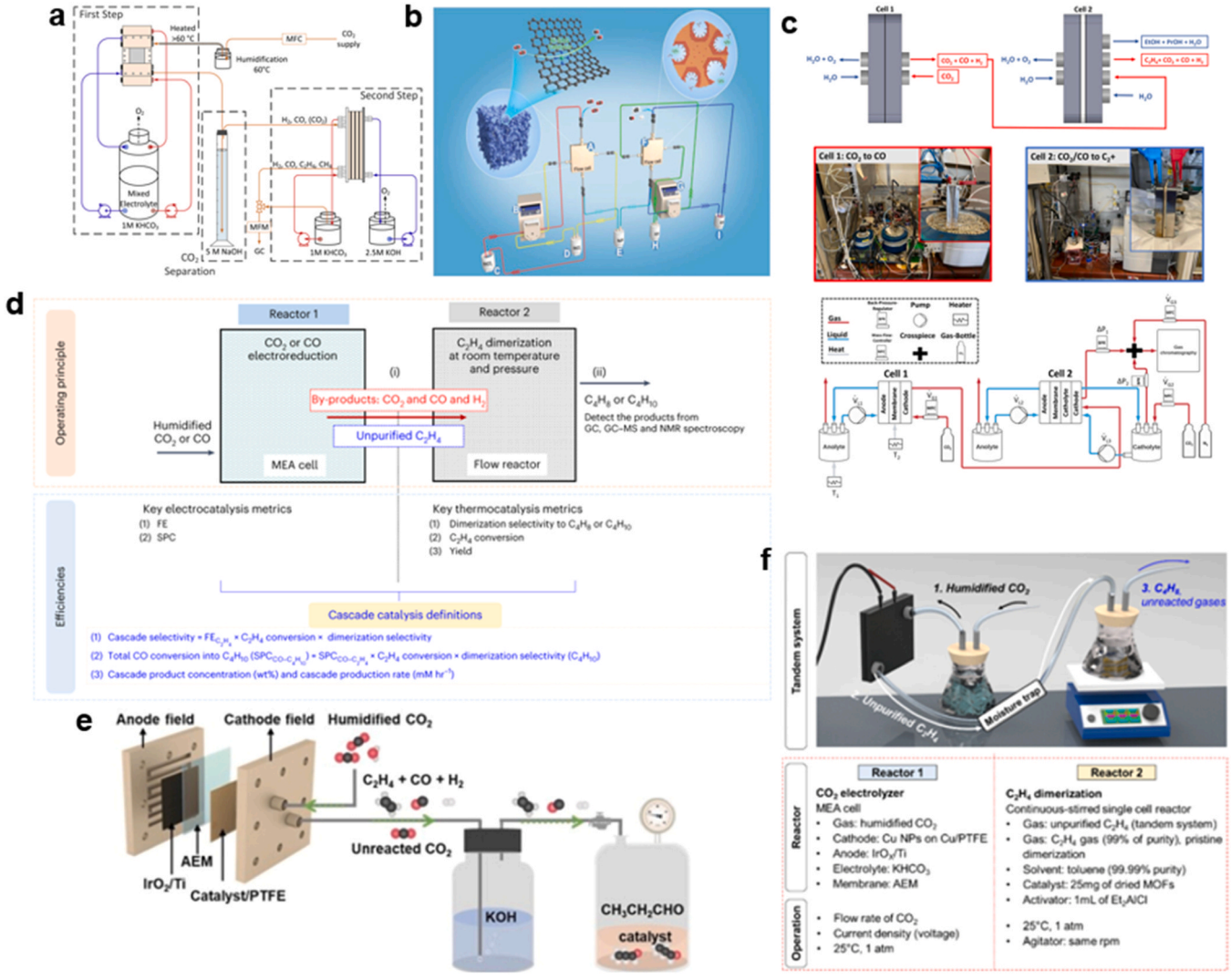

Fig. 13. **a** Schematic illustration of the tandem cell system for CO_2RR [154]. Copyright 2020, Elsevier. **b** Scheme of two-step tandem system CO_2 electrochemical reduction selective to n-propanol. Reproduce with permission[125] Copyright 2022, Welly. **c** Illustration of the tandem system with two low-temperature electrolytic cells [71]. Copyright 2023, Springer Nature. **d** Schematic EC-TC cascade concept and efficiency definitions [159]. Copyright 2023, Springer Nature. **e** Schematic illustration showing the coupling between the upstream MEA reactor and the downstream hydroformylation reactor. Reproduce with permission[161] Copyright 2024, Wiley. **f** Schematic illustration of the tandem system, reactor, and operation of MEA-based CO_2 electrolyzer and continuously stirred single-cell reactor [160]. Copyright 2024, American Chemical Society.

while the electrolyte is delivered from a reservoir containing 1 M $KHCO_3$ to both the cathode and the anode. The outlet of the first step is placed in an absorption column filled with 5 M NaOH, where unreacted CO_2 is separated from the produced CO and H_2. The gaseous products output from the absorption column are directed to a second electrolytic cell, operated with separated electrolytes at a flow rate of 100 ML min^{-1}. In the second step, CO is mainly converted to ethylene in the gas phase, and ethanol, acetate, and n-propanol in the liquid phase. The cumulative FE of multi-carbon products reached 62 % at a total current density of −300 mA/cm^2, which is 30 % higher than that of single-step electrolysis at the same current density. The main challenge in this process lies in the CO_2 losses between the first and second steps. High current densities result in high local alkalinity [155], as the formation of each carbon monoxide molecule produces two hydroxide ions. OH^- ions react with CO_2 to form carbonates. Under high alkalinity conditions, CO_3^{2-} becomes the dominant species, leading to the overall reaction: $2CO_2 + 2e^- \rightleftharpoons CO + CO_3^{2-}$. Thus, a total of 2 moles of CO_2 are required to produce 1 mol of CO. However, it is noteworthy that the CO_2-CO reaction in the first step occurs in a non-alkaline electrolyte, and the CO-C_{2+} reaction in the second step occurs in an alkaline environment, largely avoiding the issues of CO_2 loss and significant KOH consumption. Furthermore, the catalysts used in both cells of this system are common Ag and Cu nanoparticles, and there is room for improvement in overall catalytic performance and selectivity for C_{3+} products. Tang et al [125]. improved this tandem cell by developing a two-step tandem catalytic system more targeted at n-propanol production (Fig. 13**b**). In the first step, 3D Ni-SAG is used for CO_2 conversion to CO, achieving stable CO production with a Faradaic efficiency of 95.9 % at a current density of 140 mA cm^{-2}. Similar to Romero Cuellar et al.'s design [154], they placed a purifier containing 5 M NaOH solution between the two flow cells to remove unreacted CO_2. In the second step, a Cu^+/Cu system is used, selecting hollow Cu_2O nanoparticles as the catalyst for CO conversion to n-propanol. The partial current density for n-propanol reached 11.9 mA cm^{-2}, and the FE for n-propanol was 15.9 %, with a corresponding half-cell power conversion efficiency of 19.3 %. Strasser et al. [71], considering CO_2 losses in the electrochemical process, designed, assembled, and analyzed the first tandem electrolytic cell system for efficient electrochemical CO_2 reduction to C_{2+} products (such as ethylene, ethanol, and n-propanol) under fully low-temperature, neutral pH conditions (Fig. 13**c**). This tandem system design consists of two low-temperature electrolytic cells in series, allowing for the conversion of CO_2 to a mixed CO_2/CO stream in electrolytic cell 1, followed by the catalytic conversion of the mixed CO_2/CO stream to C_{2+} products in electrolytic cell 2. This tandem cell system, designed from an energy requirements perspective, further accelerates the industrial implementation of electrochemical CO_2 conversion to C_3 products.

Electrochemically reducing CO_2 to a mixture of ethylene, CO, and H_2, followed by thermocatalytic hydroformylation (EC-TC), is also an effective method for obtaining C_{3+} products through a tandem system. Currently, significant improvements have been made in the Faradaic efficiency and selectivity of electrochemical CO_2 reduction to ethylene [156,157]. The EC-TC method produces C_2H_4, CO, and H_2 in the first step, which further used as feedstocks for the second step of thermocatalytic hydroformylation, favoring the production of a single desired species [158]. Sargent et al. [159], combined electrochemical and thermochemical reactors, proposed a cascade C_1-C_2-C_4 system capable of selectively producing C_4H_{10} under mild environmental conditions (Fig. 13**d**). They upgraded the exhaust stream from the CO_2 or CO electrolytic cell using Ni-NiO-SiO_2 as the catalyst in the C_2H_4 dimerization reactor without purification, achieving an overall two-stage CO-to-C_4H_{10} cascade selectivity of 43 %. Furthermore, they applied $Ru_2(OAc)_4Ni(CN)_4$ MOF with dual metal catalytic sites as in the second step thermocatalytic reaction, selectively producing 1-C_4H_8. When the entire system operated at a constant current density of 156 mA cm^{-2}, the tandem system maintained a production rate of 1-C_4H_8 at 1.3 mol g_{cat}^{-1} h^{-1} over 10 hours (Fig. 13**f**) [160]. Li et al. [161], using $Cu(OH)_2$ nanowires as a precatalyst, electrochemically converted CO_2/H_2O to C_2H_4, CO, and H_2 in a zero-gap membrane electrode assembly (MEA) reactor (Fig. 13**e**). Followed by feeding the produced gases into a hydroformylation reactor to further convert to propionaldehyde under mild temperatures and near-atmospheric pressure conditions using an optimized Rh-DPPB catalyst. By coupling the upstream CO_2 electroreduction and downstream hydroformylation reactions, the selectivity for propionaldehyde reached ~38 %, with a total C_3 oxygenate selectivity of 44 %. These values represent an improvement of over 7 times compared to the best standalone electrochemical systems and more than 2 times compared to other mixed systems.

3.4.3. Performance comparison between Cu-based tandem system and single Cu system

To further demonstrate the advantages of tandem catalysts over single Cu-based systems, we present a comparative summary in Table 1, which compiles data on the Faradaic efficiency (FE) of C_{3+} product formation from both single Cu catalysts and Cu-based tandem catalysts. The data reveal a clear performance gap: most single Cu catalysts exhibit C_3 product FEs below 10 %, while tandem catalysts typically reach FEs above 30 %, with the highest reported values exceeding 85.4 %. These improvements are attributed to enhanced *CO coverage, improved intermediate retention, and more favorable environments for C-C coupling in tandem architectures.

In addition, we summarize several representative two-step Cu-based tandem systems in Table 2, including both electrochemical–electrochemical and electrochemical–thermochemical configurations. These systems not only improve product selectivity and carbon chain length but also significantly enhance reactant utilization. For instance, the tandem setups in Table 2 achieve up to 7-fold increases in overall selectivity or conversion efficiency compared to the best standalone systems. They also enable process segmentation: the first stage can operate in neutral media to minimize CO_2 loss, while the second stage uses alkaline conditions to optimize C-C coupling. This design flexibility is crucial for overcoming the trade-offs inherent in single-cell systems.

These comparisons strongly indicate that both material-level tandem catalysts and system-level tandem configurations are highly effective in boosting C_{3+} product selectivity and efficiency, providing a compelling strategy for advancing scalable CO_2 electro-reduction technologies.

4. Non-Cu-based materials for CO_2RR to C_{3+} products

Due to the effective binding with CO* , Cu-based catalysts are widely used for C_{2^+} products. However, the lack of selectivity control over C_1, C_2, and C_{3+} products results in the production of multiple by-products, which reduces the energy conversion efficiency for the single C_{3+} product. In addition to Cu and Cu-based materials, transition-metal phosphides, chalcogenides, and free-metal catalysts have demonstrated exceptional performance in selectively producing C_{3+} products during CO_2RR.

4.1. Ni-based materials for CO_2RR to C_{3+} products

Since Bocarsly et al [162]. first reported that Ni_3Al thin films on glassy carbon can produce C_3 products from CO_2, non-copper, nickel--based heterogeneous electrocatalysts have attracted significant attention for CO_2 reduction to C_{3+} products. Unlike Cu-based catalysts, which generate *CO intermediates on the catalyst surface and proceed with C-C coupling reactions, Ni-based catalysts (typically Ni_xP) rely on HCOO* as the key intermediate and follow a completely different pathway to achieve C-C coupling and the formation of multi-carbon products [163]. On Ni-based catalysts, HCOO* undergoes further transformation into H_2CO* via proton-coupled electron transfer (PCET). Subsequently, H_2CO* undergoes self-condensation (C-C coupling) to form multi-carbon intermediates, such as methyl glyoxal and 2,3-furandiol

Table 1
Summary of performance of Cu-based catalysts for CO_2RR to C_{3+} products.

Catalyst type	Catalyst	Cell type	Electrolyte	C_{3+} product	C_{3+} current density (mA cm^{-2})	Potential (V vs. RHE)	FE %	Refs.
CuOD-Cu/ Chemical Oxidation	F -Cu	Flow cell	0.75 M KOH	1-propanol	32	−0.60	6.4	44
	CuOD-Cu	H-cell	0.1 M $KHCO_3$	1-propanol	4.5	−0.94	~17.9	46
	CuOD-Cu	Flow cell	0.1 M $KHCO_3$	1-propanol	8.51	−1.14	6.96	46
	Cu_2O HNC	Flow cell	3.0 M KOH	1-propanol	58.41	−1.68	8.21	59
	Cu_2O-derived Cu	H-cell	0.1 M $KHCO_3$	1-propanol	1.7	−0.83	4.3	60
	CuO-derived Cu	Flow cell	1.0 M KOH	1-butanol	0.08	−0.48	0.056	67
				1-propanol	18.5	−0.58	6.5	
	b-Cu_2O/Cu	Flow cell	1.0 M KOH	1-propanol	101.6	−1.10	12.1	79
	b-Cu_2O/Cu	H-cell	0.1 M $KHCO_3$	1-propanol	6.8	−1.40	16.2	79
	CuS_x-DSV	Flow cell	1.0 M KOH	1-propanol	9.9	−0.85	3.8	80
	CuS_x-DSV	H-cell	0.1 M $KHCO_3$	1-propanol	3.1	−1.05	15.4	80
	Cu-CuI	Flow cell	1.0 M KOH	1-propanol	62.1	−1.00	~6.9	85
	K-F-Cu-CO_2	Flow cell	1.0 M KOH	1-propanol	~31.2	−0.53	~4.7	86
	Cu-BDD	H-cell	0.5 M KCl	acetone	/	−0.39	7.0	87
	Cu-B	H-cell	0.1 M $KHCO_3$	1-propanol	0.58	−1.15	7.1	88
	Cu-P	H-cell	0.1 M $KHCO_3$	1-propanol	0.41	−1.15	5.1	88
CuOD-Cu/thermal annealing	Activated Cu mesh	H-cell	0.5 M $KHCO_3$	1-propanol	1.3	−0.90	13.1	61
				propylene	/		< 2	
	Electrodeposited Cu foam	H-cell	0.5 M $KHCO_3$	1-propanol	1.72	−0.87	8.21	94
CuOD-Cu/oxygen plasma exposure & halogen anion treatment	Plasma-Activated Cu nanocube	H-cell	0.1 M $KHCO_3$	1-propanol	0.11	−1.00	~7.2	63
	Cu_2O_{Cl}	H-cell	0.1 M KCl	1-propanol	/	−1.60	8.7	65
				propylene			0.9	
				propane			1	
				1-butane			0.9	
	Cu-KF	Flow cell	0.1 M $KHCO_3$	1-propanol	/	−1.00	3.1	66
	$Ar_{10\ min}$-Plasma Cu	Flow cell	0.1 M $CsHCO_3$	1-propanol	~0.2	−1.00	~6.0	105
	ON-CuO	H-cell	0.1 M $KHCO_3$	1-propanol	/	−1.10	5.9	95
	Pulsed-Cu(100)	H-cell	0.1 M $KHCO_3$	1-propanol	/	−1.00	5.5	107
	Cu_KCl	H-cell	0.1 M KCl	1-propanol	/	−1.40	8.6	112
	Cu_KBr	H-cell	0.1 M KBr	1-propanol	/	−1.50	6.3	112
	Cu_KI	H-cell	0.1 M KI	1-propanol	/	−1.40	8.8	112
	R-Cu-c	H-cell	0.1 M $KHCO_3$	1-propanol	8.1	−1.05	17.2	114
Cu NPs	34 %N-C/Cu	Flow cell	1 M KOH	1-propanol	/	−0.68	~7.7	84
	5 nm Cu NP	H-cell	0.1 M $KHCO_3$	Mainly 1-propanol	/	−0.80	~5.68	118
	Agglomerated Cu NPs	H-cell	0.1 M $KHCO_3$	1-propanol	1.7	−0.95	8.8	119
	Cu NPs	H-cell	0.1 M $KHCO_3$	1-propanol	0.8	−0.81	5.9	121
	Cu NPs	Flow cell	1 M $KHCO_3$	1-propanol	/	−0.97	4.6	124
	CuCl-derived Cu nanocubes	Flow cell	1 M KOH+ 0.2 M CsI	propylene	273.7	−0.60	1.5	39
Cu SACs & Cu molecular	Cu-SA/NPC	Flow cell	0.1 M $KHCO_3$	acetone	/	−0.36	36.7	51
	Cu/Ag_2S/Ag	Flow cell	0.1 M $KHCO_3$	1-propanol	/	−1.40	~4.0	133
	Hex−2Cu-O	H-cell	0.1 M $KHCO_3$	1-propanol	1.9	−1.10	18.2	75
	CuBtz	H-cell	0.1 M $KHCO_3$	1-propanol	/	−1.30	4	139
	CuBr−4PP	H-cell	0.5 M $KHCO_3$	1-propanol	/	−1.59	~10	140
Cu-Based Tandem Catalyst	CO_2−10-$Cu_{94}Ag_6$[a)]	High-pressure electrolyzer	1.0 M $CsHCO_3$	2-propanol	59.3	−0.70	56.7	47
	CO_2−10-$Cu_{94}Ag_6$	H-cell	1.0 M $CsHCO_3$	2-propanol	12.0	−0.73	39.6	47
	Cu-ZnO 7hrs	H-cell	0.1 M $KHCO_3$	2-propanol	/	−1.09	33.65	48
				acetone			30.13	
	Cu-ZnO 1 hr	H-cell	0.1 M $KHCO_3$	1-propanol	/	−1.09	23.36	48
	Cu-TO 3hrs	H-cell	0.1 M $KHCO_3$	1-propanol	/	−1.09	5.05	48
	$Cu_{0.95}Zn_{0.05}$/C	H-cell	0.1 M $NaHCO_3$	acetone	/	−0.40	12.3	49
	$Cu_{0.93}Zn_{0.07}$/C	H-cell	0.1 M $NaHCO_3$	acetone	/	−0.40	19.0	49
	$Cu_{0.85}Zn_{0.15}$/C	H-cell	0.1 M $NaHCO_3$	acetone	/	−0.40	38.1	49
	10 Ag/Cu_2O	H-cell	0.5 M $KHCO_3$	1-propanol	1.7	−0.82	9.09	145
	Ag_1Sb_{30}/Cu	H-cell	0.1 M $KHCO_3$	mainly 1-propanol	/	−1.19	~11.0	146
	Au/Cu NR (NR2)	Flow cell	1 M KOH	1-propanol	12.5	−0.41	18.2	148
	Bi/Cu_2O #50 C	Flow cell	0.1 M $KHCO_3$	propane	38.4	−1.19	85.4	153
	Bi/Cu_2O #5 C	Flow cell	0.1 M $KHCO_3$	propane	29.1	−1.19	64.6	153

[a)] Under the pressure of 10 bar

[164].

Han et al [165]. further extended the scope of nickel-based catalysis by exploring molecular nickel thiolate complexes for CO_2 reduction. They reported a series of nickel thiolate complexes that exhibited unprecedented electrocatalytic activity in reducing CO_2 to C_3 products in aqueous $KHCO_3$ electrolyte. Among these, $Ni(mp)_2^-$ (mp = 2-mercaptophenolate) showed remarkable activity, achieving FE 8.2 % for C_3 products at −1.0 V vs. RHE. Notably, the addition of CO significantly enhanced the total $FE_{C1\text{-}C3}$ products to 41.1 %, suggesting that a key Ni-CO intermediate is involved in the catalytic process. Spectroscopic

Table 2
Summary of Two-Step Tandem Catalytic System for CO_2RR to C_{3+} Products.

System Type	Catalysts	Main Products	Current density	Main Product Selectivity (FE)	Performance Improvement vs. Single System	Ref.
EC–EC Tandem	Step 1: Ag; Step 2: Cu nanoparticles	Acetate, n-propanol	Total: −300 mA/cm^2	FE(C_{2+} products) = 62 %	Approx. 30 % higher than single-step	154
EC–EC Tandem	Step 1: 3D Ni-SAG; Step 2: Hollow Cu_2O nanoparticles	n-propanol	Step 1: 140 mA/cm^2	FE(n-propanol)= 15.9 %	Half-cell PCE = 19.3 %	125
EC–EC Tandem	Step 1:Ni-N-C; Step 2: commercial Cu nanoparticles	n-propanol	Low-temperature, neutral pH	Single pass carbon efficiency: 30–35 %	2 times better than single system	71
EC–TC Tandem	Step 1: Cu nanoparticles; Step 2: Ni–NiO–SiO_2 for C_2H_4 dimerization	C_4H_{10}	100 mA/cm^2	Product yield: 94 %, selectivity: 43 %; single-pass conversion: 16.5 %	No gas purification needed; high selectivity	159
EC–TC Tandem	Step 1: Cu nanoparticles; Step 2: $Ru_2(OAc)_4Ni(CN)_4$ MOF	1-butene (1-C_4H_8)	Total: 156 mA/cm^2	Production rate= 1.3 mol/g/cat/h	Stable for 10 hours	160
EC–TC Tandem	Step 1: $Cu(OH)_2$ nanowires; Step 2: Rh-DPPB catalyst	Propionaldehyde	Zero-gap MEA reactor	Selectivity: ~38 % (propionaldehyde), ~44 % (C_3 oxygenates)	7 times better than best standalone EC; 2 times better than other mixed systems	161

studies confirmed that the nickel thiolate complexes remained intact during CO_2 reduction, providing further evidence of their stability and reusability. Dismukes et al [164]. synthesized five nickel phosphides (Ni_xP) and found that the selectivity and activity of these catalysts for C_{3+} products in CO_2RR significantly improve with increasing phosphorus content. NiP_2 achieved a remarkable 71 % FE for 2,3-furandiol at an overpotential of only 10 mV while completely suppressing the HER. Furthermore, on the potential of −0.1 V vs. RHE, NiP_2 also exhibited 84 % selectivity for methylglyoxal. This exceptional catalytic performance is attributed to the unique mechanism of nickel phosphides, which stabilize oxygen-bound intermediates such as HCOO* and H_2CO* , facilitating aldehyde self-condensation and efficient C−C coupling. Furthermore, Yeo et al [52]. enhanced the understanding of CO_2RR to C_{3+} products by synthesized $Ni_3(PO_4)_2$-derived $Ni^{\delta+}$ catalyst, which exhibited the ability to produce C_3 to C_6 hydrocarbons under ambient conditions, achieving a total FE for carbonaceous products of approximately 30 %, with a notable 6.5 % FE for C_3 to C_6 hydrocarbons at −1.2 V vs. RHE. This advancement is attributed to the presence of polarized $Ni^{\delta+}$ sites stabilized by Ni-O bonds, which drive a Fischer-Tropsch-like pathway, enabling efficient C-C bond formation and subsequent hydrocarbon chain growth. These pathways bypass the CO intermediate commonly observed on copper-based catalysts, relying instead on hydride transfer, oxophilic binding and polarization to achieve high selectivity and energy efficiency under mild conditions. Complementing these experimental studies, Rappe et al [163]. through DFT calculations provided theoretical insights into the formation of multi-carbon products. They highlighted that the strong hydrogen affinity of the Ni_2P surface and surface reconstruction triggered by hydrogen adsorption play crucial roles. This hydrogen affinity provides a sufficient hydrogen source for the reduction and hydrogenation of intermediates (e.g., HCOO* and H_2CO*), while surface reconstruction creates favorable thermodynamic conditions for C−C coupling reactions.

These combined findings underline the unique advantages of nickel-based catalysts in CO_2RR and provide a foundation for further studies. To validate and refine these hypotheses, future research involving advanced techniques such as in situ Raman spectroscopy and in situ electron microscopy is essential.

4.2. Mo-based materials for CO_2RR to C_{3+} products

Mo-based heterogeneous electrocatalysts have garnered considerable attention for the eCO_2RR to C_{3+} products due to their unique electronic structures, natural abundance, and strong ability to stabilize critical reaction intermediates [166,167]. Recent findings [168] indicate that rather than traditionally assumed edge sites, defect sites (such as S-vacancies in MoS_2 and P-vacancies in Mo_3P) located on the catalyst terraces may serve as crucial active centers. At these vacancies, the reaction pathway diverges from conventional *CO intermediates and can proceed via *OCHO and subsequent C_1 intermediates (e.g., *HCHO), which undergo condensation reactions to yield multi-carbon species. Notably, Francis et al [169]. demonstrated that single-crystal MoS_2 terraces can achieve FE of 2–5 % for producing 1-propanol at moderate overpotentials (-0.59 V vs. RHE), however, this process may be accompanied by partial de-sulfidation of MoS_2. Building upon these advances, Asadi et al [53]. further expanded the potential of Mo-based catalysts by combining imidazolium-functionalized Mo_3P (ImF-Mo_3P) nanoparticles with an anion-exchange ionomer in alkaline electrolytes to mitigate the issue of de-sulfidation. Under relatively mild overpotentials (-0.2 to −1.0 V vs. RHE), this system consistently produced hydrocarbons, achieving an impressive 91 % FE for propane at −0.8 V vs. RHE, with a partial current density j_{C3H8} of −361 mA/cm^2. Electron energy loss spectroscopy (EELS) and in situ Raman spectroscopy revealed that the anion-exchange ionomer forms a coating layer on the ImF-Mo_3P surface, regulating surface charge distribution and the local environment through ion exchange with the electrolyte. This regulation enhances CO_2 adsorption and activation via hydrogen bonding and localized electric fields, lowering CO_2 adsorption energies, stabilizing CO intermediates, and ultimately promoting C-C-C trimerization. As a result, the catalyst preferentially forms C_3 products instead of simpler C_1 or C_2 products.

Moreover, strategies such as surface reconstruction, doping, and ligand engineering can further mitigate the competing HER, thereby directing Mo-based catalysts toward the selective formation of C_3 and higher-carbon products. These combined experimental and theoretical advances highlight the remarkable potential of Mo-based catalysts to achieve the reduction of CO_2 to C_{3+} products. In the future, integrating advanced in situ characterization techniques with machine learning approaches may help validate and refine these hypotheses, providing deeper insights into active sites, intermediates, and reaction mechanisms. Such understanding will guide the rational design of Mo-based electrocatalysts capable of efficiently converting CO_2 into C_{3+} products.

4.3. Performance comparison and complementarity with Cu-based catalysts

While Cu-based catalysts are known for their unique ability to catalyze *CO–CO and *CO-C_2 coupling to generate C_{2+} and C_{3+} products, their limited selectivity and susceptibility to competing side reactions (e.g., HER and CH_4 formation) remain challenges. In contrast, recent progress in non-Cu-based catalysts, such as Ni- and Mo-based systems, has demonstrated promising selectivity for C_{3+} products through alternative pathways involving *HCOO and *H_2CO

intermediates.

To better illustrate the advantages and limitations of both categories, we summarize their performance in Table 3. Non-Cu-based catalysts show high variability in C_{3+} product FE, ranging from as low as 2 % to as high as 91 %, depending on the catalyst structure and reaction pathway. In contrast, Cu-based catalysts typically achieve C_{3+} FEs between 5 % and 40 %. Notably, the highest C_{3+} FE of 91 % was achieved by a non-Cu-based catalyst (ImF-Mo_3P) operating at a high current density of -361 mA/cm^2, whereas the best-performing Cu-based tandem catalyst reached 85.4 % FE at a much lower current density of -38.4 mA/cm^2. This indicates that certain non-Cu catalysts not only exhibit competitive selectivity but also maintain high activity under industrially relevant conditions. Furthermore, non-Cu catalysts demonstrate superior electrochemical stability in alkaline environments, which are often necessary to suppress competing reactions and enhance reaction kinetics. These advantages-high FE at high current densities, low cost, and better durability-suggest that non-Cu-based systems may hold greater promise for practical and scalable CO_2-to-C_{3+} conversion in future industrial applications.

Mechanistically, Ni-based catalysts such as NiP_2 and $Ni_3(PO_4)_2$ stabilize oxygen-bound intermediates (e.g., *HCOO, *H_2CO) and enable aldehyde condensation to form C_3 oxygenates. Similarly, Mo-based systems like Mo_3P and MoS_2 defect sites promote *HCHO trimerization or *CO-CH-CO formation via C_1 intermediates. These pathways bypass traditional *CO dimerization and offer a complementary mechanism to that of Cu. Despite some researchers have discovered some mechanism for non-Cu catalysts, a unified mechanistic understanding of C_{3+} product formation on non-Cu catalysts is still lacking, especially for C_3-C_6 hydrocarbons. Continued efforts using in situ characterization (e.g., operando Raman, XAS) and DFT-guided screening are essential to uncover the true nature of active sites and rate-determining steps.

Overall, Cu- and non-Cu-based systems offer complementary pathways toward C_{3+} products, and their combination in tandem or hybrid configurations may yield synergetic improvements in both selectivity and energy efficiency.

5. Machine learning for CO_2RR to C_{3+} products

Compared with C_1 or C_2 products, generating C_{3+} products from CO_2 are substantially more complex in electrocatalysis. Forming long-chain hydrocarbons and oxygenates typically requires overcoming higher energy barriers, navigating more intricate reaction pathways, and meticulously tuning active sites to enable the critical C-C coupling steps [38]. Traditional approaches-whether theoretical methods like DFT or experimental (high-throughput screening)-often fall short of fully exploring and optimizing these highly complex processes due to the trade-off between limited computational resources and the vast number of potential catalysts [170]. Consequently, the integration of artificial intelligence (AI), machine learning (ML), and high-throughput algorithms has emerged as a transformative strategy, accelerating the discovery of efficient and highly selective catalysts toward a new paradigm in CO_2 conversion research.

AI-driven approaches, particularly those involving ML, present compelling solutions due to their exceptional learning and predictive capabilities, allowing for rapid screening of vast catalyst libraries with significantly lower experimental and computational costs. Through combining ML with the DFT approach, significant progress has been made to accelerate DFT calculations, effectively reducing computational loads and making subsequent experimental designs more targeted [171]. For instance, Yan et al [172]. have combined DFT data with ML regression models to estimate formation energies with reduced computational expense, facilitating rapid screening of bimetallic electrocatalysts. Neural networks have further advanced the analysis of complex processes, such as reaction kinetics and the exploration of disordered structures in intermetallic compounds while trivial methods still rely heavily on expert intuition for unleashing novel catalysts. Many current approaches focus exclusively on DFT-based surface-layer properties (e.g., d-band centers) without differentiating between distinct types of surface sites, as shown in (Fig. 14). On the contrary, the neural network with an ML approach, can not only generate vast space of catalytic surface structures but also automate the screening of potential sites, selectivity, and catalytic descriptors with pre-trained data at reduced computational cost.

In the training set and learning approach, ML can generally be classified into supervised and unsupervised paradigms. Supervised learning leverages large-scale, structured datasets to train neural networks that map feature vectors to known ground-truth labels. In contrast, unsupervised learning identifies hidden patterns in unlabeled and unordered datasets. Given that CO_2RR research often relies on labeled datasets where catalytic descriptors, e.g., adsorption energies, the binding energy of reaction intermediates, and reaction selectivity, are derived from DFT calculations of known datasets, resulting in quite an accurate predictive model, making supervised learning the dominant approach in the field [174]. By pre-providing ample paired input-output data, researchers can train models using advanced frameworks such as graph neural networks (GNNs), transformers, multi-task mixture density models, or diffusion models to capture highly nonlinear and complex reaction dynamics [175]. Once trained, these models demonstrate exceptional predictive accuracy for new inputs, as validated by numerous benchmark evaluations, as demonstrated in (Fig. 15).

This combined DFT-ML approach supported by data-driven analyses, holds tremendous potential for systematically screening and determining catalytic surface configurations, predicting CO_2RR selectivity and products, optimizing and lowering reaction energy barriers, and ultimately unlocking novel catalyst designs for CO_2RR. For example, Sargent and colleagues[176] innovatively combined ML and DFT within a high-throughput screening framework to accelerate the discovery of electrocatalysts for CO_2RR. They screened 244 copper-containing intermetallic compounds from the Materials Project database, encompassing 12229 surfaces and 228969 adsorption sites. A subset of CO adsorption energy (ΔE_{CO}) data derived from DFT calculations was used to train an ML model, enabling efficient predictions across all sites. By

Table 3
Performance summary of Non-Cu-Based Catalysts for C_{3+} Products.

Catalyst	Main Product	Faradaic Efficiency (FE)	Potential	Partial current density (mA/cm^2)	Ref.
Ni_3Al thin film	C_3 products	N/A	−0.1 V vs. RHE	N/A	158
$Ni(mp)_2^-$ (molecular nickel thiolate)	C_3 products (C_3H_6+C_3H_8)	8.2 %	−1.0 V vs. RHE	N/A	161
NiP_2	2,3-furandiol	71 %	0 V vs. RHE	N/A	160
	Methylglyoxal	84 %	−0.1 V vs. RHE	N/A	
$Ni_3(PO_4)_2$-derived Niδ$^+$	C_3-C_6 hydrocarbons	6.5 % (C_3-C_6), ~30 % (total carbonaceous products)	−1.2 V vs. RHE	−0.91	48
MoS_2 (single crystal terrace)	1-propanol	2–5 %	−0.59 V vs. RHE		165
ImF-Mo_3P with ionomer	C_3H_8	91 %	−0.8 V vs. RHE	−361	49

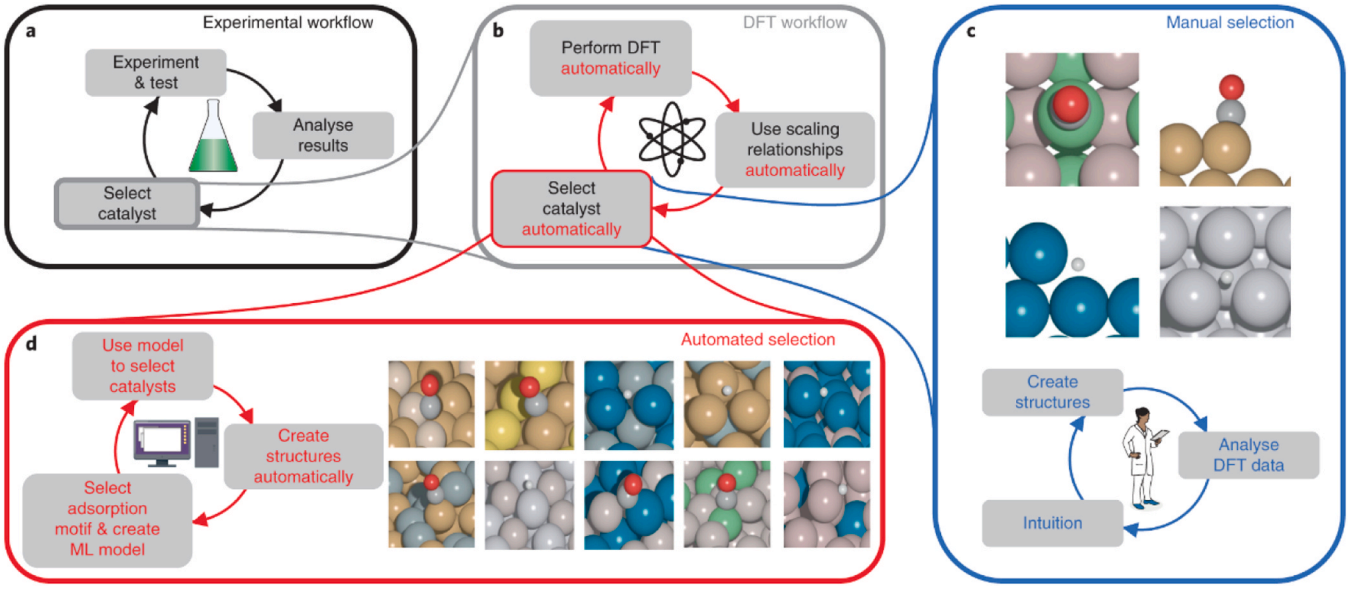

Fig. 14. Comparison of traditional catalyst discovery workflows and the machine-learning-enhanced framework. **a** and **b** how the experimental workflow for discovering catalysts can be accelerated using a DFT-based screening process. **c** the conventional workflow (in blue), which relies on scientific intuition to manually select candidates for DFT screening. **d** a new workflow (in red) that employs ML to systematically and automatically select suitable candidates [173]. Copyright 2018, Springer Nature.

correlating these predictions with volcano plots, researchers identified an optimal catalytic ΔE_{CO} of approximately −0.67 eV (Fig. 16). This iterative workflow-where ML predictions highlights promising candidates, followed by DFT validation and retraining-reduced the required DFT simulations to about 4000 times, significantly improving computational efficiency compared to the traditional high-throughput approach. Among the identified candidates, Cu-Al alloys stood out, exhibiting near-optimal ΔE_{CO} values across multiple sites. Their reduced CO overbinding further decreased the energy barrier for C-C coupling, a critical step in generating C_{2+} products. Experimental validation refined the synthesis strategies for Cu-Al alloys, achieving a C_{2+} product selectivity of 85–90 % at a current density of 600 mA cm^{-2}.

Similarly, Qiao et al [177]. integrated DFT calculations, AI-driven clustering, and experimental validation to elucidate how the oxidation state of copper (OSCu) influences the selectivity for C_{2+} products in CuO_x catalysts. They found that a moderate oxidation state (OSCu ≈ +0.5) significantly promotes the conversion of *CO to *CHO while reducing the energy barrier for C-C coupling, thereby enhancing the yield of C_{2+} products. Notably, their AI clustering analysis systematically examined 30 transition-metal-doped CuO_x samples, revealing an inverted volcano relationship between the doping metals' properties (e.g., electronegativity, ionic potential) and C_{2+} selectivity. This clustering approach efficiently classified dopants while clarifying their regulatory effects on OSCu. Metals such as Ta, W, and Nb were highlighted for stabilizing OSCu ≈ +0.5 and enhancing C_{2+} generation. Furthermore, by integrating AI clustering with Pourbaix diagrams, (Fig. 17) they proposed a co-doping strategy combining early transition metals (e.g., W, Nb, Ta) to enhance C-C coupling and late transition metals (e.g., Ag, Pd, Zn) to promote CO generation. This comprehensive design framework simplifies the complexity of catalyst design for intricate reactions, paving the way for future applications in metal oxides, MXenes, and nanostructured catalysts.

Huang et al [54]. integrate a first-principles machine learning (FPML) approach with graphdiyne (GDY)-based atomic catalysts (ACs) to achieve high-accuracy predictions of the C-C-C coupling processes and distinct C_3 product pathways in CO_2RR, which as depicted in (Fig. 18). By relying solely on datasets derived from C_1 and C_2 pathways in DFT simulations, they effectively eliminate the need for additional and often time-consuming DFT calculations for C_3 routes. Despite reducing computational burden, they still capture the mechanistic details and energy barriers of multiple C_3 products, including acetone, 1, 2-propylene glycol, and propanol. A central focus lies in elucidating how the neighboring effect and the 'small-large integrated cycle' mechanism drive C-C-C coupling. They described how sequential hydrogenation, and coupling can transition from simpler C_1 routes (small cycles) to more extensive C_3 cycles (large cycles), shedding light on the competitive landscape between C_1 and C_3 pathways: although direct coupling of C_1 intermediates is energetically favorable, forming C_3 products ultimately demands multi-step hydrogenation. In addition, they underscore that alkyl-chain active sites on GDY generally outperform metal-centered sites in promoting multi-carbon extension, thus delivering higher electrochemical activity. Among the screened catalysts, GDY-Cu, GDY-Mn, GDY-Sc, GDY-Pd, GDY-Pr, and GDY-Pm show notable advantages for 1-propanol formation, while GDY-Pr and GDY-Pm also excel at producing 1,2-propylene glycol and acetone. Beyond unraveling the complexities of the C_3 reaction mechanisms, the study reveals how different active sites in GDY-ACs facilitate carbon-chain growth from C_1/C_2 intermediates and how modulating site selection, metal choice, and multi-step cycles can critically affect the selectivity toward C_{3+} products. Consequently, this research not only clarifies the mechanistic underpinnings of C_3 pathways but also offers crucial guidance for designing high-performance GDY-based catalysts that selectively synthesize multi-carbon products in CO_2RR.

6. Conclusion & outlook

This review summarizes the latest advancements regarding the role of electrocatalysts in the reduction of CO_2 to C_{3+} products. The present strategies for designing copper-based catalysts primarily rely on the following approaches: 1. Creation of defect sites and grain boundaries: tandem reactions are achieved by increasing the number of active sites through the introduction of defect sites or different grain boundaries on the catalyst surface. This design can improve the overall activity and selectivity of the catalyst and facilitate multi-step reactions. 2. Surface engineering modulation: Increase the number of low-coordinated copper sites on the surface and adjust the ratio of Cu^+/Cu(0) by modulating the structure of the copper-based catalyst surface, prolonging the residence time of the reaction intermediates in the active sites, promoting

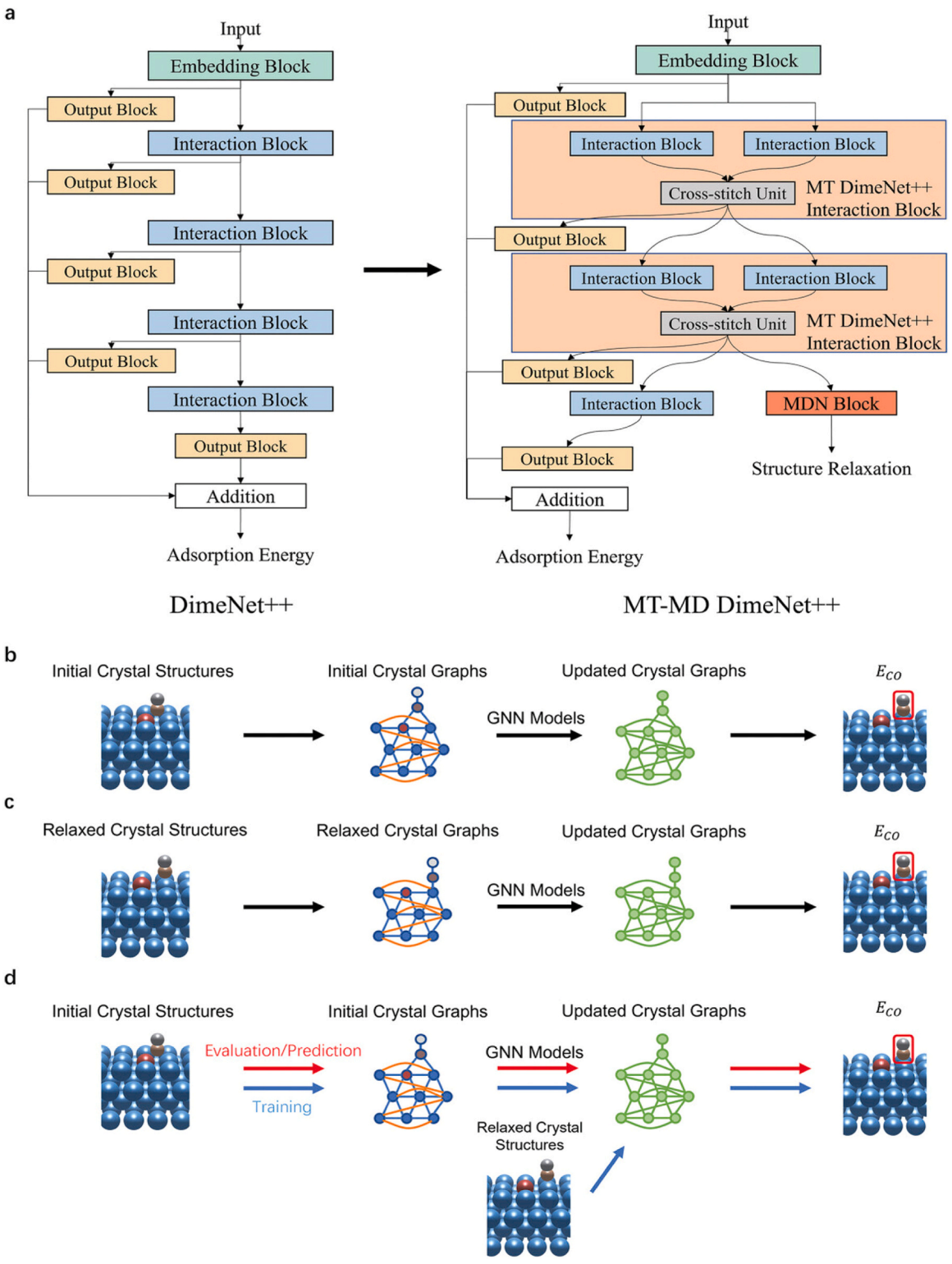

Fig. 15. The architecture of the multi-task mixture density model DimeNet+ + and its associated prediction task workflows. **a** The structures of DimeNet+ + (left) and its multi-task variant (right) are shown, where the description within the Input Block has been reorganized to clarify the illustration-specifically, the Output Block has been removed. **b** and **c** The workflow for predicting E_{CO} is demonstrated, where crystal structures (either initial or relaxed) are encoded into crystal graphs based on the specified cut-off radius and maximum number of neighbors. In these graphs, the silver, brown, red, and blue nodes represent O, C, dopant, and substrate atoms, respectively, while orange edges are added to account for periodic boundary conditions on the surface. **d** The multi-task workflow (MT) proposed in this work utilizes graph neural networks (GNNs) for prediction tasks. The blue and yellow arrows represent the training and inference processes, respectively [175]. Copyright 2024, Wiley.

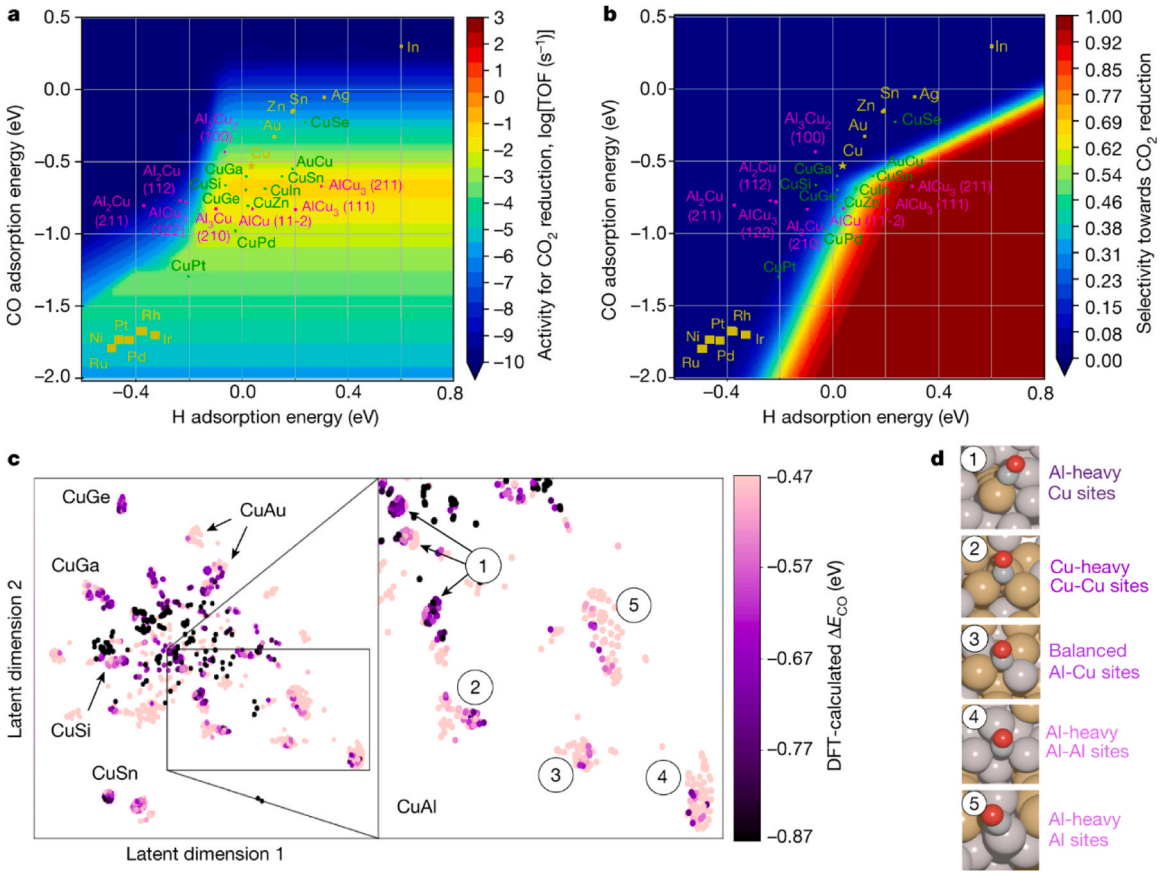

Fig. 16. The activity and selectivity volcano plots for CO_2 reduction and the DFT-calculated adsorption properties of Cu-containing alloy surfaces. **a** and **b** two-dimensional volcano plots for activity and selectivity, respectively, with CO and H adsorption energies calculated using DFT. Yellow points represent average adsorption energies for monometallic, green points for copper alloys, and magenta points for low-coverage Cu-Al surfaces. **c** approximately 4000 adsorption sites from Cu-containing alloys, with Cu-Al clusters labeled numerically. **d** coordination environments for each cluster, categorized as "Al-heavy," "Cu-heavy," or "balanced," based on the stoichiometric composition of the surface and the adsorption site [176]. Copyright 2020, Springer Nature.

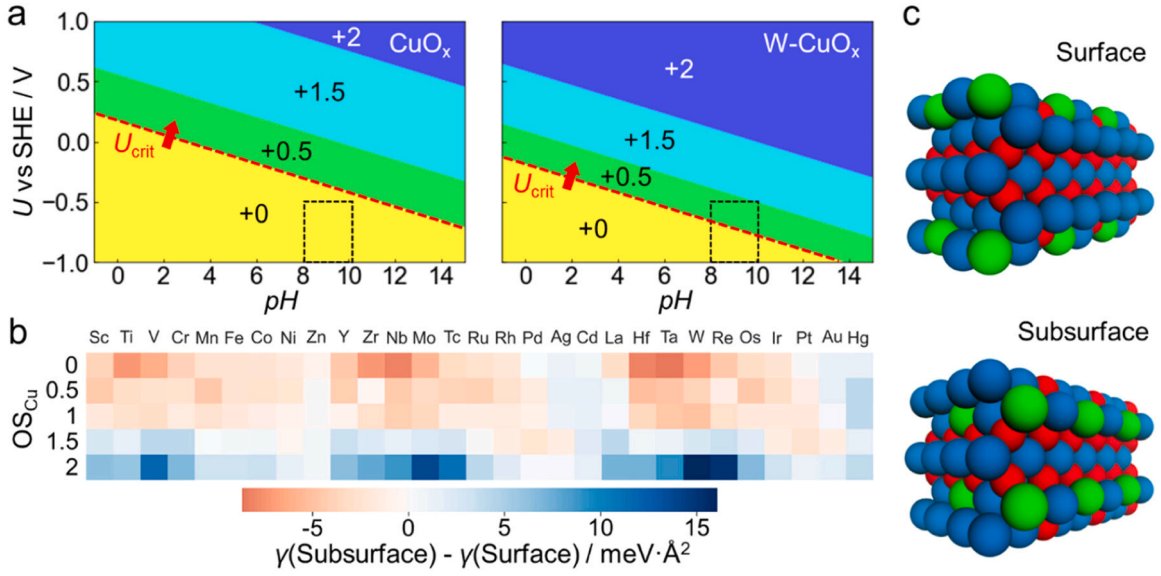

Fig. 17. The effect of doping the t-CuO(001) surface with different transition metal heteroatoms on its stable region and oxidized state (OSCu) in the Pourbaix plot (U/pH). **a** Surface Pourbaix (U/pH) diagram of pristine t-CuO(001) (CuO_x) and with W heteroatoms (W-CuO_x). The red dashed lines mark the critical potential (Ucrit) from OSCu = +0 to + 0.5, while the black dashed boxes highlight practical reaction conditions (U = −0.5 to −1.0 V vs SHE, pH = 8–10). **b** Surface free energy (γ) differences at U = 0 V vs RHE when various transition-metal atoms are doped at either the surface or the subsurface. Red regions indicate that subsurface doping is more stable, whereas blue regions indicate that surface doping is more stable. **c** Side views of the atomic structures for surface and subsurface doping, with copper (Cu) in blue, oxygen (O) in red, and transition-metal heteroatoms in green [177]. Copyright 2023, American Chemical Society.

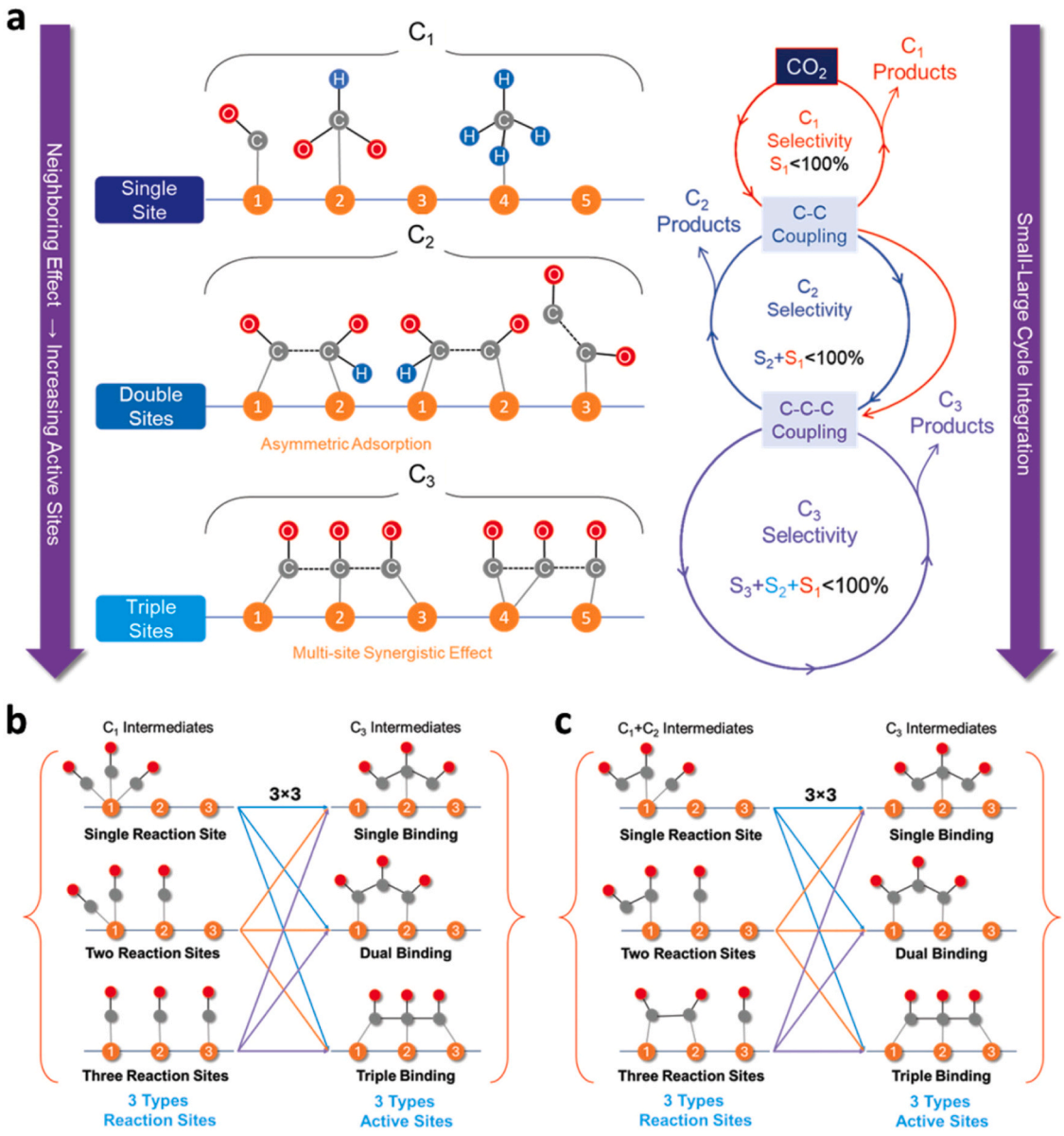

Fig. 18. **a** The motivation for introducing ML in this work. **b** only C_1 intermediates participate in C-C-C coupling with various configurations of reaction and active sites and **c** $C_1 + C_2$ intermediates [54]. Copyright 2024, Welly.

the coupling reaction of $*C_1$ and $*C_2$. 3. Optimized tandem cell design to minimize the energy consumption and CO_2 loss during the step of C_1-C_2-C_{3+}, improving the efficiency of the generation of high-value multi-carbon products.

To further enhance the efficiency of CO_2 reduction to C_{3+} product, future research should focus on the deep integration of ML and AI, conbined with HTP and advanced computational modeling, to drive the development of automated and intelligent catalyst design. The following aspects deserve our efforts in the future:

First, HTP computation for catalyst pre-screening is of significant necessity [178]. With the aid of the enhanced supercomputing power, the catalyst libraries are expected to be upbuilt for one specific application. With broadening the candidate scope for the target application assisted by the HTP computation, it will enable the faster and more reliable pre-screening of the catalysts. Meanwhile, ML-assisted computational screening methods, such as GNNs, deep learning, and Transformer models, can improve screening accuracy and reduce computational costs, making catalyst selection faster and more reliable [179]. Additionally, the application of DFT-ML hybrid frameworks allows for more efficient predictions of adsorption energies, charge distribution, and intermediate binding abilities, thereby accelerating the discovery of promising catalysts [180].

Second, the Operando/in-situ characterization techniques need to be further advanced and developed with ML technology [181]. In CO_2 to C_{3+} conversion, there exist many reaction steps before the end products formed, while traditional experimental methods often struggle to directly observe these processes. However, ML-driven operando characterization analysts can precisely analyze catalyst surface evolution, intermediate stability, and the rate-determining steps (RDS), which will optimize cayalysts' stability and activity [182,183]. Furthermore, these RDS directly influence reaction pathways and ultimately determine C_{3+} products' selectivity. Meanwhile, ML-enhanced operando/in-situ characterization enables real-time monitoring of key reaction intermediates and catalyst surface dynamics, providing a more comprehensive assessment of catalyst activity, stability, and selectivity in the formation of C_{3+} products [183]. This integrated approach offers a powerful solution for understanding catalyst effectiveness in CO_2 reduction and optimizing reaction conditions for improved efficiency.

Third, advanced computational studies considering the reaction environments (applied potential, electrolytes, other local strain/field perturbations) are very helpful in more accurately understanding the reaction mechanism [184,185]. In the electrochemical CO_2 reduction process, various strategies can be employed to modulate the reaction environment, including adjusting the applied potential on catalyst surfaces, optimizing electrolyte properties, tuning internal and interfacial strain within catalysts, and introducing localized electric or magnetic fields [186,187]. However, traditional computational models often assume idealized reaction conditions, neglecting the complex interactions occurring at real electrochemical interfaces, which makes their predictions less consistent with experimental observations. ML-driven multi-scale modeling can address this limitation by integrating electrode-electrolyte interactions, electric field perturbations, and solvent effects, leading to a more accurate optimization of catalyst stability and adaptability under realistic electrochemical conditions [188]. By incorporating these factors into catalyst optimization, ML-guided strategies hold great promise for discovering high-performance CO_2 reduction catalysts with enhanced activity and selectivity.

Last but not least, with the rapid development of HTP experimentation for materials synthesis and the growing application of ML techniques in materials science [189,190], there is a growing opportunity to combine first-hand experimental data with ML tools to elucidate the relationships between synthesis parameters and material properties. For instance, by leveraging active learning (AL) algorithms, ML models can be continuously refined using real-time experimental data, thereby increasing the efficiency of experimental design and dynamically optimizing catalyst composition, morphology, and reaction conditions [191]. Such data-driven insights can greatly accelerate the design and preparation of catalytic materials, especially those incorporating multiple functionalities required for CO_2 reduction to C_{3+} products. Consequently, harnessing the aforementioned strategies holds significant promise for advancing the next generation of CO_2 reduction catalysts, making them more effective at producing high-value multi-carbon products.

Declaration of Competing Interest

The authors declare the following financial interests/personal relationships which may be considered as potential competing interests: Prof. Zongyou Yin reports financial support was provided by Australian Research Council. Prof. Zongyou Yin reports a relationship with Australian Research Council that includes: funding grants. If there are other authors, they declare that they have no known competing financial interests or personal relationships that could have appeared to influence the work reported in this paper.

Acknowledgments

The authors acknowledge the financial support from the Australian Research Council (FT230100059, DP240100687, IH220100012, and LP210100436).

References

[1] J.-P. Gattuso, A. Magnan, R. Billé, W.W.L. Cheung, E.L. Howes, F. Joos, D. Allemand, L. Bopp, S.R. Cooley, C.M. Eakin, O. Hoegh-Guldberg, R.P. Kelly, H.-O. Pörtner, A.D. Rogers, J.M. Baxter, D. Laffoley, D. Osborn, A. Rankovic, J. Rochette, U.R. Sumaila, S. Treyer, C. Turley, Contrasting futures for ocean and society from different anthropogenic C_2 emissions scenarios, Science 349 (6243) (2015) aac4722.

[2] W. Song, X.-Y. Liu, C.-C. Hu, G.-Y. Chen, X.-J. Liu, W.W. Walters, G. Michalski, C.-Q. Liu, Important contributions of non-fossil fuel nitrogen oxides emissions, Nat. Commun. 12 (1) (2021) 243.

[3] Z. Liu, Z. Deng, S.J. Davis, C. Giron, P. Ciais, Monitoring global carbon emissions in 2021, Nat. Rev. Earth Environ. 3 (4) (2022) 217–219.

[4] Z. Liu, Z. Deng, S. Davis, P. Ciais, Monitoring global carbon emissions in 2022, Nat. Rev. Earth Environ. 4 (4) (2023) 205–206.

[5] D. Cheng, Z.-J. Zhao, G. Zhang, P. Yang, L. Li, H. Gao, S. Liu, X. Chang, S. Chen, T. Wang, G.A. Ozin, Z. Liu, J. Gong, The nature of active sites for carbon dioxide electroreduction over oxide-derived copper catalysts, Nat. Commun. 12 (1) (2021) 395.

[6] X. Duan, J. Xu, Z. Wei, J. Ma, S. Guo, S. Wang, H. Liu, S. Dou, Metal-Free Carbon Materials for CO_2 Electrochemical Reduction, Adv. Mater. 29 (41) (2017) 1701784.

[7] Y. Yamazaki, H. Takeda, O. Ishitani, Photocatalytic reduction of CO_2 using metal complexes, J. Photochem. Photobiol. C: Photochem. Rev. 25 (2015) 106–137.

[8] R. Muñoz, L. Meier, I. Diaz, D. Jeison, A review on the state-of-the-art of physical/chemical and biological technologies for biogas upgrading, Rev. Environ. Sci. Bio/Technol. 14 (4) (2015) 727–759.

[9] J. Wu, S. Ma, J. Sun, J.I. Gold, C. Tiwary, B. Kim, L. Zhu, N. Chopra, I.N. Odeh, R. Vajtai, A.Z. Yu, R. Luo, J. Lou, G. Ding, P.J.A. Kenis, P.M. Ajayan, A metal-free electrocatalyst for carbon dioxide reduction to multi-carbon hydrocarbons and oxygenates, Nat. Commun. 7 (1) (2016) 13869.

[10] X. Li, Y. Sun, J. Xu, Y. Shao, J. Wu, X. Xu, Y. Pan, H. Ju, J. Zhu, Y. Xie, Selective visible-light-driven photocatalytic CO_2 reduction to CH_4 mediated by atomically thin $CuIn_5S_8$ layers, Nat. Energy 4 (8) (2019) 690–699.

[11] A.R. Woldu, Z. Huang, P. Zhao, L. Hu, D. Astruc, Electrochemical CO_2 reduction (CO_2RR) to multi-carbon products over copper-based catalysts, Coord. Chem. Rev. 454 (2022) 214340.

[12] S. Jin, Z. Hao, K. Zhang, Z. Yan, J. Chen, Advances and Challenges for the Electrochemical Reduction of CO_2 to CO: From Fundamentals to Industrialization, Angew. Chem. 133 (38) (2021) 20795–20816.

[13] L. Fan, C. Xia, P. Zhu, Y. Lu, H. Wang, Electrochemical CO_2 reduction to high-concentration pure formic acid solutions in an all-solid-state reactor, Nat. Commun. 11 (1) (2020) 3633.

[14] T. Zheng, C. Liu, C. Guo, M. Zhang, X. Li, Q. Jiang, W. Xue, H. Li, A. Li, C.-W. Pao, J. Xiao, C. Xia, J. Zeng, Copper-catalysed exclusive CO_2 to pure formic acid conversion via single-atom alloying, Nat. Nanotechnol. 16 (12) (2021) 1386–1393.

[15] H. Wu, L. Huang, J. Timoshenko, K. Qi, W. Wang, J. Liu, Y. Zhang, S. Yang, E. Petit, V. Flaud, J. Li, C. Salameh, P. Miele, L. Lajaunie, B. Roldán Cuenya, D. Rao, D. Voiry, Selective and energy-efficient electrosynthesis of ethylene from CO_2 by tuning the valence of Cu catalysts through aryl diazonium functionalization, Nat. Energy 9 (4) (2024) 422–433.

[16] W. Fang, R. Lu, F.-M. Li, C. He, D. Wu, K. Yue, Y. Mao, W. Guo, B. You, F. Song, T. Yao, Z. Wang, B.Y. Xia, Low-coordination Nanocrystalline Copper-based Catalysts through Theory-guided Electrochemical Restructuring for Selective CO_2 Reduction to Ethylene, Angew. Chem. Int. Ed. 63 (16) (2024) e202319936.

[17] X. Zhong, H.-J. Peng, C. Xia, X. Liu, Recent advances in upgrading CO_2 to C_{3+} products via electrochemical and complementary engineering, J. Mater. Chem. A (2024).

[18] K. Xiang, F. Shen, Y. Fu, L. Wu, Z. Wang, H. Yi, X. Liu, P. Wang, M. Liu, Z. Lin, Boosting CO_2 electroreduction towards C_{2+} products via CO* intermediate manipulation on copper-based catalysts, Environ. Sci.: Nano 9 (3) (2022) 911–953.

[19] G. Liang, S. Yang, C. Wu, Y. Liu, Y. Zhao, L. Huang, S. Zhang, S. Dou, H. Du, D. Cui, L. Lin, Advancing C–C coupling of the electrocatalytic CO_2 reduction reaction for C_{2+} products, J. Mater. Chem. A (2025).

[20] Y. Guan, Y. Li, Z. Li, Y. Hou, L. Lei, B. Yang, Promotion of C—C Coupling in the CO_2 Electrochemical Reduction to Valuable C_{2+} Products: From Micro-Foundation to Macro-Application, Adv. Mater. (2025) 2417567.

[21] Y. Luo, S. Hu, B. Liu, Steering electroreduction of carbon dioxide to valuable C_{3+} products, Sci. China Mater. 67 (6) (2024) 1780–1790.

[22] S.R. Nicholson, N.A. Rorrer, T. Uekert, G. Avery, A.C. Carpenter, G.T. Beckham, Manufacturing Energy and Greenhouse Gas Emissions Associated with United States Consumption of Organic Petrochemicals, ACS Sustain. Chem. Eng. 11 (6) (2023) 2198–2208.

[23] Y. Qian, J. Guo, Y. Zhang, W. Tao, X. Lu, Combustion and emission behavior of N-propanol as partially alternative fuel in a direct injection spark ignition engine, Appl. Therm. Eng. 144 (2018) 126–136.

[24] Y.-Y. Liu, H.-L. Zhu, Z.-H. Zhao, N.-Y. Huang, P.-Q. Liao, X.-M. Chen, Insight into the Effect of the d-Orbital Energy of Copper Ions in Metal–Organic Frameworks on the Selectivity of Electroreduction of CO_2 to CH_4, ACS Catal. 12 (5) (2022) 2749–2755.

[25] L. Guo, J. Zhou, F. Liu, X. Meng, Y. Ma, F. Hao, Y. Xiong, Z. Fan, Electronic Structure Design of Transition Metal-Based Catalysts for Electrochemical Carbon Dioxide Reduction, ACS Nano 18 (14) (2024) 9823–9851.

[26] Y. Qin, W. Zhao, C. Xia, L.J. Yu, F. Song, J. Zhang, T. Wu, R. Cao, S. Ding, B. Y. Xia, Y. Su, CO Intermediate-Assisted Dynamic Cu Sintering During Electrocatalytic CO_2 Reduction on Cu−N−C Catalysts, Angew. Chem. 136 (23) (2024).

[27] Mao, Y.; Zhang, M.; Zhai, G.; Si, S.; Liu, D.; Song, K.; Liu, Y.; Wang, Z.; Zheng, Z.; Wang, P.; Dai, Y.; Cheng, H.; Huang, B., Asymmetric Cu(I)—W Dual-Atomic Sites Enable C—C Coupling for Selective Photocatalytic CO2 Reduction to C2H4. *Advanced Science* 2024 (11/28), 2401933.

[28] J.D. Goodpaster, A.T. Bell, M. Head-Gordon, Identification of Possible Pathways for C–C Bond Formation during Electrochemical Reduction of CO_2: New Theoretical Insights from an Improved Electrochemical Model, J. Phys. Chem. Lett. 7 (8) (2016) 1471–1477.

[29] S. Chakraborty, R. Das, M. Riyaz, K. Das, A.K. Singh, D. Bagchi, C.P. Vinod, S. C. Peter, Wurtzite $CuGaS_2$ with an In-Situ-Formed CuO Layer Photocatalyzes CO_2 Conversion to Ethylene with High Selectivity, Angew. Chem. Int. Ed. 62 (9) (2023) e202216613.

[30] X.Y. Zhang, Z.X. Lou, J. Chen, Y. Liu, X. Wu, J.Y. Zhao, H.Y. Yuan, M. Zhu, S. Dai, H.F. Wang, C. Sun, P.F. Liu, H.G. Yang, Direct OC-CHO coupling towards highly C_{2+} products selective electroreduction over stable Cu^0/Cu^{2+} interface, Nat. Commun. 14 (1) (2023) 7681.

[31] K. Yao, J. Li, H. Wang, R. Lu, X. Yang, M. Luo, N. Wang, Z. Wang, C. Liu, T. Jing, S. Chen, E. Cortés, S.A. Maier, S. Zhang, T. Li, Y. Yu, Y. Liu, X. Kang, H. Liang, Mechanistic Insights into OC–COH Coupling in CO_2 Electroreduction on Fragmented Copper, J. Am. Chem. Soc. 144 (31) (2022) 14005–14011.

[32] X. Nie, M.R. Esopi, M.J. Janik, A. Asthagiri, Selectivity of CO_2 Reduction on Copper Electrodes: The Role of the Kinetics of Elementary Steps, Angew. Chem. Int. Ed. 52 (9) (2013) 2459–2462.

[33] Z. Wang, Y. Li, J. Boes, Y. Wang, E. Sargent, CO_2 Electrocatalyst Design Using Graph Theory, Research Square Platform LLC, 2020.

[34] L. Chen, C. Tang, Y. Zheng, E. Skúlason, Y. Jiao, C_3 production from CO_2 reduction by concerted *CO trimerization on a single-atom alloy catalyst, J. Mater. Chem. A 10 (11) (2022) 5998–6006.

[35] Y.-T. Chan, I.S. Huang, M.-K. Tsai, Enhancing C–C bond formation by surface strain: a computational investigation for C_2 and C_3 intermediate formation on strained Cu surfaces, Phys. Chem. Chem. Phys. 21 (41) (2019) 22704–22710.

[36] X. Chang, A. Malkani, X. Yang, B. Xu, Mechanistic Insights into Electroreductive C–C Coupling between CO and Acetaldehyde into Multicarbon Products, J. Am. Chem. Soc. 142 (6) (2020) 2975–2983.

[37] S. Pablo-García, F.L.P. Veenstra, L.R.L. Ting, R. García-Muelas, F. Dattila, A. J. Martín, B.S. Yeo, J. Pérez-Ramírez, N. López, Mechanistic routes toward C_3 products in copper-catalysed CO2 electroreduction, Catal. Sci. Technol. 12 (2) (2022) 409–417.

[38] Y. Zheng, A. Vasileff, X. Zhou, Y. Jiao, M. Jaroniec, S.-Z. Qiao, Understanding the Roadmap for Electrochemical Reduction of CO_2 to Multi-Carbon Oxygenates and Hydrocarbons on Copper-Based Catalysts, J. Am. Chem. Soc. 141 (19) (2019) 7646–7659.

[39] J. Gao, A. Bahmanpour, O. Kröcher, S.M. Zakeeruddin, D. Ren, M. Grätzel, Electrochemical synthesis of propylene from carbon dioxide on copper nanocrystals, Nat. Chem. 15 (5) (2023) 705–713.

[40] Y. Pang, J. Li, Z. Wang, C.-S. Tan, P.-L. Hsieh, T.-T. Zhuang, Z.-Q. Liang, C. Zou, X. Wang, P. De Luna, J.P. Edwards, Y. Xu, F. Li, C.-T. Dinh, M. Zhong, Y. Lou, D. Wu, L.-J. Chen, E.H. Sargent, D. Sinton, Efficient electrocatalytic conversion of carbon monoxide to propanol using fragmented copper, Nat. Catal. 2 (3) (2019) 251–258.

[41] X. Wang, P. Ou, A. Ozden, S.-F. Hung, J. Tam, C.M. Gabardo, J.Y. Howe, J. Sisler, K. Bertens, F.P. García de Arquer, R.K. Miao, C.P. O'Brien, Z. Wang, J. Abed, A. S. Rasouli, M. Sun, A.H. Ip, D. Sinton, E.H. Sargent, Efficient electrosynthesis of n-propanol from carbon monoxide using a Ag–Ru–Cu catalyst, Nat. Energy 7 (2) (2022) 170–176.

[42] T.-T. Zhuang, Y. Pang, Z.-Q. Liang, Z. Wang, Y. Li, C.-S. Tan, J. Li, C.T. Dinh, P. De Luna, P.-L. Hsieh, T. Burdyny, H.-H. Li, M. Liu, Y. Wang, F. Li, A. Proppe, A. Johnston, D.-H. Nam, Z.-Y. Wu, Y.-R. Zheng, A.H. Ip, H. Tan, L.-J. Chen, S.-H. Yu, S.O. Kelley, D. Sinton, E.H. Sargent, Copper nanocavities confine intermediates for efficient electrosynthesis of C_3 alcohol fuels from carbon monoxide, Nat. Catal. 1 (12) (2018) 946–951.

[43] R. Zhang, J. Zhang, S. Wang, Z. Tan, Y. Yang, Y. Song, M. Li, Y. Zhao, H. Wang, B. Han, R. Duan, Synthesis of n-Propanol from CO_2 Electroreduction on Bicontinuous Cu_2O/Cu Nanodomains, Angew. Chem. Int. Ed. (2024).

[44] W. Ma, S. Xie, T. Liu, Q. Fan, J. Ye, F. Sun, Z. Jiang, Q. Zhang, J. Cheng, Y. Wang, Electrocatalytic reduction of CO_2 to ethylene and ethanol through hydrogen-assisted C–C coupling over fluorine-modified copper, Nat. Catal. 3 (6) (2020) 478–487.

[45] J. Li, F. Che, Y. Pang, C. Zou, J.Y. Howe, T. Burdyny, J.P. Edwards, Y. Wang, F. Li, Z. Wang, P. De Luna, C.-T. Dinh, T.-T. Zhuang, M.I. Saidaminov, S. Cheng, T. Wu, Y.Z. Finfrock, L. Ma, S.-H. Hsieh, Y.-S. Liu, G.A. Botton, W.-F. Pong, X. Du, J. Guo, T.-K. Sham, E.H. Sargent, D. Sinton, Copper adparticle enabled selective electrosynthesis of n-propanol, Nat. Commun. 9 (1) (2018) 4614.

[46] C. Long, X. Liu, K. Wan, Y. Jiang, P. An, C. Yang, G. Wu, W. Wang, J. Guo, L. Li, K. Pang, Q. Li, C. Cui, S. Liu, T. Tan, Z. Tang, Regulating reconstruction of oxide-derived Cu for electrochemical CO_2 reduction toward n-propanol, Sci. Adv. 9 (43) (2023) eadi6119.

[47] K. Qi, Y. Zhang, N. Onofrio, E. Petit, X. Cui, J. Ma, J. Fan, H. Wu, W. Wang, J. Li, J. Liu, Y. Zhang, Y. Wang, G. Jia, J. Wu, L. Lajaunie, C. Salameh, D. Voiry, Unlocking direct CO2 electrolysis to C_3 products via electrolyte supersaturation, Nat. Catal. 6 (4) (2023) 319–331.

[48] S. Munir, A.R. Varzeghani, S. Kaya, Electrocatalytic reduction of CO_2 to produce higher alcohols, Sustain. Energy Fuels 2 (11) (2018) 2532–2541.

[49] S. Payra, S. Kanungo, S. Roy, Controlling C–C coupling in electrocatalytic reduction of CO_2 over $Cu_{1-x}Zn_x$/C, Nanoscale 14 (36) (2022) 13352–13361.

[50] M.-G. Kim, Y. Choi, E. Park, C.-H. Cheon, N.-K. Kim, B.K. Min, W. Kim, Crystalline/Amorphous Ni_2P/Ho_2O_3 Core/Shell Nanoparticles for Electrochemical Reduction of CO_2 to Acetone, ACS Appl. Energy Mater. 3 (12) (2020) 11516–11522.

[51] K. Zhao, X. Nie, H. Wang, S. Chen, X. Quan, H. Yu, W. Choi, G. Zhang, B. Kim, J. G. Chen, Selective electroreduction of CO_2 to acetone by single copper atoms anchored on N-doped porous carbon, Nat. Commun. 11 (1) (2020) 2455.

[52] Y. Zhou, A.J. Martín, F. Dattila, S. Xi, N. López, J. Pérez-Ramírez, B.S. Yeo, Long-chain hydrocarbons by CO_2 electroreduction using polarized nickel catalysts, Nat. Catal. 5 (6) (2022) 545–554.

[53] M. Esmaeilirad, Z. Jiang, A.M. Harzandi, A. Kondori, M. Tamadoni Saray, C. U. Segre, R. Shahbazian-Yassar, A.M. Rappe, M. Asadi, Imidazolium-functionalized Mo_3P nanoparticles with an ionomer coating for electrocatalytic reduction of CO_2 to propane, Nat. Energy 8 (8) (2023) 891–900.

[54] M. Sun, B. Huang, Direct Machine Learning Predictions of C_3 Pathways, Adv. Energy Mater. 14 (13) (2024) 2400152.

[55] H. Jiao, C. Wang, H. Tian, Z.-Y. Zhang, Y. Zhao, P. Na, Y. Yamauchi, Z.-L. Wang, Strong interaction heterointerface of NiFe oxyhydroxide/cerium oxide for efficient and stable water oxidation, Chem. Eng. J. 498 (2024) 155063.

[56] D. Ren, J. Gao, L. Pan, Z. Wang, J. Luo, S.M. Zakeeruddin, A. Hagfeldt, M. Grätzel, Atomic Layer Deposition of ZnO on CuO Enables Selective and Efficient Electroreduction of Carbon Dioxide to Liquid Fuels, Angew. Chem. Int. Ed. 58 (42) (2019) 15036–15040.

[57] S.J. Raaijman, N. Arulmozhi, M.T.M. Koper, Morphological Stability of Copper Surfaces under Reducing Conditions, ACS Appl. Mater. Interfaces 13 (41) (2021) 48730–48744.

[58] Z.-Z. Wu, F.-Y. Gao, M.-R. Gao, Regulating the oxidation state of nanomaterials for electrocatalytic CO_2 reduction, Energy amp; Environ. Sci. 14 (3) (2021) 1121–1139.

[59] H. Zhang, Y. Qiao, Y. Wang, Y. Zheng, H. Huang, In situ oxidative etching-enabled synthesis of hollow Cu_2O nanocrystals for efficient CO_2RR into C_{2+} products. *Sustainable Energy &amp*, Fuels 6 (21) (2022) 4860–4865.

[60] A.D. Handoko, C.W. Ong, Y. Huang, Z.G. Lee, L. Lin, G.B. Panetti, B.S. Yeo, Mechanistic Insights into the Selective Electroreduction of Carbon Dioxide to Ethylene on Cu_2O-Derived Copper Catalysts, J. Phys. Chem. C. 120 (36) (2016) 20058–20067.

[61] M. Rahaman, A. Dutta, A. Zanetti, P. Broekmann, Electrochemical Reduction of CO_2 into Multicarbon Alcohols on Activated Cu Mesh Catalysts: An Identical Location (IL) Study, ACS Catal. 7 (11) (2017) 7946–7956.

[62] M. Rahaman, K. Kiran, I.Z. Montiel, V. Grozovski, A. Dutta, P. Broekmann, Selective n-propanol formation from CO_2 over degradation-resistant activated PdCu alloy foam electrocatalysts, Green. Chem. 22 (19) (2020) 6497–6509.

[63] D. Gao, I. Zegkinoglou, N.J. Divins, F. Scholten, I. Sinev, P. Grosse, B. Roldan Cuenya, Plasma-Activated Copper Nanocube Catalysts for Efficient Carbon Dioxide Electroreduction to Hydrocarbons and Alcohols, ACS Nano 11 (5) (2017) 4825–4831.

[64] D. Gao, F. Scholten, B. Roldan Cuenya, Improved CO_2 Electroreduction Performance on Plasma-Activated Cu Catalysts via Electrolyte Design: Halide Effect, ACS Catal. 7 (8) (2017) 5112–5120.

[65] S. Lee, D. Kim, J. Lee, Electrocatalytic Production of C_3-C_4 Compounds by Conversion of CO_2 on a Chloride-Induced Bi-Phasic Cu2O-Cu Catalyst, Angew. Chem. Int. Ed. 54 (49) (2015) 14701–14705.

[66] Y. Kwon, Y. Lum, E.L. Clark, J.W. Ager, A.T. Bell, CO2 Electroreduction with Enhanced Ethylene and Ethanol Selectivity by Nanostructuring Polycrystalline Copper, ChemElectroChem 3 (6) (2016) 1012–1019.

[67] L.R.L. Ting, R. García-Muelas, A.J. Martín, F.L.P. Veenstra, S.T.J. Chen, Y. Peng, E.Y.X. Per, S. Pablo-García, N. López, J. Pérez-Ramírez, B.S. Yeo, Electrochemical Reduction of Carbon Dioxide to 1-Butanol on Oxide-Derived Copper, Angew. Chem. Int. Ed. 59 (47) (2020) 21072–21079.

[68] Y. Chen, X.-Y. Li, Z. Chen, A. Ozden, J.E. Huang, P. Ou, J. Dong, J. Zhang, C. Tian, B.-H. Lee, X. Wang, S. Liu, Q. Qu, S. Wang, Y. Xu, R.K. Miao, Y. Zhao, Y. Liu, C. Qiu, J. Abed, H. Liu, H. Shin, D. Wang, Y. Li, D. Sinton, E.H. Sargent, Efficient multicarbon formation in acidic CO_2 reduction via tandem electrocatalysis, Nat. Nanotechnol. 19 (3) (2024) 311–318.

[69] B. Cao, F.-Z. Li, J. Gu, Designing Cu-Based Tandem Catalysts for CO_2 Electroreduction Based on Mass Transport of CO Intermediate, ACS Catal. 12 (15) (2022) 9735–9752.

[70] B. Zhang, L. Wang, D. Li, Z. Li, R. Bu, Y. Lu, Tandem strategy for electrochemical CO_2 reduction reaction, Chem. Catal. 2 (12) (2022) 3395–3429.

[71] T. Möller, M. Filippi, S. Brückner, W. Ju, P. Strasser, A CO_2 electrolyzer tandem cell system for CO_2-CO co-feed valorization in a Ni-N-C/Cu-catalyzed reaction cascade, Nat. Commun. 14 (1) (2023) 5680.

[72] Z.-Y. Zhang, H. Tian, H. Jiao, X. Wang, L. Bian, Y. Liu, N. Khaorapapong, Y. Yamauchi, Z.-L. Wang, SiO_2 assisted Cu^0–Cu^+–NH_2 composite interfaces for efficient CO_2 electroreduction to C_{2+} products, J. Mater. Chem. A 12 (2) (2024) 1218–1232.

[73] T. Cheng, H. Xiao, W.A. Goddard, Full atomistic reaction mechanism with kinetics for CO reduction on Cu(100) from ab initio molecular dynamics free-energy calculations at 298 K, Proc. Natl. Acad. Sci. 114 (8) (2017) 1795–1800.

[74] A. Xu, S.-F. Hung, A. Cao, Z. Wang, N. Karmodak, J.E. Huang, Y. Yan, A. Sedighian Rasouli, A. Ozden, F.-Y. Wu, Z.-Y. Lin, H.-J. Tsai, T.-J. Lee, F. Li, M. Luo, Y. Wang, X. Wang, J. Abed, Z. Wang, D.-H. Nam, Y.C. Li, A.H. Ip, D. Sinton, C. Dong, E.H. Sargent, Copper/alkaline earth metal oxide interfaces for electrochemical CO_2-to-alcohol conversion by selective hydrogenation, Nat. Catal. 5 (12) (2022) 1081–1088.

[75] B. Yang, L. Chen, S. Xue, H. Sun, K. Feng, Y. Chen, X. Zhang, L. Xiao, Y. Qin, J. Zhong, Z. Deng, Y. Jiao, Y. Peng, Electrocatalytic CO_2 reduction to alcohols by modulating the molecular geometry and Cu coordination in bicentric copper complexes, Nat. Commun. 13 (1) (2022) 5122.

[76] P. De Luna, R. Quintero-Bermudez, C.-T. Dinh, M.B. Ross, O.S. Bushuyev, P. Todorović, T. Regier, S.O. Kelley, P. Yang, E.H. Sargent, Catalyst electro-redeposition controls morphology and oxidation state for selective carbon dioxide reduction, Nat. Catal. 1 (2) (2018) 103–110.

[77] Y. Zhou, F. Che, M. Liu, C. Zou, Z. Liang, P. De Luna, H. Yuan, J. Li, Z. Wang, H. Xie, H. Li, P. Chen, E. Bladt, R. Quintero-Bermudez, T.-K. Sham, S. Bals, J. Hofkens, D. Sinton, G. Chen, E.H. Sargent, Dopant-induced electron localization drives CO_2 reduction to C_2 hydrocarbons, Nat. Chem. 10 (9) (2018) 974–980.

[78] D. Tan, B. Wulan, J. Ma, X. Cao, J. Zhang, Electrochemical-driven reconstruction for efficient reduction of carbon dioxide into alcohols, Chem. Catal. 3 (2) (2023).

[79] Zhang, R.; Zhang, J.; Wang, S.; Tan, Z.; Yang, Y.; Song, Y.; Li, M.; Zhao, Y.; Wang, H.; Han, B.; Duan, R., Synthesis of N-propanol from CO2 Electroreduction on Bicontinuous Cu2O/Cu Nanodomains. Angewandte Chemie International Edition n/a (n/a), e202405733.

[80] C. Peng, G. Luo, J. Zhang, M. Chen, Z. Wang, T.-K. Sham, L. Zhang, Y. Li, G. Zheng, Double sulfur vacancies by lithium tuning enhance CO_2 electroreduction to n-propanol, Nat. Commun. 12 (1) (2021) 1580.

[81] H. Tian, Z.-Y. Zhang, H. Fang, H. Jiao, T.-T. Gao, J.-T. Yang, L. Bian, Z.-L. Wang, Selective electrooxidation of methane to formic acid by atomically dispersed CuO_x and its induced Lewis acid sites on V_2O_5 in a tubular electrode, Appl. Catal. B: Environ. Energy 351 (2024) 124001.

[82] W. Lai, Y. Qiao, Y. Wang, H. Huang, Stability Issues in Electrochemical CO_2 Reduction: Recent Advances in Fundamental Understanding and Design Strategies, Adv. Mater. 35 (51) (2023) 2306288.

[83] S. Yu, S. Louisia, P. Yang, The Interactive Dynamics of Nanocatalyst Structure and Microenvironment during Electrochemical CO_2 Conversion, JACS Au 2 (3) (2022) 562–572.

[84] X. Wang, Z. Wang, F.P. García de Arquer, C.-T. Dinh, A. Ozden, Y.C. Li, D.-H. Nam, J. Li, Y.-S. Liu, J. Wicks, Z. Chen, M. Chi, B. Chen, Y. Wang, J. Tam, J. Y. Howe, A. Proppe, P. Todorović, F. Li, T.-T. Zhuang, C.M. Gabardo, A. R. Kirmani, C. McCallum, S.-F. Hung, Y. Lum, M. Luo, Y. Min, A. Xu, C.P. O'Brien, B. Stephen, B. Sun, A.H. Ip, L.J. Richter, S.O. Kelley, D. Sinton, E.H. Sargent, Efficient electrically powered CO_2-to-ethanol via suppression of deoxygenation, Nat. Energy 5 (6) (2020) 478–486.

[85] H. Li, T. Liu, P. Wei, L. Lin, D. Gao, G. Wang, X. Bao, High-Rate CO_2 Electroreduction to C_{2+} Products over a Copper-Copper Iodide Catalyst, Angew. Chem. 133 (26) (2021) 14450–14454.

[86] C. Peng, S. Yang, G. Luo, S. Yan, M. Shakouri, J. Zhang, Y. Chen, W. Li, Z. Wang, T.-K. Sham, G. Zheng, Surface Co-Modification of Halide Anions and Potassium Cations Promotes High-Rate CO_2-to-Ethanol Electrosynthesis, Adv. Mater. 34 (39) (2022) 2204476.

[87] P.K. Jiwanti, K. Natsui, K. Nakata, Y. Einaga, The electrochemical production of C_2/C_3 species from carbon dioxide on copper-modified boron-doped diamond electrodes, Electrochim. Acta 266 (2018) 414–419.

[88] H. Li, X. Qin, T. Jiang, X.-Y. Ma, K. Jiang, W.-B. Cai, Changing the Product Selectivity for Electrocatalysis of CO_2 Reduction Reaction on Plated Cu Electrodes, ChemCatChem 11 (24) (2019) 6139–6146.

[89] F. Yang, C. Liang, H. Yu, Z. Zeng, Y.M. Lam, S. Deng, J. Wang, Phosphorus-Doped Graphene Aerogel as Self-Supported Electrocatalyst for CO_2-to-Ethanol Conversion, Adv. Sci. 9 (25) (2022) 2202006.

[90] S. Mu, H. Lu, Q. Wu, L. Li, R. Zhao, C. Long, C. Cui, Hydroxyl radicals dominate reoxidation of oxide-derived Cu in electrochemical CO_2 reduction, Nat. Commun. 13 (1) (2022) 3694.

[91] Y. Yang, A. He, H. Li, Q. Zou, Z. Liu, C. Tao, J. Du, Operando Constructing Cu/Cu_2O Electrocatalysts for Efficient CO_2 Electroreduction to Ethanol: CO_2-Assisted Structural Evolution of Octahedral Cu_2O by Operando CV Activation, ACS Catal. 12 (20) (2022) 12942–12953.

[92] C. Chen, X. Yan, S. Liu, Y. Wu, Q. Wan, X. Sun, Q. Zhu, H. Liu, J. Ma, L. Zheng, H. Wu, B. Han, Highly Efficient Electroreduction of CO_2 to C_{2+} Alcohols on Heterogeneous Dual Active Sites, Angew. Chem. 132 (38) (2020) 16601–16606.

[93] R. Kas, R. Kortlever, H. Yılmaz, M.T.M. Koper, G. Mul, Manipulating the Hydrocarbon Selectivity of Copper Nanoparticles in CO_2 Electroreduction by Process Conditions, ChemElectroChem 2 (3) (2015) 354–358.

[94] A. Dutta, M. Rahaman, B. Hecker, J. Drnec, K. Kiran, I. Zelocualtecatl Montiel, D. Jochen Weber, A. Zanetti, A. Cedeño López, I. Martens, P. Broekmann, M. Oezaslan, CO_2 electrolysis – Complementary operando XRD, XAS and Raman spectroscopy study on the stability of CuxO foam catalysts, J. Catal. 389 (2020) 592–603.

[95] D.G. Park, J.W. Choi, H. Chun, H.S. Jang, H. Lee, W.H. Choi, B.C. Moon, K.-H. Kim, M.G. Kim, K.M. Choi, B. Han, J.K. Kang, Increasing CO Binding Energy and Defects by Preserving Cu Oxidation State via O_2-Plasma-Assisted N Doping on CuO Enables High C_{2+} Selectivity and Long-Term Stability in Electrochemical CO_2 Reduction, ACS Catal. 13 (13) (2023) 9222–9233.

[96] H. Jung, S.Y. Lee, C.W. Lee, M.K. Cho, D.H. Won, C. Kim, H.-S. Oh, B.K. Min, Y. J. Hwang, Electrochemical Fragmentation of Cu_2O Nanoparticles Enhancing Selective C–C Coupling from CO_2 Reduction Reaction, J. Am. Chem. Soc. 141 (11) (2019) 4624–4633.

[97] R. Du, T. Li, Q. Wu, P. Wang, X. Yang, Y. Fan, Y. Qiu, K. Yan, P. Wang, Y. Zhao, W.-W. Zhao, G. Chen, In Situ Engineering of the Cu^+/Cu^0 Interface to Boost C2+ Selectivity in CO_2 Electroreduction, ACS Appl. Mater. Interfaces 14 (32) (2022) 36527–36535.

[98] D. Bhalothia, W.-H. Hsiung, S.-S. Yang, C. Yan, P.-C. Chen, T.-H. Lin, S.-C. Wu, P.-C. Chen, K.-W. Wang, M.-W. Lin, T.-Y. Chen, Submillisecond Laser Annealing Induced Surface and Subsurface Restructuring of Cu–Ni–Pd Trimetallic Nanocatalyst Promotes Thermal CO_2 Reduction, ACS Appl. Energy Mater. 4 (12) (2021) 14043–14058.

[99] J. Hao, S. Xie, Q. Huang, Z. Ding, H. Sheng, C. Zhang, J. Yao, Spin-Enhanced C-C Coupling in CO_2 Electroreduction with Oxide-Derived Copper, CCS Chem. 5 (9) (2023) 2046–2058.

[100] Z. Wei, J. Ding, X. Duan, G.-L. Chen, F.-Y. Wu, L. Zhang, X. Yang, Q. Zhang, Q. He, Z. Chen, J. Huang, S.-F. Hung, X. Yang, Y. Zhai, Enhancing Selective Electrochemical CO_2 Reduction by In Situ Constructing Tensile-Strained Cu Catalysts, ACS Catal. 13 (7) (2023) 4711–4718.

[101] S. Kunze, L.C. Tănase, M.J. Prieto, P. Grosse, F. Scholten, L. De Souza Caldas, D. Van Vörden, T. Schmidt, B.R. Cuenya, Plasma-assisted oxidation of Cu(100) and Cu(111), Chem. Sci. 12 (42) (2021) 14241–14253.

[102] H. Mistry, A.S. Varela, C.S. Bonifacio, I. Zegkinoglou, I. Sinev, Y.-W. Choi, K. Kisslinger, E.A. Stach, J.C. Yang, P. Strasser, B.R. Cuenya, Highly selective plasma-activated copper catalysts for carbon dioxide reduction to ethylene, Nat. Commun. 7 (1) (2016) 12123.

[103] W. Zhang, Y. Yang, D. Guo, L. Liu, Recent progress on copper catalysts with different surface states for CO_2 electroreduction, J. Energy Chem. 88 (2024) 10–27.

[104] F. Scholten, I. Sinev, M. Bernal, B. Roldan Cuenya, Plasma-Modified Dendritic Cu Catalyst for CO_2 Electroreduction, ACS Catal. 9 (6) (2019) 5496–5502.

[105] K. Jiang, Y. Huang, G. Zeng, F.M. Toma, W.A. Goddard, I.I.I. Bell, A. T., Effects of Surface Roughness on the Electrochemical Reduction of CO_2 over Cu, ACS Energy Lett. 5 (4) (2020) 1206–1214.

[106] Z. Tang, E. Nishiwaki, K.E. Fritz, T. Hanrath, J. Suntivich, Cu(I) Reducibility Controls Ethylene vs Ethanol Selectivity on (100)-Textured Copper during Pulsed CO_2 Reduction, ACS Appl. Mater. Interfaces 13 (12) (2021) 14050–14055.

[107] R.M. Arán-Ais, F. Scholten, S. Kunze, R. Rizo, B. Roldan Cuenya, The role of in situ generated morphological motifs and Cu(i) species in C_{2+} product selectivity during CO_2 pulsed electroreduction, Nat. Energy 5 (4) (2020) 317–325.

[108] D. Raciti, M. Mao, J.H. Park, C. Wang, Local pH effect in the CO_2 reduction reaction on high-surface-area copper electrocatalysts, J. Electrochem. Soc. 165 (10) (2018) F799.

[109] F.S. Roberts, K.P. Kuhl, A. Nilsson, Electroreduction of Carbon Monoxide Over a Copper Nanocube Catalyst: Surface Structure and pH Dependence on Selectivity, ChemCatChem 8 (6) (2016) 1119–1124.

[110] H. Xiao, T. Cheng, W.A. Goddard, I.I.I. Sundararaman, R., Mechanistic Explanation of the pH Dependence and Onset Potentials for Hydrocarbon Products from Electrochemical Reduction of CO on Cu (111), J. Am. Chem. Soc. 138 (2) (2016) 483–486.

[111] M. Moura de Salles Pupo, R. Kortlever, Electrolyte Effects on the Electrochemical Reduction of CO_2, ChemPhysChem 20 (22) (2019) 2926–2935.

[112] T. Kim, G.T.R. Palmore, A scalable method for preparing Cu electrocatalysts that convert CO_2 into C_{2+} products, Nat. Commun. 11 (1) (2020) 3622.

[113] C. He, C. Xu, W. Zhang, Instructive Synergistic Effect of Coordinating Phosphorus in Transition-Metal-Doped β-Phosphorus Carbide Guiding the Design of High-Performance CO_2RR Electrocatalysts, ACS Appl. Mater. Interfaces 15 (49) (2023) 57015–57028.

[114] D. Tan, B. Wulan, J. Ma, X. Cao, J. Zhang, Electrochemical-driven reconstruction for efficient reduction of carbon dioxide into alcohols, Chem. Catal. 3 (2) (2023) 100512.

[115] Y. Li, D. Kim, S. Louisia, C. Xie, Q. Kong, S. Yu, T. Lin, S. Aloni, S.C. Fakra, P. Yang, Electrochemically scrambled nanocrystals are catalytically active for CO_2-to-multicarbons, Proc. Natl. Acad. Sci. 117 (17) (2020) 9194–9201.

[116] J.-Y. Kim, D. Hong, J.-C. Lee, H.G. Kim, S. Lee, S. Shin, B. Kim, H. Lee, M. Kim, J. Oh, G.-D. Lee, D.-H. Nam, Y.-C. Joo, Quasi-graphitic carbon shell-induced Cu confinement promotes electrocatalytic CO_2 reduction toward C_{2+} products, Nat. Commun. 12 (1) (2021) 3765.

[117] T.-C. Chou, C.-C. Chang, H.-L. Yu, W.-Y. Yu, C.-L. Dong, J.-J. Velasco-Vélez, C.-H. Chuang, L.-C. Chen, J.-F. Lee, J.-M. Chen, H.-L. Wu, Controlling the Oxidation State of the Cu Electrode and Reaction Intermediates for Electrochemical CO_2 Reduction to Ethylene, J. Am. Chem. Soc. 142 (6) (2020) 2857–2867.

[118] Y. Yang, S. Louisia, S. Yu, J. Jin, I. Roh, C. Chen, M.V. Fonseca Guzman, J. Feijóo, P.-C. Chen, H. Wang, C.J. Pollock, X. Huang, Y.-T. Shao, C. Wang, D.A. Muller, H. D. Abruña, P. Yang, Operando studies reveal active Cu nanograins for CO_2 electroreduction, Nature 614 (7947) (2023) 262–269.

[119] D. Ren, N.T. Wong, A.D. Handoko, Y. Huang, B.S. Yeo, Mechanistic Insights into the Enhanced Activity and Stability of Agglomerated Cu Nanocrystals for the Electrochemical Reduction of Carbon Dioxide to n-Propanol, J. Phys. Chem. Lett. 7 (1) (2016) 20–24.

[120] Z.-Z. Wu, X.-L. Zhang, Z.-Z. Niu, F.-Y. Gao, P.-P. Yang, L.-P. Chi, L. Shi, W.-S. Wei, R. Liu, Z. Chen, S. Hu, X. Zheng, M.-R. Gao, Identification of Cu(100)/Cu(111) Interfaces as Superior Active Sites for CO Dimerization During CO_2 Electroreduction, J. Am. Chem. Soc. 144 (1) (2022) 259–269.

[121] D. Kim, C.S. Kley, Y. Li, P. Yang, Copper nanoparticle ensembles for selective electroreduction of CO_2 to C_2-C_3 products, Proc. Natl. Acad. Sci. 114 (40) (2017) 10560–10565.

[122] C. Hahn, T. Hatsukade, Y.-G. Kim, A. Vailionis, J.H. Baricuatro, D.C. Higgins, S. A. Nitopi, M.P. Soriaga, T.F. Jaramillo, Engineering Cu surfaces for the electrocatalytic conversion of CO_2: Controlling selectivity toward oxygenates and hydrocarbons, Proc. Natl. Acad. Sci. 114 (23) (2017) 5918–5923.

[123] Q. Fan, X. Zhang, X. Ge, L. Bai, D. He, Y. Qu, C. Kong, J. Bi, D. Ding, Y. Cao, X. Duan, J. Wang, J. Yang, Y. Wu, Manipulating Cu Nanoparticle Surface Oxidation States Tunes Catalytic Selectivity toward CH_4 or C_{2+} Products in CO_2 Electroreduction, Adv. Energy Mater. 11 (36) (2021) 2101424.

[124] N.S. Romero Cuellar, K. Wiesner-Fleischer, M. Fleischer, A. Rucki, O. Hinrichsen, Advantages of CO over CO_2 as reactant for electrochemical reduction to ethylene, ethanol and n-propanol on gas diffusion electrodes at high current densities, Electrochim. Acta 307 (2019) 164–175.

[125] G. Wu, Y. Song, Q. Zheng, C. Long, T. Fan, Z. Yang, X. Huang, Q. Li, Y. Sun, L. Zuo, S. Lei, Z. Tang, Selective Electroreduction of CO_2 to n-Propanol in Two-Step Tandem Catalytic System, Adv. Energy Mater. 12 (36) (2022) 2202054.

[126] C.-C. Chang, M.-S. Ku, Role of High-Index Facet Cu(711) Surface in Controlling the C2 Selectivity for CO_2 Reduction Reaction—A DFT Study, J. Phys. Chem. C. 125 (20) (2021) 10919–10925.

[127] Y. Fang, X. Liu, Z. Liu, L. Han, J. Ai, G. Zhao, O. Terasaki, C. Cui, J. Yang, C. Liu, Synthesis of amino acids by electrocatalytic reduction of CO_2 on chiral Cu surfaces, Chem 9 (2) (2023) 460–471.

[128] J.G. Chen, Electrochemical CO_2 Reduction via Low-Valent Nickel Single-Atom Catalyst, Joule 2 (4) (2018) 587–589.

[129] A. Wang, J. Li, T. Zhang, Heterogeneous single-atom catalysis, Nat. Rev. Chem. 2 (6) (2018) 65–81.

[130] G. Shi, Y. Xie, L. Du, X. Fu, X. Chen, W. Xie, T.-B. Lu, M. Yuan, M. Wang, Constructing Cu−C Bonds in a Graphdiyne-Regulated Cu Single-Atom Electrocatalyst for CO_2 Reduction to CH_4, Angew. Chem. Int. Ed. 61 (23) (2022) e202203569.

[131] H. Zhu, S. Liu, J. Yu, Q. Chen, X. Mao, T. Wu, Computational screening of effective g-C_3N_4 based single atom electrocatalysts for the selective conversion of CO_2, Nanoscale 15 (18) (2023) 8416–8423.

[132] C.E. Creissen, M. Fontecave, Keeping sight of copper in single-atom catalysts for electrochemical carbon dioxide reduction, Nat. Commun. 13 (1) (2022) 2280.

[133] Z. Ma, T. Wan, D. Zhang, J.A. Yuwono, C. Tsounis, J. Jiang, Y.-H. Chou, X. Lu, P. V. Kumar, Y.H. Ng, D. Chu, C.Y. Toe, Z. Han, R. Amal, Atomically Dispersed Cu Catalysts on Sulfide-Derived Defective Ag Nanowires for Electrochemical CO_2 Reduction, ACS Nano 17 (3) (2023) 2387–2398.

[134] S. Li, A. Guan, C. Yang, C. Peng, X. Lv, Y. Ji, Y. Quan, Q. Wang, L. Zhang, G. Zheng, Dual-Atomic Cu Sites for Electrocatalytic CO Reduction to C_{2+} Products, ACS Mater. Lett. 3 (12) (2021) 1729–1737.

[135] Q. Sun, C. Jia, Y. Zhao, C. Zhao, Single atom-based catalysts for electrochemical CO_2 reduction, Chin. J. Catal. 43 (7) (2022) 1547–1597.

[136] D.E. Polyansky, D.C. Grills, M.Z. Ertem, K.T. Ngo, E. Fujita, Role of Bimetallic Interactions in the Enhancement of Catalytic CO_2 Reduction by a Macrocyclic Cobalt Catalyst, ACS Catal. 12 (3) (2022) 1706–1717.

[137] K.E. Rivera Cruz, Y. Liu, T.L. Soucy, P.M. Zimmerman, C.C.L. McCrory, Increasing the CO_2 Reduction Activity of Cobalt Phthalocyanine by Modulating the σ-Donor Strength of Axially Coordinating Ligands, ACS Catal. 11 (21) (2021) 13203–13216.

[138] R. Wang, J. Liu, Q. Huang, L.-Z. Dong, S.-L. Li, Y.-Q. Lan, Partial Coordination-Perturbed Bi-Copper Sites for Selective Electroreduction of CO_2 to Hydrocarbons, Angew. Chem. Int. Ed. 60 (36) (2021) 19829–19835.

[139] H.-L. Zhu, H.-Y. Chen, Y.-X. Han, Z.-H. Zhao, P.-Q. Liao, X.-M. Chen, A Porous π–π Stacking Framework with Dicopper(I) Sites and Adjacent Proton Relays for Electroreduction of CO_2 to C_{2+} Products, J. Am. Chem. Soc. 144 (29) (2022) 13319–13326.

[140] N. Sakamoto, K. Sekizawa, S. Shirai, T. Nonaka, T. Arai, S. Sato, T. Morikawa, Dinuclear Cu(I) molecular electrocatalyst for CO_2-to-C_3 product conversion, Nat. Catal. (2024).

[141] G. Wang, J. Chen, Y. Ding, P. Cai, L. Yi, Y. Li, C. Tu, Y. Hou, Z. Wen, L. Dai, Electrocatalysis for CO_2 conversion: from fundamentals to value-added products, Chem. Soc. Rev. 50 (8) (2021) 4993–5061.

[142] J.D. Lee, J.B. Miller, A.V. Shneidman, L. Sun, J.F. Weaver, J. Aizenberg, J. Biener, J.A. Boscoboinik, A.C. Foucher, A.I. Frenkel, J.E.S. van der Hoeven, B. Kozinsky, N. Marcella, M.M. Montemore, H.T. Ngan, C.R. O'Connor, C.J. Owen, D. J. Stacchiola, E.A. Stach, R.J. Madix, P. Sautet, C.M. Friend, Dilute Alloys Based on Au, Ag, or Cu for Efficient Catalysis: From Synthesis to Active Sites, Chem. Rev. 122 (9) (2022) 8758–8808.

[143] M.T. Tang, H.-J. Peng, J.H. Stenlid, F. Abild-Pedersen, Exploring Trends on Coupling Mechanisms toward C_3 Product Formation in $CO_{(2)}R$, J. Phys. Chem. C. 125 (48) (2021) 26437–26447.

[144] A. Herzog, A. Bergmann, H.S. Jeon, J. Timoshenko, S. Kühl, C. Rettenmaier, M. Lopez Luna, F.T. Haase, B. Roldan Cuenya, Operando Investigation of Ag-Decorated Cu_2O Nanocube Catalysts with Enhanced CO_2 Electroreduction toward Liquid Products, Angew. Chem. Int. Ed. 60 (13) (2021) 7426–7435.

[145] Y.E. Kim, J.E. Park, J.H. Lee, H. Choi, W. Lee, Y.N. Ko, H.Y. Kim, K.T. Park, Ag decorated-Cu_2O catalysts with enhanced selectivity for CO_2 electroreduction toward C_{2+} products, J. Environ. Chem. Eng. 11 (5) (2023) 111028.

[146] S. Bae, S.Y. Hwang, G. Yun, Y. Gwon, S.Y. Kim, C.K. Rhee, Y. Sohn, Ag–Sb/Cu by Galvanic Replacement: Electrochemical CO_2 Reduction and Unveiling C_{3+} Hydrocarbon Pathways, J. Phys. Chem. C. 127 (49) (2023) 23601–23617.

[147] F. Pan, H. Zhang, K. Liu, D. Cullen, K. More, M. Wang, Z. Feng, G. Wang, G. Wu, Y. Li, Unveiling Active Sites of CO_2 Reduction on Nitrogen-Coordinated and Atomically Dispersed Iron and Cobalt Catalysts, ACS Catal. 8 (4) (2018) 3116–3122.

[148] S. Jeong, C. Huang, Z. Levell, R.X. Skalla, W. Hong, N.J. Escorcia, Y. Losovyj, B. Zhu, A.N. Butrum-Griffith, Y. Liu, C.W. Li, D. Reifsnyder Hickey, Y. Liu, X. Ye, Facet-Defined Dilute Metal Alloy Nanorods for Efficient Electroreduction of CO_2 to n-Propanol, J. Am. Chem. Soc. 146 (7) (2024) 4508–4520.

[149] H. Xie, S. Chen, F. Ma, J. Liang, Z. Miao, T. Wang, H.-L. Wang, Y. Huang, Q. Li, Boosting Tunable Syngas Formation via Electrochemical CO_2 Reduction on Cu/In_2O_3 Core/Shell Nanoparticles, ACS Appl. Mater. Interfaces 10 (43) (2018) 36996–37004.

[150] K.P. Kuhl, T. Hatsukade, E.R. Cave, D.N. Abram, J. Kibsgaard, T.F. Jaramillo, Electrocatalytic Conversion of Carbon Dioxide to Methane and Methanol on Transition Metal Surfaces, J. Am. Chem. Soc. 136 (40) (2014) 14107–14113.

[151] R.A. Geioushy, M.M. Khaled, K. Alhooshani, A.S. Hakeem, A. Rinaldi, Graphene/ZnO/Cu2O electrocatalyst for selective conversion of CO_2 into n-propanol, Electrochim. Acta 245 (2017) 456–462.

[152] Z. Geng, X. Kong, W. Chen, H. Su, Y. Liu, F. Cai, G. Wang, J. Zeng, Oxygen Vacancies in ZnO Nanosheets Enhance CO_2 Electrochemical Reduction to CO, Angew. Chem. Int. Ed. 57 (21) (2018) 6054–6059.

[153] C. Azenha, C. Mateos-Pedrero, M. Alvarez-Guerra, A. Irabien, A. Mendes, Binary copper-bismuth catalysts for the electrochemical reduction of CO_2: Study on surface properties and catalytic activity, Chem. Eng. J. 445 (2022) 136575.

[154] N.S. Romero Cuellar, C. Scherer, B. Kaçkar, W. Eisenreich, C. Huber, K. Wiesner-Fleischer, M. Fleischer, O. Hinrichsen, Two-step electrochemical reduction of CO_2 towards multi-carbon products at high current densities, J. CO_2 Util. 36 (2020) 263–275.

[155] T. Burdyny, W.A. Smith, CO_2 reduction on gas-diffusion electrodes and why catalytic performance must be assessed at commercially-relevant conditions, Energy Environ. Sci. 12 (5) (2019) 1442–1453.

[156] B. Zhang, J. Zhang, M. Hua, Q. Wan, Z. Su, X. Tan, L. Liu, F. Zhang, G. Chen, D. Tan, X. Cheng, B. Han, L. Zheng, G. Mo, Highly Electrocatalytic Ethylene Production from CO_2 on Nanodefective Cu Nanosheets, J. Am. Chem. Soc. 142 (31) (2020) 13606–13613.

[157] X. She, L. Zhai, Y. Wang, P. Xiong, M.M.-J. Li, T.-S. Wu, M.C. Wong, X. Guo, Z. Xu, H. Li, H. Xu, Y. Zhu, S.C.E. Tsang, S.P. Lau, Pure-water-fed, electrocatalytic CO_2 reduction to ethylene beyond 1,000 h stability at 10 A, Nat. Energy 9 (1) (2024) 81–91.

[158] A.N. Biswas, L.R. Winter, Z. Xie, J.G. Chen, Utilizing CO2 as a Reactant for C_3 Oxygenate Production via Tandem Reactions, JACS Au 3 (2) (2023) 293–305.

[159] M.G. Lee, X.-Y. Li, A. Ozden, J. Wicks, P. Ou, Y. Li, R. Dorakhan, J. Lee, H.K. Park, J.W. Yang, B. Chen, J. Abed, R. dos Reis, G. Lee, J.E. Huang, T. Peng, Y.-H. Chin, D. Sinton, E.H. Sargent, Selective synthesis of butane from carbon monoxide using cascade electrolysis and thermocatalysis at ambient conditions, Nat. Catal. 6 (4) (2023) 310–318.

[160] M.G. Lee, S. Kandambeth, X.-Y. Li, O. Shekhah, A. Ozden, J. Wicks, P. Ou, S. Wang, R. Dorakhan, S. Park, P.M. Bhatt, V.S. Kale, D. Sinton, M. Eddaoudi, E. H. Sargent, Bimetallic Metal Sites in Metal–Organic Frameworks Facilitate the Production of 1-Butene from Electrosynthesized Ethylene, J. Am. Chem. Soc. 146 (20) (2024) 14267–14277.

[161] J. Zhang, X. Kang, Y. Yan, X. Ding, L. He, Y. Li, Cascade Electrocatalytic and Thermocatalytic Reduction of CO_2 to Propionaldehyde, Angew. Chem. Int. Ed. 63 (12) (2024) e202315777.

[162] A.R. Paris, A.B. Bocarsly, Ni–Al Films on Glassy Carbon Electrodes Generate an Array of Oxygenated Organics from CO_2, ACS Catal. 7 (10) (2017) 6815–6820.

[163] S. Banerjee, A. Kakekhani, R.B. Wexler, A.M. Rappe, Mechanistic Insights into CO_2 Electroreduction on Ni_2P: Understanding Its Selectivity toward Multicarbon Products, ACS Catal. 11 (18) (2021) 11706–11715.

[164] K.U.D. Calvinho, A.B. Laursen, K.M.K. Yap, T.A. Goetjen, S. Hwang, N. Murali, B. Mejia-Sosa, A. Lubarski, K.M. Teeluck, E.S. Hall, E. Garfunkel, M. Greenblatt, G.C. Dismukes, Selective CO_2 reduction to C_3 and C_4 oxyhydrocarbons on nickel phosphides at overpotentials as low as 10 mV, Energy Environ. Sci. 11 (9) (2018) 2550–2559.

[165] J. Cheng, B. Yuan, H. Tao, Y. Chen, Y. Ming, M. Han, Z. Eisenberg, R., Molecular Nickel Thiolate Complexes for Electrochemical Reduction of CO_2 to C_{1-3} Hydrocarbons, Angew. Chem. Int. Ed. 62 (9) (2023) e202211804.

[166] A. Kondori, M. Esmaeilirad, A. Baskin, B. Song, J. Wei, W. Chen, C.U. Segre, R. Shahbazian-Yassar, D. Prendergast, M. Asadi, Identifying Catalytic Active Sites of Trimolybdenum Phosphide (Mo_3P) for Electrochemical Hydrogen Evolution, Adv. Energy Mater. 9 (22) (2019) 1900516.

[167] M. Esmaeilirad, A. Kondori, N. Shan, M.T. Saray, S. Sarkar, A.M. Harzandi, C. M. Megaridis, R. Shahbazian-Yassar, L.A. Curtiss, C.U. Segre, M. Asadi, Efficient electrocatalytic conversion of CO_2 to ethanol enabled by imidazolium-functionalized ionomer confined molybdenum phosphide, Appl. Catal. B: Environ. 317 (2022) 121681.

[168] S. Kang, S. Han, Y. Kang, Unveiling Electrochemical Reaction Pathways of CO_2 Reduction to C Species at S-Vacancies of MoS_2, ChemSusChem 12 (12) (2019) 2671–2678.

[169] S.A. Francis, J.M. Velazquez, I.M. Ferrer, D.A. Torelli, D. Guevarra, M. T. McDowell, K. Sun, X. Zhou, F.H. Saadi, J. John, M.H. Richter, F.P. Hyler, K. M. Papadantonakis, B.S. Brunschwig, N.S. Lewis, Reduction of Aqueous CO_2 to 1-Propanol at MoS_2 Electrodes, Chem. Mater. 30 (15) (2018) 4902–4908.

[170] O. Ahmed Taialla, U. Mustapha, A. Hakam Shafiu Abdullahi, E. Kotob, M. Mosaad Awad, A. Musa Alhassan, I. Hussain, K. Omer, S.A. Ganiyu, K. Alhooshani, Unlocking the potential of ZIF-based electrocatalysts for electrochemical reduction of CO_2: Recent advances, current trends, and machine learnings, Coord. Chem. Rev. 504 (2024) 215669.

[171] A. Tkatchenko, Machine learning for chemical discovery, Nat. Commun. 11 (1) (2020) 4125.

[172] E. Hu, C. Liu, W. Zhang, Q. Yan, Machine Learning Assisted Understanding and Discovery of CO_2 Reduction Reaction Electrocatalyst, J. Phys. Chem. C. 127 (2) (2023) 882–893.

[173] K. Tran, Z.W. Ulissi, Active learning across intermetallics to guide discovery of electrocatalysts for CO_2 reduction and H_2 evolution, Nat. Catal. 1 (9) (2018) 696–703.

[174] J.K. Pedersen, T.A.A. Batchelor, A. Bagger, J. Rossmeisl, High-Entropy Alloys as Catalysts for the CO_2 and CO Reduction Reactions, ACS Catal. 10 (3) (2020) 2169–2176.

[175] C. Liang, B. Wang, S. Hao, G. Chen, P.-A. Heng, X. Zou, Multi-Task Mixture Density Graph Neural Networks for Predicting Catalyst Performance, Adv. Funct. Mater. 34 (45) (2024) 2404392.

[176] M. Zhong, K. Tran, Y. Min, C. Wang, Z. Wang, C.-T. Dinh, P. De Luna, Z. Yu, A. S. Rasouli, P. Brodersen, S. Sun, O. Voznyy, C.-S. Tan, M. Askerka, F. Che, M. Liu, A. Seifitokaldani, Y. Pang, S.-C. Lo, A. Ip, Z. Ulissi, E.H. Sargent, Accelerated discovery of CO_2 electrocatalysts using active machine learning, Nature 581 (7807) (2020) 178–183.

[177] H. Li, Y. Jiang, X. Li, K. Davey, Y. Zheng, Y. Jiao, S.-Z. Qiao, C_{2+} Selectivity for CO_2 Electroreduction on Oxidized Cu-Based Catalysts, J. Am. Chem. Soc. 145 (26) (2023) 14335–14344.
[178] D. Behrendt, S. Banerjee, C. Clark, A.M. Rappe, High-Throughput Computational Screening of Bioinspired Dual-Atom Alloys for CO_2 Activation, J. Am. Chem. Soc. 145 (8) (2023) 4730–4735.
[179] A.P. Dmitrieva, A.S. Fomkina, C.T. Tracey, E.A. Romanenko, A. Ayati, P. V. Krivoshapkin, E.F. Krivoshapkina, AI and ML for selecting viable electrocatalysts: progress and perspectives, J. Mater. Chem. A 12 (45) (2024) 31074–31102.
[180] A. Badreldin, O. Bouhali, A. Abdel-Wahab, Complimentary Computational Cues for Water Electrocatalysis: A DFT and ML Perspective, Adv. Funct. Mater. 34 (12) (2024) 2312425.
[181] B. Hasa, Y. Zhao, F. Jiao, In Situ/Operando Characterization Techniques of Electrochemical CO_2 Reduction, Annu. Rev. Chem. Biomol. Eng. 14 (2023) 165–185.
[182] H. Li, Y. Jiao, K. Davey, S.-Z. Qiao, Data-Driven Machine Learning for Understanding Surface Structures of Heterogeneous Catalysts, Angew. Chem. Int. Ed. 62 (9) (2023) e202216383.
[183] Z. Yao, Y. Lum, A. Johnston, L.M. Mejia-Mendoza, X. Zhou, Y. Wen, A. Aspuru-Guzik, E.H. Sargent, Z.W. Seh, Machine learning for a sustainable energy future, Nat. Rev. Mater. 8 (3) (2023) 202–215.
[184] H. Lu, N. Uddin, Z. Sun, Z. Chen, Z. Mahfoud, Y. Wu, A.A. Wibowo, Z. Su, X. Yin, C.S. Tang, X. Liao, S.P. Ringer, X.S. Zhao, H.T. Nguyen, A.T.S. Wee, M. Bosman, Z. Yin, Stabilized bismuth nanoplasmonics for selective CO_2 reduction to methanol at a heterointerface, Nano Energy 115 (2023) 108684.
[185] N. Uddin, Z. Sun, J. Langley, H. Lu, P. Cao, A. Wibowo, X. Yin, C.S. Tang, H. T. Nguyen, J.D. Evans, X. Li, X. Zhang, M. Heggen, R.E. Dunin-Borkowski, A.T. S. Wee, H. Zhao, N. Cox, Z. Yin, Ultrabroadband plasmon driving selective photoreforming of methanol under ambient conditions, Proc. Natl. Acad. Sci. 120 (3) (2023) e2212075120.
[186] W. Lai, Y. Qiao, J. Zhang, Z. Lin, H. Huang, Design strategies for markedly enhancing energy efficiency in the electrocatalytic CO_2 reduction reaction, Energy Environ. Sci. 15 (9) (2022) 3603–3629.
[187] F. Pan, Y. Yang, Designing CO_2 reduction electrode materials by morphology and interface engineering, Energy Environ. Sci. 13 (8) (2020) 2275–2309.
[188] R. Ding, J. Chen, Y. Chen, J. Liu, Y. Bando, X. Wang, Unlocking the potential: machine learning applications in electrocatalyst design for electrochemical hydrogen energy transformation, Chem. Soc. Rev. 53 (23) (2024) 11390–11461.
[189] H. Zhao, W. Chen, H. Huang, Z. Sun, Z. Chen, L. Wu, B. Zhang, F. Lai, Z. Wang, M. L. Adam, C.H. Pang, P.K. Chu, Y. Lu, T. Wu, J. Jiang, Z. Yin, X.-F. Yu, A robotic platform for the synthesis of colloidal nanocrystals, Nat. Synth. 2 (6) (2023) 505–514.
[190] H. Lu, J. Tournet, K. Dastafkan, Y. Liu, Y.H. Ng, S.K. Karuturi, C. Zhao, Z. Yin, Noble-Metal-Free Multicomponent Nanointegration for Sustainable Energy Conversion, Chem. Rev. 121 (17) (2021) 10271–10366.
[191] X. Song, P. Pu, H. Feng, H. Ding, Y. Deng, Z. Ge, S. Zhao, T. Liu, Y. Yang, M. Wei, X. Zhang, Integrating Active Learning and DFT for Fast-Tracking Single-Atom Alloy Catalysts in CO_2-to-Fuel Conversion, ACS Appl. Mater. Interfaces 16 (41) (2024) 55416–55428.

Yiding Yang is currently a PhD student at the Research School of Chemistry, Australian National University (Australia). He got his MSc from the Australian National University (Australia) in 2023 and his BSc from Soochow University (China) in 2020. He is now focusing on the development of novel nanomaterials for CO_2 capture and conversion.

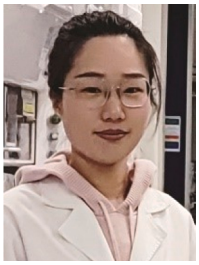

Kaili Liu is currently a PhD student at the Research School of Chemistry, Australian National University (Australia). She got her MSc from National Center for Nanoscience and Technology, University of Chinese Academy of Sciences (China) in 2017 and BSc from Qingdao University of Science and Technology (China) in 2014. She is now focusing on the development of novel nanomaterials for energy conversion.

Md Sakib Hasan Khan is currently a PhD student at the Research School of Chemistry, Australian National University (Australia). He got his MSc from the Dept. of Electrical and Electronic Engineering (EEE), Khulna University of Engineering & Technology (KUET) in 2020 and his BSc from the same institution in 2018. He is now focusing on the development of novel nanomaterials for energy conversion.

Zhehao Sun received his B. Eng. and M. Eng. degree in Energy and Environmental Engineering from the Dalian University of Technology. He is currently a PhD candidate in the Research School of Chemistry, Australian National University. His research interests include functional nanomaterials, first-principles calculations, machine learning, and solid-state physics for energy conversion.

Professor Zongyou Yin obtained his B.S. and M.S. degrees at Jilin University in China and completed his Ph.D. at Nanyang Technological University (NTU) in Singapore. Then, he started his postdoc careers at NTU/Singapore, IMRE/Singapore, followed by MIT, and then Harvard University. Dr. Yin started his own Research Group at Australian National University (ANU) in 2017. His group's research is interdisciplinary, encompassing chemistry and physics of nano-to-atomic materials, the fundamental relationship among materials structures-devices, and synergistic integration of multi-functions towards systems for energy and wearable applications.